Design of aiming control strategies to enhance energy harnessing in power-generation solar systems with central receiver during cloud shading transients

Jesús Manuel García García

Major Professor: **Marco E. Sanjuan M., Ph.D.**
Co-Major Professor: **Ricardo S. Vasquez P., Ph.D.**

CSIRO Supervisor: **Yen Chean Soo Too, Ph.D.**
CSIRO Supervisor: **Andrew Beath, Ph.D.**

Department of Mechanical Engineering
Universidad del Norte

A thesis submitted for the degree of
Doctor of Philosophy

Barranquilla, Colombia 2017

Dedico esta tesis con mucho cariño a todos los que siempre creyeron en mí. A Dios quien siempre ha estado a mi lado, y a toda mi familia: mi mamá (Olga), mi papá (Manuel), mi hermano (Oneiber), mis hermanas (Marianela y Marielis), y mis dos sobrinitas (Marian y Bárbara). Los quiero mucho.

Acknowledgements

Haber realizado este doctorado ha sido toda una aventura, todavía recuerdo claramente los primeros días de esta odisea. Todas las personas que me han conocido durante este periodo se darán cuenta que no ha sido para nada fácil. Ha habido picos de euforia máximos con logros muy importantes, así como abismos enormes de los cuales me costó salir. Pero al final se ha conseguido, el ciclo se cierra con la presentación de este proyecto. A través de estas palabras quiero rendir tributo a todas esas personas, muchas veces anónimas, que con su granito de arena me ayudaron en esta travesía. Como mencioné en la dedicatoria, primero debo agradecer enormemente a Dios y a mi familia, ustedes siempre me animan a seguir adelante. Nada de esto fuese posible sin su ayuda.

Agradezco también todo el apoyo recibido de mi tutor, el Doctor Marco Sanjuan, quien con todos sus consejos y ayuda me ha guiado en este camino tan difícil. Aunado al esfuerzo de mi tutor se encuentra el apoyo de la Universidad del Norte, una institución que me recibió con los brazos abiertos. Muchas gracias también a todo el Departamento de Ingeniería Mecánica, y a todos los Profesores que compartieron sus conocimientos conmigo. A ustedes, mis más sinceras palabras de agradecimiento por todo ese esfuerzo y dedicación.

Dentro de este proyecto también aprecio muchísimo los consejos del Doctor Ricardo Vásquez. Una persona con un corazón enorme que me apoyó con conocimientos y ayuda para desarrollar la pasantía internacional en Australia. En este sentido, agradezco también la colaboración del instituto australiano de investigación CSIRO, guiado por el Doctor Yen Chean Soo Too, y el Doctor Andrew Beath.

Quiero recordar también al Doctor Edinzo Iglesias, el Doctor Yohn Garcia, y la Doctora Silvia Calderón. Este logro no hubiese sido posible sin su apoyo cuando me encontraba en formación durante mis estudios de pregrado en Ingeniería Química de la Universidad de Los Andes en Venezuela. Muchas gracias por haber confiado en mí.

Finalmente quiero agradecer a todos los compañeros del programa de maestría y doctorado con quienes he recorrido este camino. Agradezco infinitamente a Adriana quien ha sido un pilar enorme en aquellos momentos donde el ánimo flaqueaba, solo puedo decir muchísimas gracias y que Dios te acompañe en todos los proyectos que emprendas. Asimismo, agradezco el apoyo de compañeros como Iván (Portnoy y Gómez), David, Jorge, Yuhan, Johnnys, Elena, Cinthia, Horacio, Andrés, Diego, Arnaldo, José, Blanca, German, Arnold, Hermes, Fernando, Eduar, Lisneider, Daniel, Luz, Leonardo. Creo que se me escapan varios nombres, no obstante, a todos con quienes he compartido muchas gracias por todos los excelentes momentos vividos.

A todos, mil gracias.
Lo logramos.

Abstract

Maintaining receiver's thermal stresses below the material limits is one of the issues that need careful attention in solar thermal towers. Thermal stresses depend on heliostats' aiming points over the central receiver and available direct solar radiation at any instant. The solar radiation profiles change due to several reasons such as earth's movements. Even though this change is unavoidable, its behavior is predictable. However, at ground level, direct solar radiation mainly varies because of clouds, which is a complex phenomenon not easily predictable. Since solar central receivers rely on an unavoidable time-changing resource, then the heliostats' aiming points need to be appropriately changed to avoid excessive thermal stresses caused by sudden solar radiation changes. This dissertation proposes a novel aiming point strategy based on a multiple input multiple output model predictive control (MPC) approach.

The novel alternative methodology proposes an agent-based group behavior over heliostats' subsets, which makes possible either concentrating or dispersing solar radiation as required by the MPC strategy. After developing the appropriate model of the process, the analysis is focused on the closed-loop performance of the process. The results of these tests indicate that it is possible to develop a closed-loop control algorithm that distributes solar radiation over the central receiver on the predefined heat flux limits.

Next step requires the analysis under cloud shading radiation transients. A dynamic $2D$ cloud shading disturbance is developed using a biomimetic cloud-shading model. The model is tuned through an optimization procedure employing available measurement time series. The method uses an objective function based on statistical indexes that allow extracting the most important characteristics of an actual set of curves. Then, a multi-objective optimization algorithm finds the tuning parameters of the

model that better fit data. The results show that it is possible to obtain responses like real direct solar radiation transients.

The closed-loop simulations, using the developed disturbance, reveal that the primary feedback loop aiming strategy could successfully restore the solar receiver back to its steady state after transient operations caused by clouds. However, the controlled variables showed undesired overshoots and high heating rates. These issues are overcome through a set point readjustment approach, which is temporally supported by a PI controller. Following tests indicate that the proposed aiming control strategy provides a continuous safe operation of the solar central receiver when subject to transient flux distribution due to clouds.

Contents

List of Figures

Chapter 1

Introduction

Nowadays energy consumption is characterized by its unsustainability due to the use of non-renewable natural resources. Currently, there are several options addressed to take advantage of renewable resources. One of these promising alternatives involves taking advantage of solar radiation, a worldwide available resource [1, 2]. Three big groups conform solar technologies, through photovoltaic panels where solar radiation goes directly to electricity, through thermal processes which consist of heating a fluid that later has several applications downstream, and through chemical reactions that can be used to produce heat or electricity. Figure (1.1) shows a summary of these technologies [3].

Solar thermal processes employ different kinds of collectors, which can be classified as shown in Fig. (1.2) [2]. According to the concentration ratio, solar collectors fall into two main groups. The first group contains the solar collector where radiation goes over a focal line and the other ones where the energy goes to a focal point. In the line focusing alternatives, parabolic trough solar concentrators are at the top as one of the most accepted technologies. In regards to point focusing alternatives, the most

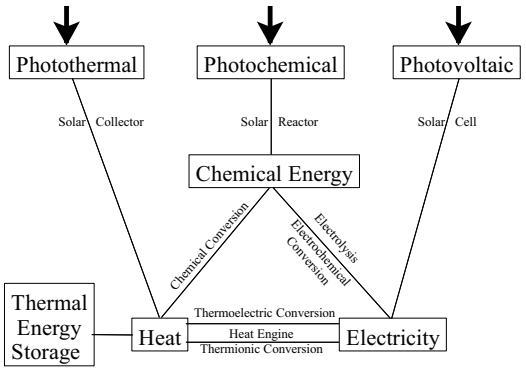

Figure 1.1: Available technologies developed to take advantage of solar radiation [3].

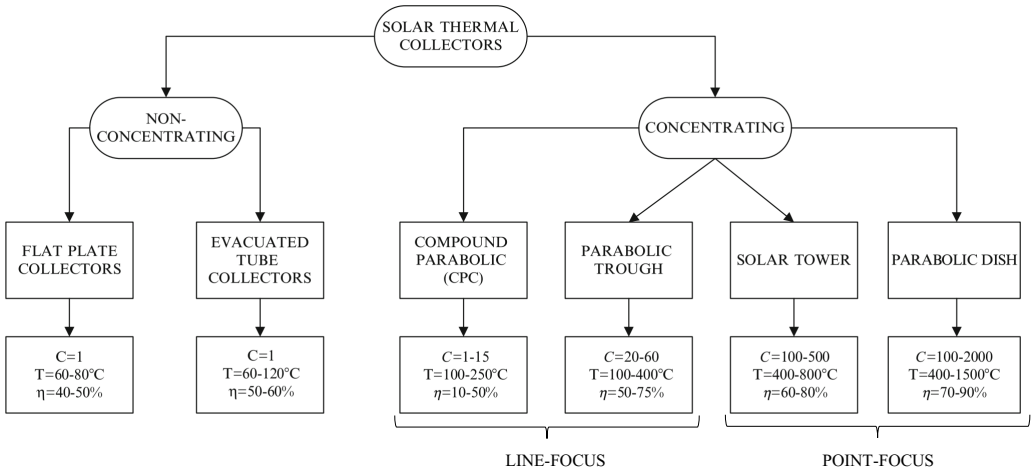

Figure 1.2: Thermal collector technologies used in solar plants [2].

favorable option is solar towers [4]. These are attractive due to its high-efficiency design and lower cost of storage if compared with parabolic troughs. Additionally, solar towers are less sensitive to seasonal variations, and the possibility of changing the size and number of heliostats offers several trade-offs [5].

Regarding costs, the photovoltaic panels are ahead of the other alternatives. Wittenstein *et al.* [5] shows that solar photovoltaic costs have significantly declined over the past years, and cannot be considered as cost outliers. However, it still depends on several factors that influence the final Levelized costs of any given investment [5].

In solar thermal base processes, great scientific challenges need to be solved to find efficient processes to collect, convert, store and use solar energy inside a profitable economic scheme. Two main barriers need to be overcome to achieve these objectives. Firstly, in the case of power generation, prices through this technology are still not competitive compared to conventional processes. Secondly, the natural variation of the solar radiation, meaning it is difficult to ensure the supply when it is required [6, 7].

Regardless the employed technology, the full benefit of renewable alternatives in the future will depend on several factors such as the transformation of the electricity system based on technology advances and new operating procedures, business models, and regulatory approaches [7]. Meaning, therefore, great research efforts are still required to have a strong alternative to conventional non-renewable processes.

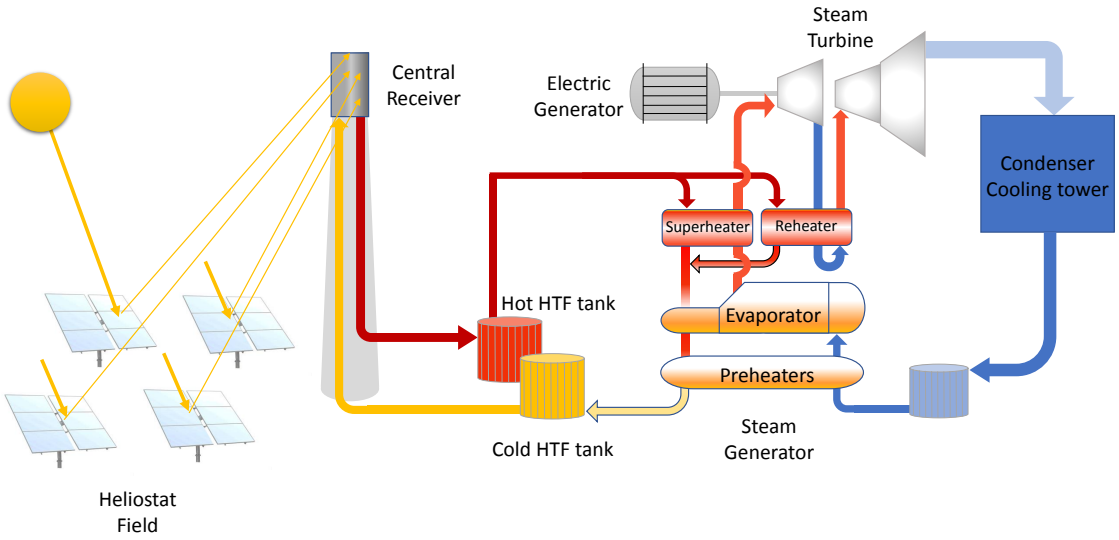

Figure 1.3: General scheme of a solar tower power plant.

1.1 Description of the process

As previously mentioned, alternative technologies that have the potential to replace those based on non-renewable resources still need to grow. In the case of solar thermal approaches to power generation, one of the most promising technologies is central solar towers. This alternative constitutes the center of the research project presented here.

In central-tower thermal power plants, Figure (1.3), an array of large mirrors called heliostats reflects the solar radiation towards a receiver located at the top of a tower. Then a heat transfer fluid flowing through the receiver takes the concentrated radiation and transports the heat to a conventional thermodynamic cycle to generate power [8].

The basic process contains five major subsystems: (1) Field of collectors, (2) Central receiver, (3) Heat transfer system, (4) Thermal storage system, and (5) control system [6]. Even though these are the main subgroups identified in the basic scheme of this process, there are several configurations under study.

In solar power tower plants, the core device is the central receiver at the top of the tower. In this unit, all the solar radiation coming from the solar field is concentrated in a small area. This fact takes the receiver to work under very hard conditions, which at the same time adds uncertainty to its lifetime. During operation, the main problems are tube corrosion, cracks in the welded zones, thermal stresses over the materials, and

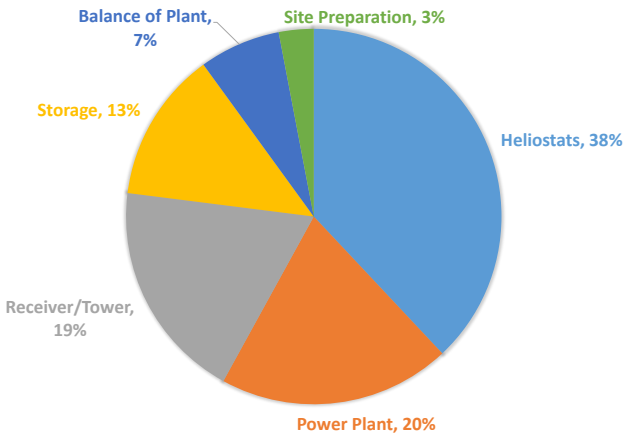

Figure 1.4: Direct costs percentages associated to the development of a solar tower power generation plant [10].

tube overheating especially during radiation transients [9]. Additionally, considering this device represents around 20% of total direct costs (See Figure (1.4)), then a safe operation of this unit is crucial.

There are several kinds of central receivers, one of these are the tubular receivers which can be divided into cavity receivers and external receivers. In a cavity receiver, the radiation coming from the heliostat field goes to an aperture into a box-like structure before reaching the heat transfer surfaces. The active heat transfer areas consist of tubes arrangements in panels around the walls.

In external receivers, the surfaces can be flat or convex toward the heliostat field. In large solar plants, the external receiver resembles a cylinder composed of several panels. As in cavity receivers, each panel contains several pipes where the heat transfer fluid flows. Figure (1.5) shows schemes of these two types of receivers. There are several characteristics that differentiate external and cavity receivers. Radiative losses are usually larger in external receivers due to the hot panels are exposed. Likewise, reflection losses for an external receiver are slightly larger. In regards to spillage losses, cavity receivers present higher values due to the incoming radiation must fit into a small aperture [3, 11].

A third kind is volumetric receivers, which contains a porous material that absorbs the concentrated solar energy. Once solar radiation reaches the absorber section, a gaseous fluid flows through this material which allows transferring from the absorber to the fluid. Advantages of this kind of receiver include its high capacity of absorbing heat flux, which allows heating the fluid at higher temperatures. Figure (1.6) shows the temperature profiles in tubular and volumetric receivers. There are two main configurations for volumetric receivers, open and closed loop. In the open-loop case,

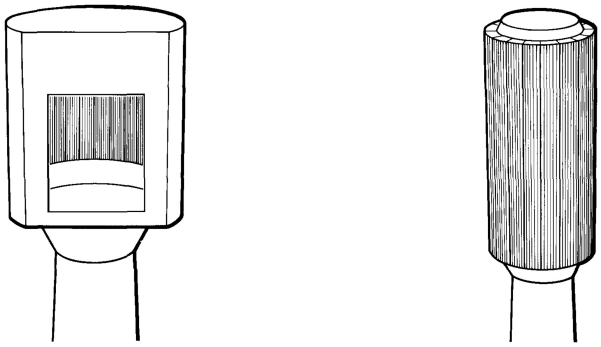

(a) (b)

Figure 1.5: Tubular receivers basic scheme: (a) Cavity Receiver, (b) External Receiver. [11]

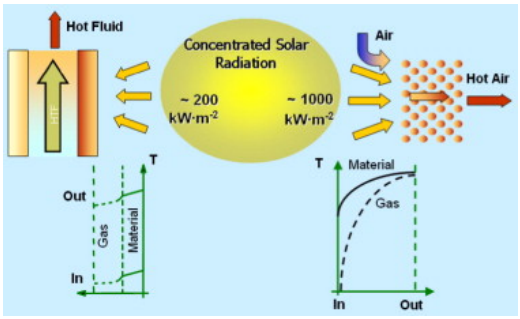

Figure 1.6: Profile temperature comparison between tubular and volumetric receivers [13].

the receiver works using air at atmospheric pressure while the closed loop receiver uses pressurised air [12].

Considering the concentration ratio in solar tower systems is high, the heliostat field must be properly directed to the central receiver to avoid damaging it. Most of the developed approaches base its operation in optimization procedures using models, and then the solution is implemented in an open-loop structure. There are two main drawbacks of these methodologies. Firstly, the uncertainties are given by the model when random disturbances have a significant effect on the process. Secondly, the high computational power required due to the high number of heliostats in a regular solar field.

1.2 Statement of the Problem

The high concentration ratio in solar central receiver systems makes these devices highly vulnerable to solar radiation fluctuations. It is a weakness enhanced by

atmospheric disturbances such as clouds commonly observed at the ground level. Meaning therefore that an improper operation of the system can lead to excessive thermal stresses that can ruin the entire device, a disastrous result considering the high cost of central receivers. Additionally, it is not only about protecting the receiver during disturbances, but the whole process must also be economically sustainable so that it can become a reliable alternative.

Available methodologies to confront this problem involve manipulating heliostats of the solar field to redirect sunlight onto the central receiver. So far the proposed solutions rely on radiation and heat transfer models that require a high computational support to handle the calculations derived from the large amount heliostats in a conventional solar field. Furthermore, since these methodologies operate in an open loop structure, model uncertainties are unavoidably transferred to the actual process. An issue that becomes more critical considering these algorithms are tested under clear sky conditions, an ideal scenario that is not always guaranteed.

1.3 Objectives

1.3.1 General objective

Design a multivariate and adaptive closed loop control strategy that maximizes solar radiation harvesting during cloudiness transients without exceeding the operational or mechanical limits in open solar central receivers.

1.3.2 Specific objectives

- Develop a dynamic model of the central receiver capable of reproducing the behavior of the system during sun radiation transients caused by cloud shading.
- Establish a model that represents the dynamic behavior of the shadows created by moving clouds.
- Design a multivariate closed loop strategy to control temperature/heat flux in the central receiver.
- Analyse the behavior of the control strategy under solar radiation transients due to cloud shading.

1.4 Significance of the Study

There are several outcomes derived from this research project. The main expected result is a methodology that allows the implementation of available closed loop control strategies to promote an appropriate heat flux distribution over the central receiver according to specific constraints. The methodology will reduce the required computational load by decreasing the high amount of degrees of freedom given by the high number of heliostats in a solar field. Even though the analysis will be base on one particular control approach, the methodology can be extended to other regulatory control approaches. After the implementation of the closed loop aiming strategy, the daily operation of the process is not easily influenced by the uncertainties due to natural variability.

Since the robustness of the closed loop needs to be tested under disturbances, the project will also have as an outcome the proposal for a novel cloud shading model to replicate solar transients over a two-dimensional domain. Considering it is designed independently from the control strategy, the model could be used by any other solar process model that requires a transient analysis.

1.5 Limitations in Colombia to implement solar thermal systems

Using alternative renewable energy sources is a priority that is becoming a concern in Colombia. For several years some relevant steps have been taken to promote its inclusion at a residential and industrial level. One of the important points to achieve the development of successful projects is to identify those locations with the best performance for the implementation of different alternatives. In regards to solar energy, the most important contribution is the Atlas of Solar Radiation of Colombia. This project comes from the inter-institutional collaboration of the IDEAM (Instituto de Hidrología, Meteorología y Estudios Ambientales) and the UPME (Unidad de Planeación Minero Energética). Created to obey the Law 697 of 2001, which promotes the rational and efficient use of energy, specifically the Decree 3683 of 2003 referring to the inventory of conventional and non-conventional energy sources. The Atlas contains thirteen maps showing the following variables: (1) Global radiation, (2) Sunshine duration, (3) UV radiation, and (4) Ozone and UV indices. Developing this Atlas was possible using data from 71 meteorological stations distributed in the country. However, due to the data they collected and the period they recorded,

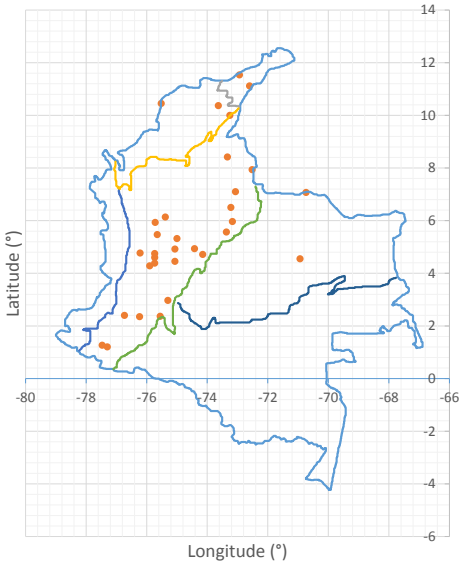

Figure 1.7: Distribution of reference measurement stations used to develop the solar radiation Atlas in Colombia

only 32 of these stations are catalogued as reference stations. Figure (1.7) shows the geographical distribution these stations [14].

Although determining the available solar radiation is vital to develop a solar alternative, in Colombia, the main implementation efforts go to photovoltaic systems. Thus, the maps that have prospered are those of global solar radiation. There is no a reliable source of direct or diffuse direct solar radiation data (direct measurements), which are indispensable for the development of solar thermal concentrating systems.

On the other hand, in Colombia, Law 1715 of 2014 was also approved. The purpose of this law is to promote investment, research and development of clean technologies for energy production, and energy efficiency through tax deductions. It also establishes lines of action for the fulfillment of commitments made by Colombia in the field of renewable energies, efficient energy management and reduction of greenhouse gas emissions, such as those acquired through the approval of the International Renewable Energy Agency (IRENA) through Law 1665 of 2013. This Law that will promote the development of generation systems through Non-Conventional Renewable Energy Sources in Colombia.

However, the road to implementing large-scale systems is quite long and involves much effort. An issue that becomes stronger considering the economic competition with hydraulic based systems currently available in the country.

1.6 Thesis overview

This thesis consists of seven additional chapters. Chapter 2 shows the literature review of control strategies in solar tower systems, explaining the role of these algorithms for sun tracking, to maintain fluid's outlet temperature in the receiver, and to operate the power generation block. Additionally, this chapter describes the approaches adopted in actual solar plants such as Solar Two and the PSA solar tower experience. Chapter 3 shows all the details about the developed model. It indicates the way that the solar radiation is concentrated over the central receiver, then explains the heat transfer phenomenon in the receiver and the stress calculation due to the temperature distribution in the pipes. It also presents a discussion about available simulation platforms, its advantages, and disadvantages in regards to the developed model. It indicates all the characteristics of the case that this thesis studies. Chapter 4 shows the insights of the agent-based cloud shading model. Then it describes the optimization procedure developed to tune the model for obtaining solar transients as in actual data. Chapter 5 displays the core of the whole aiming strategy. It defines the behavior of the aiming points according to predefined rules and the way it links to a multivariate control strategy as the Dynamic Matrix Control approach. Afterward, Chapters 6 & 7 shows the analysis of the control strategy for distributing heat flux following predefined allowable flux profiles, and the strategy working to maintain the temperature in a set point to avoid thermal stresses and corrosion problems. Chapter 8 presents the conclusions achieved after developing the research project. It also explains some following works in the upcoming panorama. Finally, the appendix section names the publications derived from the work developed in this project.

Chapter 2

State of the art: Automatic control strategies in the solar-tower fields

From the standpoint of automatic control, it is required to develop strategies to accomplish the following objectives. (1) Compensate for deficiencies in the construction of the heliostats. (2) Optimize the efficiency of the solar receiver. (3) Minimize human intervention in the control strategy. (4) Maintain temperature gradients as low as possible and below the limits given by the manufacturer of the receiver [15, 16]. One important issue that the control scheme must deal is managing a MIMO (Multiple-Inputs-Multiple-Outputs). It must be done while taking into account important disturbances such as cloud interference at the solar field, which would produce high-temperature peaks at the central receiver if these are not correctly handled. Figure (2.1) shows a general overview of how control strategies are involved in this kind of process.

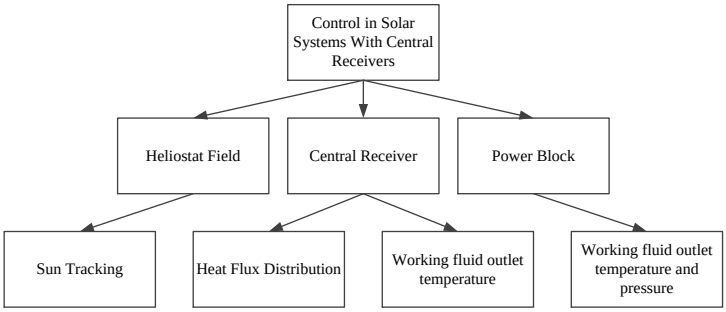

Figure 2.1: General overview of automatic control applied in central receiver solar thermal systems

2.1 Sun tracking

The first main step of this process is to redirect solar radiation over the central receiver, a procedure called sun tracking. Here the control strategy must be able to point the heliostat image to the position given by the central receiver control strategy. Thus, two main approaches have been studied, open loop and closed loop.

2.1.1 Open loop sun tracking

In this method, the relative position of the sun is obtained using a model that takes into account the geographical coordinates of the solar field and the current time. Then, it is possible to calculate the appropriate normal vector of the heliostat, using the solar vector, the coordinates of the heliostat, and the coordinates of the central receiver at the top of the tower. It allows orientating the heliostat in two axes, usually azimuth and elevation. Thus, the control system in each heliostat takes the function of following the position calculated through the model (Setpoint) by measuring the physical position of the heliostat using encoders (Controlled variable). Then it sends a corresponding signal to the motors coupled in the heliostat (Manipulated variable), Figure (2.2) shows its general scheme. Among its advantages it can be said these algorithms can reach the desired degree of precision for these systems, these are also autonomous, and most important its cost is lower than closed loop options. Main drawbacks of this approach rely on the fact that no check is performed to verify that radiation is arriving at the intended point over the target. That is why this method is called open loop because there is no guarantee the intended result has been achieved. Errors in this method can be around $1 - 1.5\,mrad$, sometimes tending to accumulate. Factors that influence these errors can be summarized as follows: [17, 18]

- Heliostat drive tolerances and gear backlash, which is caused by the motion of the heliostat due to its weight. Thus, the entire gear mechanism might rotate against the direction given by the controller.
- Inaccuracy in the tracking model.
- Intervals between heliostat motions due to encoder resolution limitation.
- Structural deformation of the heliostat due to external forces.
- Heliostat foundation shift.

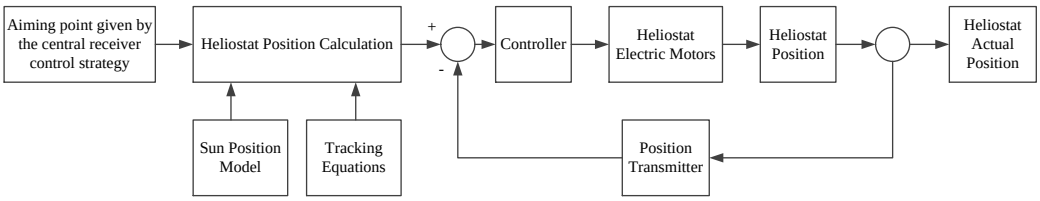

Figure 2.2: General scheme heliostat open loop tracking

- Target center shift due to structure settling of the receiver, or any maintenance operation performed on the receiver or nearby components.
- Time-varying astigmatism and cosine effects.
- Processor accuracy.
- Atmospheric refraction.

Most common formulas used for rotating the heliostats are the Azimuth-Elevation. In these tracking formulas, one rotation axis of the heliostat points to the Zenith, while the another one is perpendicular to the first axis and tangent to the reflector. This method has become popular due it is based on natural observation. However, it has avoided looking into different approaches for concentrating solar radiation. Thus, according to Chen *et al.* [19] a general form for sun tracking can be derived and by applying particular considerations, different sun-tracking methods can be obtained, including Azimuth-Elevation. The error between the real focusing position and the command sent to the heliostat is commonly corrected either manually or automatically. In the manual case, an operator has to change the azimuth and the elevation angles until the heliostat points an auxiliary target. This exhausting task must be repeated with each one of the heliostats. In an automatic mode, one way presented by Berenguel *et al.* [17] uses a black and white camera for determining the position of the centroid of the projected image, then it is compared with the ideal target point, and then the offset is estimated and corrected [6]. It is important to realize even this is an automatic way of correcting the offset; it is done individually for each heliostat. Therefore the whole strategy is still considered open loop.

2.1.2 Closed loop sun tracking

One approach that has also been studied is to implement a closed loop strategy for compensating the offset issue seen in the open loop case. Thus, it is required to

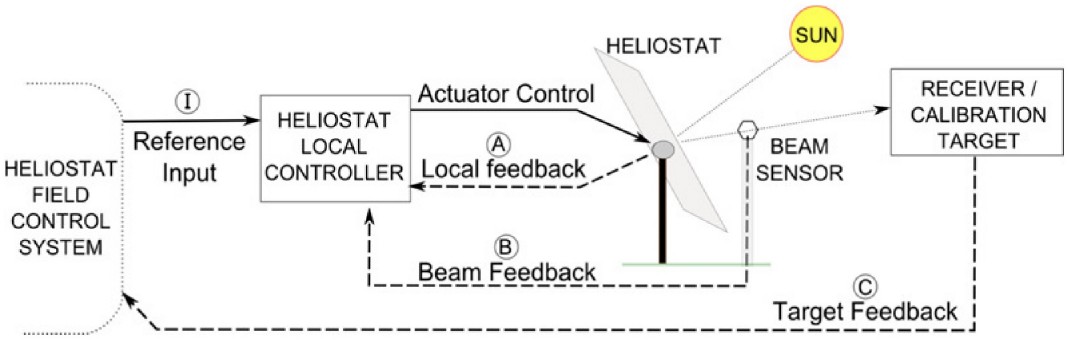

Figure 2.3: General scheme closed loop tracking control strategy [21]

measure the incident radiation given by each heliostat, detect the aiming errors and feedback the appropriate correction, Fig. (2.3) shows the general scheme for this strategy. However, this approach has not been widely used due to the fact it is difficult to distinguish the radiation that comes from any of the different heliostats in the field. Moreover, measuring the flux distribution over the target cannot be used due it contains the radiation that comes from all the heliostats of the field [18]. Additionally, another major issue associated with this strategy relies on maintaining a stable tracking operation in cloudy days [20]. Among approaches seen in literature, using a central sensor around the central receiver, such as a camera or photocells, is one solution for developing a closed loop strategy [20, 18]. However, simultaneously handling all the heliostats is a major problem that needs more research.

An alternative way of carrying out a closed loop control strategy is to implement at each heliostat a sensor that allows moving the heliostat according the sun moves along the day. In the research developed by Quero *et al.* [22], it is presented a sun tracking sensor that overcomes cost related issues by employing a manufacturing method called microelectromechanical system (MEMS). Besides significantly reducing costs, improving the accuracy of the sensor. Fig. (2.4) shows the way this sensor is used in the closed loop strategy.

2.2 Heat flux control over the central receiver

As has been mentioned before, heat flux distribution over the central receiver is a major issue that must be controlled carefully. Implemented solutions indicate the strategy can vary depending on the characteristics of the heating fluid and the type of central receiver. An appropriate aiming strategy should avoid sudden increases in heat flux while generating as much power as possible. Maximum limits depend on

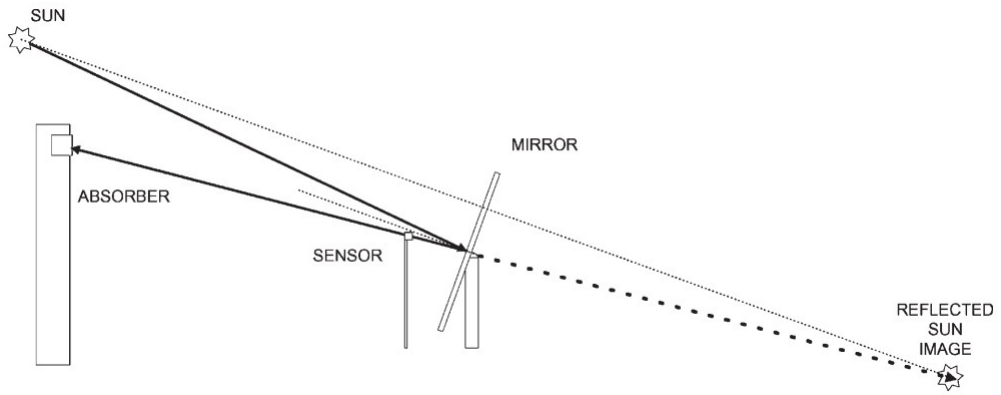

Figure 2.4: Scheme using sensor proposed by Quero *et al.* [22].

the materials used to construct the central receiver, based on its allowable thermal stresses and corrosion limits [23].

2.2.1 Open loop methodologies

Many of the approaches proposed for achieving a desired heat flux distribution are based on optimization procedures. In the research presented by Cruz *et al.* [24], the problem is addressed using a large-scale two-layer optimization. The first layer of optimization determines the available heliostats and initial starting points. In the second layer, using a local gradient optimizer, the error between the reference and the obtained flux map is minimized. Besarati *et al.* [25] presented an optimization method based on genetic algorithms which are used to minimize the standard deviation of the flux density distribution. Salomé *et al.* [26] proposed an open loop control strategy designed and implemented for the THEMIS experimental solar tower in France, which uses the HLFCAL convolution method to develop an iterative seek procedure.

The aiming strategy also varies depending on receiver's design. Sánchez González *et al.* [27] showed a control strategy for external solar receivers using molten salt as the working fluid. The goal of this method was not to achieve a uniform heat flux over the central receiver, but it calculates the Allowable Flux Distribution (AFD) per panel based on thermal stresses and corrosion limits. The core algorithm of this aiming strategy tries to aim heliostats to enhance energy collection and reduce the spillage. It is done by using a search and a fit algorithm. The search algorithm is based on symmetric aiming strategy using receiver's equatorial line as a reference. The goal of this algorithm is to find preliminary aiming factors at each solar field sector. Then the fit algorithm is applied to adjust the preliminary heat flux distribution to the AFD profile.

For the *Solar Two* plant case, which uses molten salt, two heat flux strategies were developed: SAPS (Static Aim Processing System) and DAPS (Dynamic Aim Processing System). Initially, each heliostat is aimed at the vertical centerline of the receiver, then depending on the image characteristics of each heliostat, the amount of shift for each one of them is calculated. Heliostats whose projected image is the smallest will be assigned with the highest changes because its spillage losses are low, while those heliostats with the largest projected images will have the smallest changes. DAPS takes input and output temperatures of the working fluid in the receiver and uses the current aiming points of the heliostats to calculate the flux distribution over the receiver. Then, it compares this flux against the values given by designer's specifications. If there is any excess, the strategy looks for the heliostats pointing to that node and defocus them. The SAPS and DAPS strategies are used for avoiding excessive temperature gradients, and a control strategy was also implemented for controlling molten salt flow rates. Thus, if the outlet temperature or receiver radiation sensors are lower than the predetermined thresholds, which means there is a cloud over the field, then the mass flow valve is totally opened. It allows avoiding sudden peaks in heat flux over the receiver once the disturbance disappears [6, 28, 29].

Besides having the SAPS and DAPS strategies to avoid excessive temperature gradients, it has also implemented a control strategy for maintaining molten salt flow rates depending on its outlet temperature. Since this temperature depends on cloud coverage, then it has two objectives. First, a feedforward loop was designed to ramp salt flow to full to prevent receiver damage rapidly. Second, and probably the most sensitive approach, it is wanted to maintain salt flow at its maximum clear-sky value during periods of total cloud cover. This way, as soon as clouds disappear, adequate salt cooling of the receiver would be guaranteed. In general, the strategy consists of a flow feedback control loop whose setpoint is chosen by a Boolean condition depending on the temperature of the molten salt at the outlet of the receiver and by the radiation sensors (RT) located in the neighborhood of the central receiver. Thus, if the outlet temperature or receiver radiation sensors are lower than the predetermined thresholds, then full molten salt is established. On the other hand, the flow rate is calculated based on the inlet temperature, outlet temperature, and radiation sensors around the receiver. Figure (2.5a) shows the flow control algorithm presented in the SANDIA Report [30], and Fig. 2.5b shows the *P&ID* representation of this algorithm.

Even though these strategies are working at time intervals mentioned before, there are several operating states and transitions among them that are important to carry

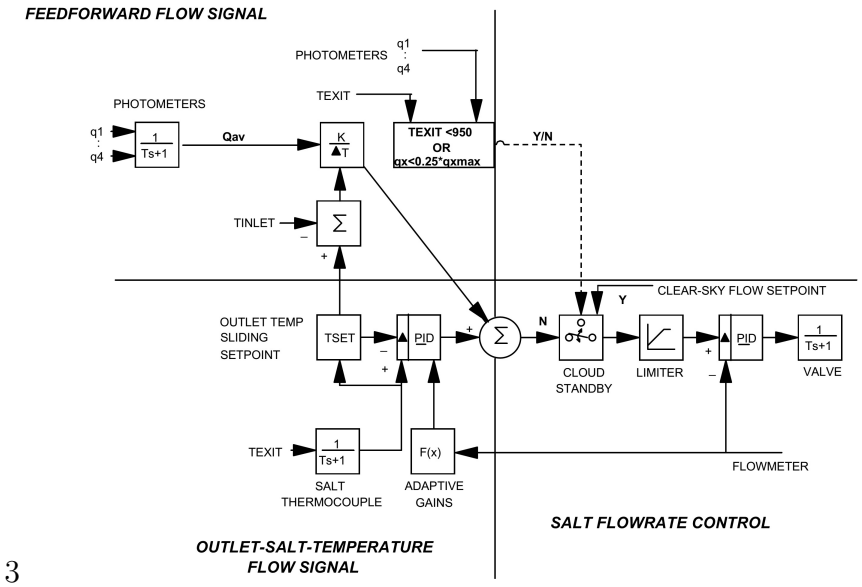

3

(a) Flow control algorithm shown in SANDIA report [30]

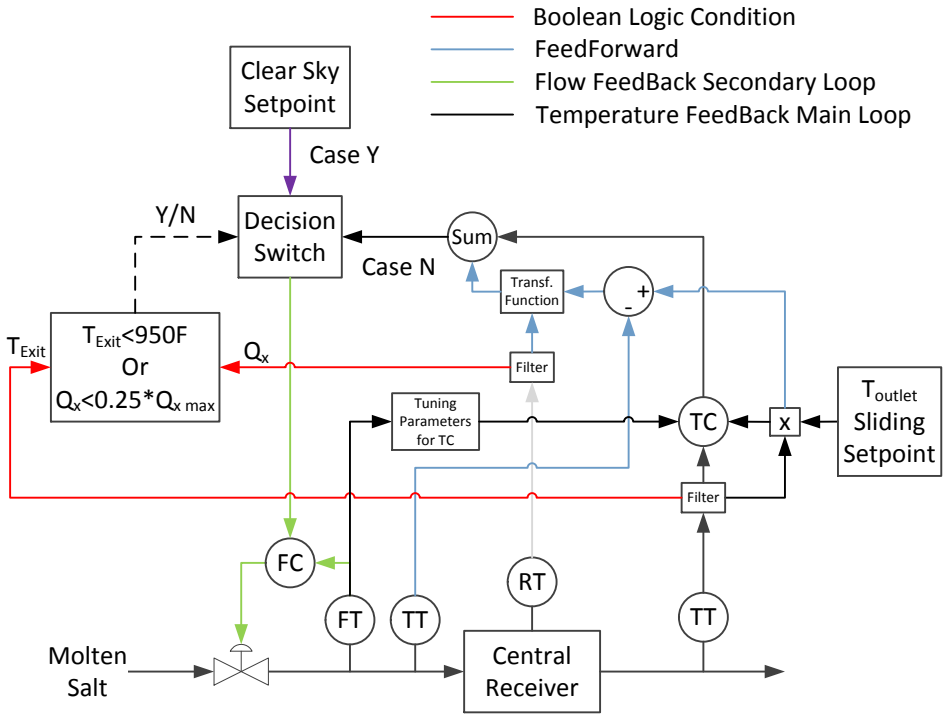

(b) *P&ID* representation of flow control algorithm for central receiver in Solar Two plant.

Figure 2.5: Control Strategy used in Solar Two plant [30]

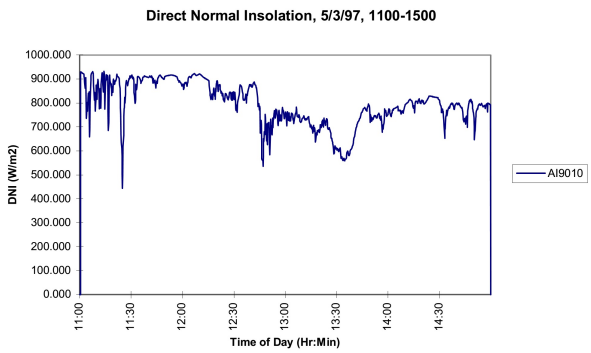

(a) Solar radiation during the test of the strategy

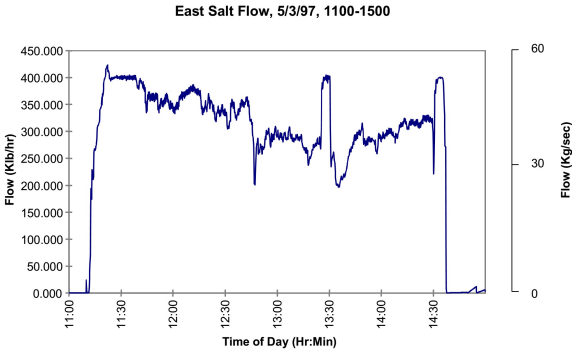

(b) Mass flow while testing the control strategy

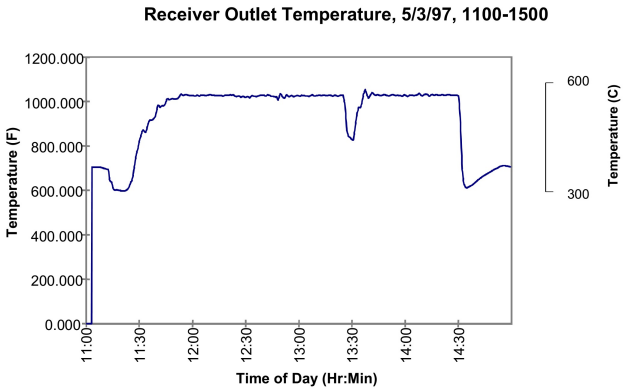

(c) Molten salt temperature at the central receiver outlet

Figure 2.6: Results given by the control strategy implemented in Solar Two Plant

out for the energy collection process. Following state definitions, and transitions belong to the design document for the *Solar Two* plant, published SANDIA Laboratories [28]. Results in Fig. (2.6) indicate the control strategy can maintain temperature relatively stable. Moreover, as exposed in the report, at around 13:30 the strategy enabled the cloud standby. Thus mass flow rate increased suddenly, and consequently, temperature decreased significantly.

2.2.2 Closed loop methodologies

Close loop methodologies to distribute heat flux over central receivers are not popular. A highlighting case is an approach used in the *Plataforma Solar de Almería* (PSA) in Spain. The approach used for controlling the heat flux over the receiver is different from classic automatic control systems. It is less restrictive because it uses an open air volumetric receiver [31], thus the temperature is allowed to move between upper and lower limits. In this case, implemented solution is a heuristic knowledge-based control

strategy. This approach can reproduce the performance of a skilled operator during regular tests. There are 40 thermocouples placed in the volumetric receiver divided into the five aiming points. For each one of those aiming points, the upper and lower boundaries are calculated. It establishes corresponding limits for transitions during start-up. The control strategy has two basic control actions which are: heliostat adjustment and aiming point adjustment. The first control action takes place when an average temperature in an aiming point is much higher than the mean temperature of another one. In this case, one heliostat goes from the hot aiming point to the cold one. The second action implies moving the coordinates of the aiming point. This action is carried out to compensate an important internal disequilibrium within an aiming point influence [31, 6].

To determine if the difference between two aiming points is high, the difference between both aiming points mean indexes must be higher than the threshold. It is important to notice that the only case when there are no available control actions shows up when there is a high difference, but no heliostats are pointing such hot zone. This situation takes place especially during days with high irradiance levels, and overall in central aiming points.

In the case of requiring moving a heliostat, there is a sequence to follow for determining which one is the most suitable to change. First, it searches for a heliostat in the hot point that originally belonged to the cold one. If there is no match, it looks for a heliostat that does not belong to the hot zone. Finally, if there is no match, any heliostat from the hot zone is chosen. Fig. (2.8) indicates the temperature variation for an aiming point over the central receiver in PSA plant [6].

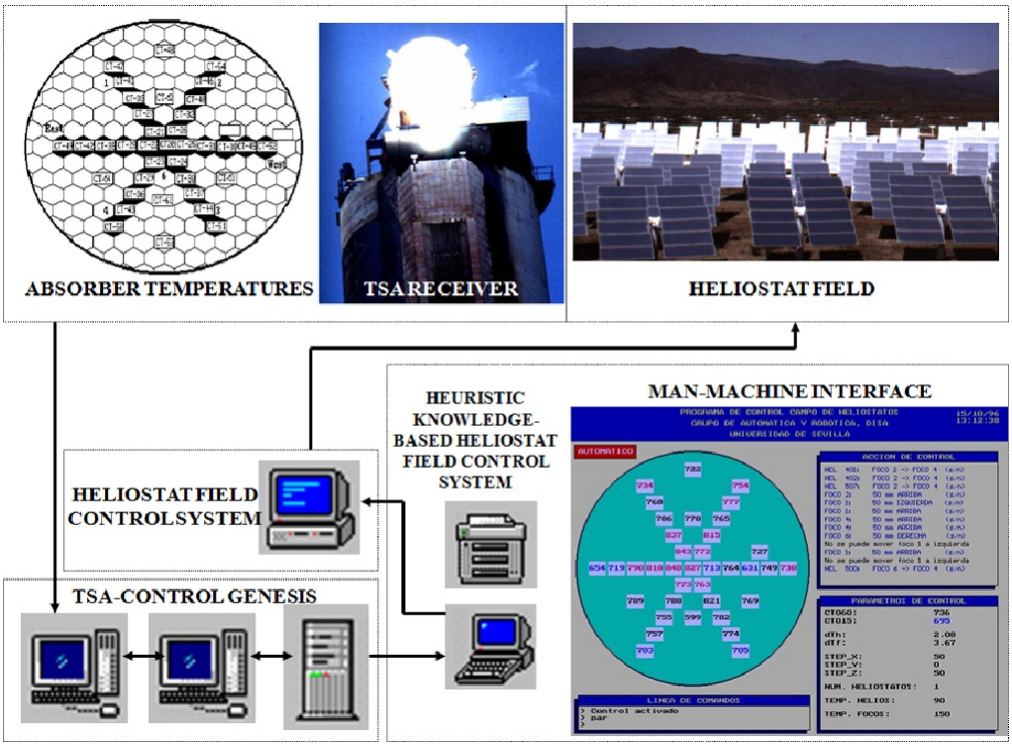

Figure 2.7: Control scheme used in PSA plant for controlling temperature over the central receiver [6].

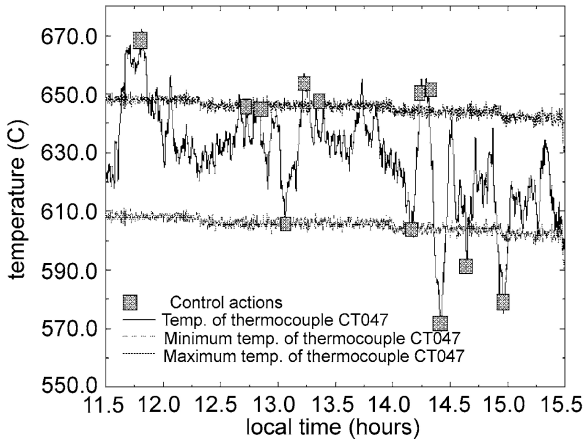

Figure 2.8: Temperature profile for a specific point over the central receiver surface [6].

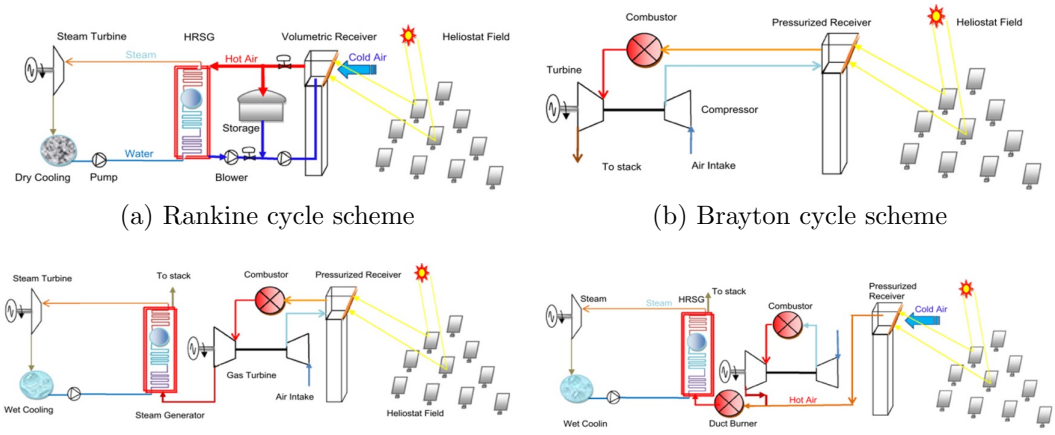

(a) Rankine cycle scheme

(b) Brayton cycle scheme

(c) Combined cycle scheme

(d) Combined cycle scheme

Figure 2.9: Common thermodynamic cycles coupled to the central receiver system [35].

2.3 Power block control strategies

Considering the power block in solar thermal plants has almost the same configuration than in conventional fossil fuel based stations, the control strategies in the conventional case apply to the power block in the solar plant. The most important controlled variables in this system are related to the steam that feeds the turbine. Specifically the steam pressure, superheater outlet steam temperature, and reheater outlet steam temperature. Common control approaches include SISO loops using Proportional-Integral-Derivative (PID) controllers. However, there are also studies that propose other alternatives such as Model Predictive Control (MPC) strategies to enhance the performance of the system [32].

Performance and control strategies implemented in the power block also depend on the cycle used for converting the thermal energy to electricity. Common power cycles used in solar plants are Brayton, Rankine and combined. 2.9 shows different configurations of the power generation systems that can be used in central receiver solar power plants. The main difference between these cycles are the working fluids used. In the Rankine cycle steam is the working fluid, and in the Brayton cycle, it is a gaseous fluid such as air. [33, 34]. It can also bee seen the addition of a combustor in some of these systems, this is an optional device, which is used for carrying out a more efficient process and for suppressing fluctuations in solar radiation.

In PSA power plant it has been established the air power at the input of the steam generator is controlled by manipulating the mass flow provided by blower G_2 ($\dot{m}_2$).

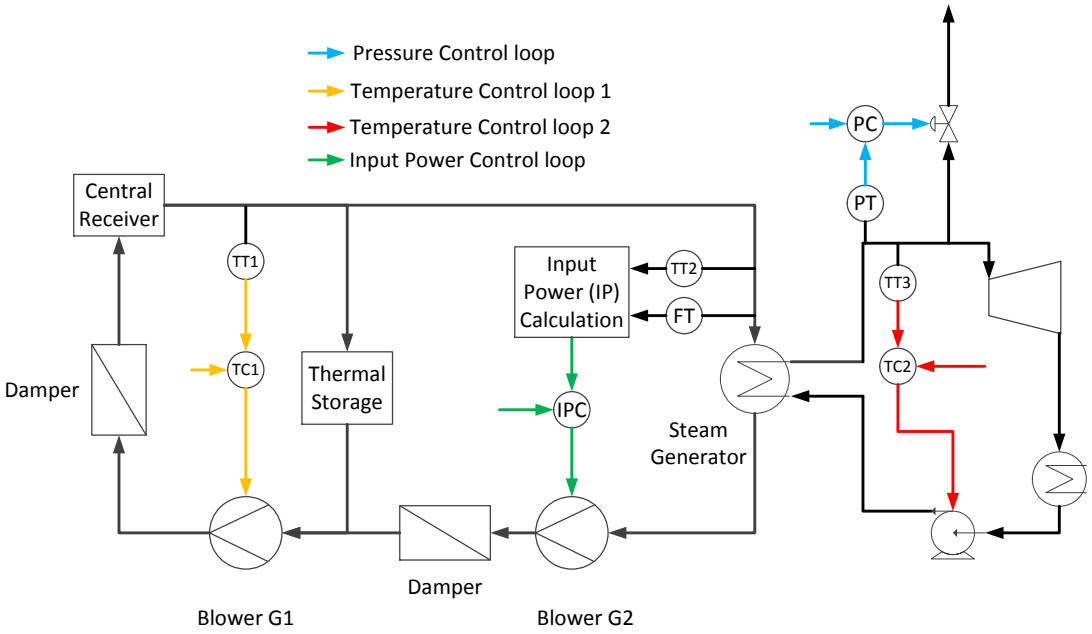

Figure 2.10: Control strategy applied to the power generation cycle in PSA plant

Moreover, an MPC approach is implemented by using the Hybrid Toolbox developed by Bemporad [36]. It allows creating a receding horizon MPC controller solving a Mixed-Integer Programing optimization problem. In this strategy the mass flow given by blower G_1, to control the temperature at the outlet of the central receiver, is considered a disturbance[1]. It also has been reported the particular characteristics of the hybrid process are the main reason for not using a multivariable controller because MIMO systems do not take into account the different operating modes. For the steam generator system, the process requires other two control loops. One of them is in charge of controlling the steam temperature at the outlet of the steam generator by manipulating the water pump at the inlet of the same unit. The second loop is in charge of maintaining pressure at the outlet of the steam generator by manipulating a release valve. Fig. (2.10) shows a general scheme of all these strategies.

[1]The effect of this control loop is hidden in the heat flux control strategy

Chapter 3

Process Model

3.1 Computational platforms for developing solar thermal projects

Modeling, analyzing and optimizing central receiver systems require mastering a user-friendly tool. Unfortunately, a standardized software is not available. So far exists two main branches, there are several codes that require much work to adapt them for studying a specific project, and there are some interactive software packages that allow executing some limited analysis. Regarding developed codes, most popular options are UHC, DELSOL, HFLCAL, MIRVAL, FIAT LUX, and SOLTRACE. Tables 3.1 & 3.2 show the main characteristics of these algorithms [37, 38]. Most of these codes were written in Fortran and under a public license. However, online access to these routines is not easily available. Regarding the interactive software packages, there are some options such as SolarPILOT^{TM}, SAM, and Tonatiuh.

SolarPILOT is a graphical user interface that extends DELSOL3 using the Hermite expansion technique. It applies calculations to each heliostat image, rather than to larger groups of heliostats, and integrates the SolTrace^{TM} ray-tracing engine to analyze more complex geometries [39].

SAM (System Advisor Model) is a performance and financial model developed by NREL and designed to facilitate decision making for people involved in the renewable energy industry. SAM makes performance predictions and cost of energy estimates for grid-connected power projects based on installation and operating costs and system design parameters that can be specified as inputs to the model [40].

Tonatiuh is an open-source object-oriented program developed to assist in the design and analysis of solar concentrating systems. It uses Monte-Carlo Ray tracing, in a distributed computing structure coupled to a 3D user interface that provides a

Table 3.1: Main codes developed to study solar central receiver systems [37, 38]

Code	UHC	DELSOL	HFLCAL
Research team	University of Houston codes	SANDIA	GAST project
Currently used by	SANDIA, Tietronix	CIEMAT, SANDIA	DLR
Availability	Source and and executable version	Source and and executable version	Not available
Programming language	FORTRAN/C++	FORTRAN/Basic	FORTRAN
Flux calculation method	Hermite polynomial expansion/convolution	Hermite polynomial expansion/convolution	Simplified convolution of each heliostat's flux
Receiver type	Flat, cavity or external cylinder	Flat, cavity or external cylinder	Flat, cylindrical or conical

Table 3.2: (Cont.) Main codes developed to study solar central receiver systems

Code	MIRVAL	FIAT LUX	SolTrace
Research team	SANDIA	CIEMAT-PSA	NREL
Currently used by	DLR, SANDIA CRS	CIEMAT, CRS	NREL, CNRS
Availability	Source and executable version	Unknown	Executable version
Programming language	FORTRAN	MATLAB	Delphi5
Flux calculation method	Monte Carlo ray-tracing	Normally distributed random value of slope error	Monte Carlo ray-tracing
Receiver type	Flat, cavity or external	Flat	Almost any receiver configuration

friendly environment for developing many solar thermal projects [41].

There are some advantages and disadvantages of the available options. The software tools previously mentioned are easy to use and computationally efficient. However, these packages show some constraints that limit its integration to other programs such as Matlab. For example, in this project, it is mandatory to develop control strategies whose development is not supported by the solar packages named above. On the other hand, a direct employment of codes allows having a huge flexibility for modeling the process. However, the source files of the developed codes are not easy to find, and user manuals are not available. These circumstances lead this project to develop its codes in a widespread and robust calculation platform such as Matlab.

3.2 Heat flux radiation model

The main objective of this model is testing automatic control strategies, meaning it is necessary to calculate the heat distribution over a central receiver after the heliostat field redirects sun radiation. Figure (3.1) shows a brief scheme of the process. There are several approaches to model this process. These main methods are [42]:

1. Hermite polynomial expansion convolution.
2. Simplified convolution.
3. Normally distributed random value of slope error.
4. Monte Carlo ray-tracing (MCRT).
5. Radiation methods.

One of the most accurate methods is to apply Monte Carlo ray tracing (MCRT). However, it requires robust computational hardware. Another common method is the HFLCAL because it shows accurate results as the MCRT. HFLCAL is based on the research developed by Kiera [43] and modified by Schwarzbözl *et al.* [44]. The calculated heat flux is based on a circular normal distribution [26, 45] as shown in Eq. (3.1). HFLCAL calculates the heat flux distribution maps based on two main parameters:

1. The amount of power reflected by the heliostat.
2. A global deviation based on the Gaussian standard distribution for the sun shape, the reflected beam on the heliostat, the tracking error, and the astigmatism of the mirror surface.

The heat flux over the receiver must take into account the apparent position of the sun, location heliostats on the solar field, and the target coordinates on the receiver [26]. Therefore, it is necessary to define a set of equations to take into account several parameters such as the sun position, the blocking and shadowing effect, optical properties of the heliostats material, heliostats position, and atmospheric conditions, among others. Figure (3.2) shows a scheme of the model to be developed.

Besides these advantages, it has also been used to optimize solar field distributions, where it shows good results. Thus, it is considered appropriate for the purpose of this investigation. The HFLCAL method is based on the research developed by Kiera [43]

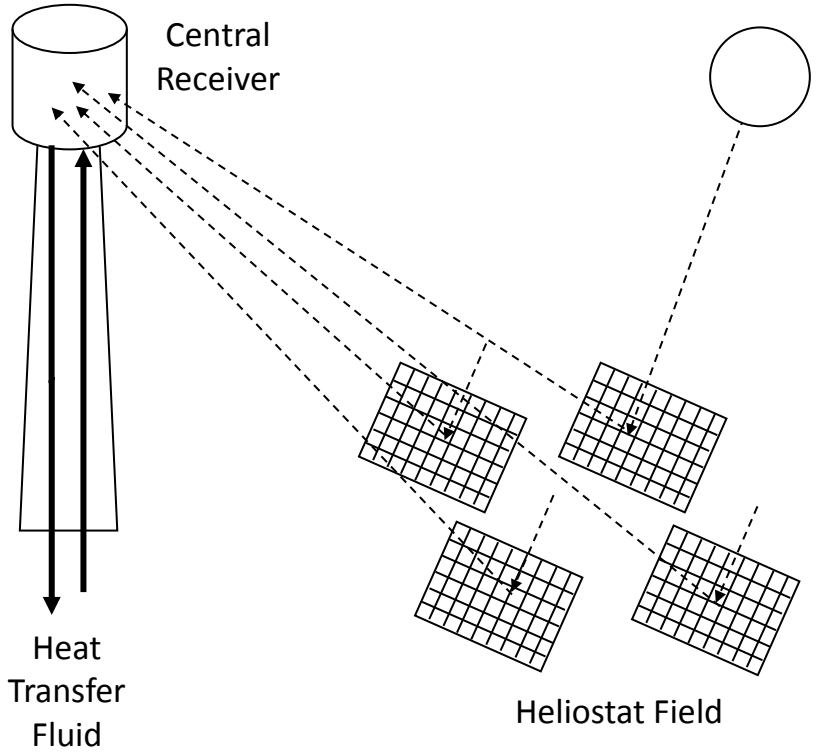

Figure 3.1: Basic scheme of the process

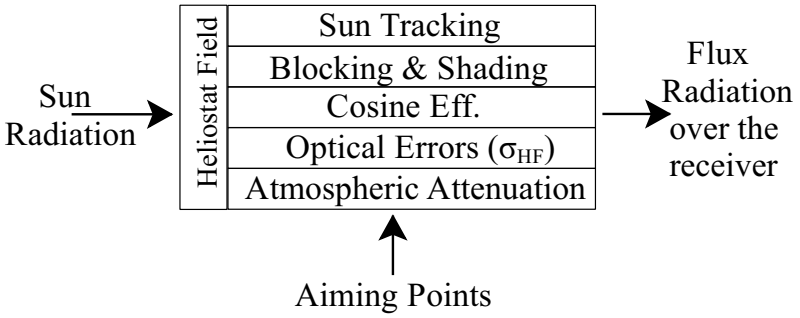

Figure 3.2: Main features accounted in the developed model.

and modified by Schwarzbözl *et al.* [44]. This heat flux is based on a circular normal distribution as it is shown by Eq. (3.1) [45, 26].

$$Flux_{HF} = \frac{P_H}{2\pi\sigma_{HF}^2} e^{-\frac{(x-x_{AP})^2+(y-y_{AP})^2}{2\sigma_{HF}^2}} \tag{3.1}$$

where P_H is the total solar power concentrated by the heliostat mirror at the receiver surface. σ_{HF} represents the total effective deviation, x and y are the coordinates of the receiver's surface, and the coordinates x_{AP} and y_{AP} are used to specify the aiming point at the receiver surface. Equation (3.2) is used to obtain the reflected power. Where I_D represents the DNI (Direct Normal Irrandiance, kW/m^2). A_H is the mirror area of the heliostat. w is the incidence angle between the sun ray vector and the normal vector to the heliostat surface. f_{at} is the attenuation factor due to atmospheric conditions which also depends on the distance (D) between the heliostat and the receiver, this dependence is given by Eq. (3.3) [46]. f_{bs} is the blocking and shading factor between heliostats, it is calculated according to the procedure shown in subsection 3.2.3. Finally, ρ represents the reflectivity of the heliostat mirror.

$$P_H = I_D \cdot A_H \cdot cos\,(w) \cdot f_{at} \cdot \rho \cdot f_{bs} \tag{3.2}$$

$$f_{at} = \begin{cases} 0.99321 - 0.000176 \cdot D + 1.97 \times 10^{-8} D^2 & D \leq 1000\ m \\ e^{-0.0001106 \cdot D} & D > 1000\ m \end{cases} \tag{3.3}$$

The total effective deviation (σ_{HF}) is obtained as the convolution of three Gaussians distributions. This expression is shown in Eq. (3.4), which is the same used by Sánchez-González [47]. It is done in order to validate the results given by developed model against the data shown in [47]. The first distribution is used to represent solar radiation density (σ_{sun}), which decreases as it reaches the edge of the sun disc [44]. The second distribution is related to the beam quality (σ_{slp}), which takes into account deviations of the mirror curvature from ideal shape and imperfections due waviness and roughness. The third distribution takes into account the tracking errors (σ_t) which are caused by a finite motor step size, tolerances of the gear boxes and wind loads on the structure.

$$\sigma_{HF} = \sqrt{D^2 \cdot \left(\sigma_{sun}^2 + 2 \cdot (1 + \cos w) \cdot \sigma_{slp}^2 + \sigma_t^2\right)} \tag{3.4}$$

3.2.1 Sun Position

For calculating relative sun position, the algorithm used is a code available at Matlab® web page [48]. This code was implemented based on the report created by the National Renewable Energy Laboratory (NREL) [49]. It allows obtaining the solar Zenith and Azimuth angle in the period from the year -2000 to 6000 with uncertainties of ± 0.0003 and is based on the equations published by Jean Meeus [50]. Thus the Azimuth angle is obtained from the North to East, and the Zenith angle calculated from the vertical, being both angles in degrees.

3.2.2 Tracking Equations

Tracking the sun is another important aspect that must be taken into account for this model. Regular heliostats are devices capable of rotating around two axes, in this way the most common formulas used for rotating the heliostats are the Azimuth-Elevation equations. In these tracking formulas, one rotation axis of the heliostat points to the Zenith, while the another one is perpendicular to the first axis and tangent to the reflector. This method has become popular because it is based on natural observation. However, it has avoided looking into different approaches for concentrating solar radiation. According to Chen *et al.* a general form for sun tracking can be derived and by applying particular considerations, different sun-tracking methods can be obtained, including Azimuth-Elevation [19]. Equations (3.5) and (3.6) show the expressions developed by Chen for the rotation around both axes of the heliostat.

$$\theta_H = \frac{\pi}{2} - \arcsin \left[\frac{\begin{array}{c} -\sin\alpha\left(\cos\Phi\cos\delta\cos\Omega + \sin\Phi\sin\delta\right) - \cos\alpha\sin\zeta\cos\delta\sin\Omega \\ +\cos\alpha\cos\zeta\left(-\sin\Phi\cos\delta\cos\Omega + \cos\Phi\sin\delta\right) \\ +\sin\alpha\sin\lambda + \cos\alpha\sin\zeta\cos\lambda\sin\phi + \cos\alpha\cos\zeta\cos\lambda\cos\phi \end{array}}{2\cos w} \right] \tag{3.5}$$

$$\rho_i = \arcsin \left[\frac{\begin{array}{c} -\cos\zeta\cos\delta\sin\Omega + \sin\zeta\left(\sin\Phi\cos\delta\cos\Omega - \cos\Phi\sin\delta\right) \\ +\cos\zeta\cos\lambda\sin\phi - \sin\zeta\cos\lambda\cos\phi \end{array}}{2\cos w\ \cos\beta_H} \right] \tag{3.6}$$

where:

ζ: Rotation angle of heliostat normal surface vector from Noth to East about Zenith axis in the Earth surface frame.
α: Vertical angle of heliostat normal surface vector from the horizon in the Earth surface frame.
λ: Altitude angle of target-heliostat vector about the Earth surface.
ϕ: Target-heliostat rotation angle about Zenith from North toward East about the Earth surface.
Φ: Local latitude.
δ: Declination angle of the sun.
Ω : Solar hour angle.
w: Incidence angle.
β_H: Defined as $\pi/2 - \theta_H$.
θ_H, ρ_i: Rotation angles around the chosen axes.

Thus tracking equations can be classified into two main categories. First, without correlation between heliostat axes and target, where the most famous case is the Azimuth-Elevation tracking formulas. Second, with the correlation between heliostat axes and target, where one of the most important are the Spinning-Elevation tracking formulas. Differences among these cases come from using special values on parameters α, ζ, λ, and ϕ. Table 3.3 shows different tracking formulas and the particular values used for deriving them and some advantages for using them.

Table 3.3: Conditions used for obtaing different tracking formulas. [19]

Category	Name	Conditions	Major Advantages
Without correlation between heliostat axes and target	Azimuth Elevation	$\alpha = -90°$	Vertical Mounted
	Polar Mounted	$\alpha = \Phi$ $\zeta = 180\,°$	Nearly single-axis tracking for $\phi = 180°$
With correlation between heliostat axes and target	Spinning Elevation	$\lambda = \alpha$ $\phi = \zeta$	Minimum aberration effect
	Latitude Oriented	$\lambda = \alpha = \Phi - 90\,°$ $\phi = \zeta = 180\,°$	Maximum solar power collection; minimum aberration effect
	Polar Oriented	$\lambda = \alpha = \Phi$ $\phi = \zeta = 180\ °$	Single-axis traking; minimum aberration effect

3.2.3 Blocking and Shading

Changes in sun's position have as a consequence that some heliostats avoid sun radiation to reach the surface of heliostats in its neighborhood once the shading takes places. In other cases sun radiation reflected by a heliostat does not reach the central receiver due to the interference of heliostats near it, so the blocking effect is dominant. This efficiency is quantified using the procedure presented by Sassi [51]. First, it is required to project heliostats' centers around the studied heliostat following the sun vector for determining the shading, and following the heliostat-receiver vector for calculating blocking. This projection is obtained by solving the equation system formed by the straight line expression and the studied heliostat plane. That is, two equations come from the following straight-line expression:

$$\frac{x - x_0}{V_x} = \frac{y - y_0}{V_y} = \frac{z - z_0}{V_z} \tag{3.7}$$

where x_0, y_0, and z_0 represents the points (centers of the neighbor heliostats) that are projected to the surface of the studied heliostat. Values V_x, V_y, and V_z are the components of either the sun vector (for shading) or the heliostat-receiver vector (for blocking). The third equation used is the plane of the studied heliostat (Eq. (3.8)), which is known provided its normal vector is determined through the tracking equations. In this equation x_c , y_c , and z_c are the coordinates of the studied heliostat.

$$n_x \cdot (x - x_c) + n_y \cdot (y - y_c) + n_z \cdot (z - z_c) = 0 \tag{3.8}$$

Once the projection is obtained, the system must be properly rotated to have the normal vector of the plane pointing the Z-axis. It allows plotting the heliostat real dimensions around each projected point. Therefore, the percentage of area covered by neighborhood heliostats over the studied heliostat is proportional to the blocking-shading factor. This procedure assumes heliostats are parallel planes, which is less favourable than the actual situation. However, it improves the calculation time of the algorithm [52].

3.2.4 Projection of concentrated solar radiation over the central receiver

Solar radiation distribution calculated through Eq. (3.1), represents the solar radiation in a plane perpendicular to the vector formed between heliostats and the central receiver, as shown in Fig. (3.3). Therefore, it is required to project this distribution

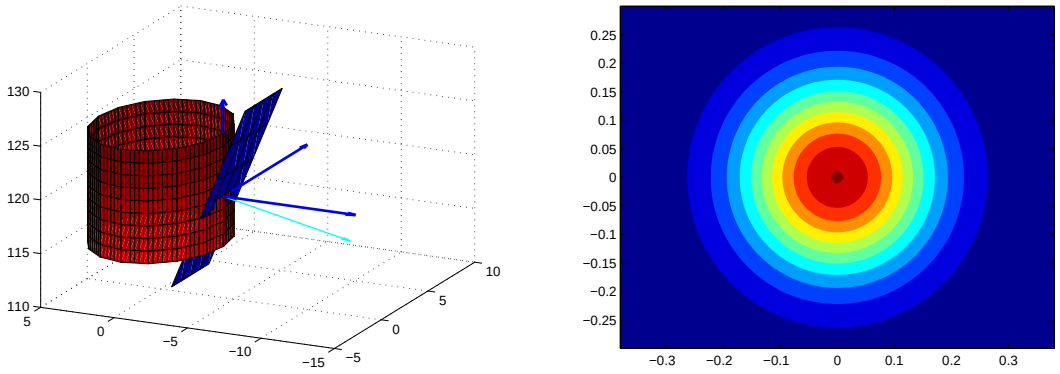

(a) (b)

Figure 3.3: (a) Perpendicular plane to the vector heliostat-central receiver, (b) Gaussian distribution of solar radiation in the perpendicular plane (Eq.(3.1))

over the surface of the central receiver. This projection can be made using the same procedure shown by Sassi [51]. That is, each point of the central receiver is projected into the perpendicular plane using the vector formed between the receiver and the heliostat. Then the set of points is the rotated for obtaining a $2D$ representation, and the radiation distribution is calculated using Eq. (3.1). Finally, it is noteworthy that the amount of radiation over receiver's surface depends on the angle between the normal vector of the receiver surface and the receiver-heliostat vector (ω_p), therefore:

$$F_{Receiver} = F_{Perpendicular} \cdot \cos \omega_p \tag{3.9}$$

3.2.5 Model Validation

This project uses the same configuration studied by Sánchez - González *et al.* [27]. This configuration has the main features found in Gemasolar Solar Field located in Spain. Table 3.4 shows details of the solar field. This research uses two approaches for comparing results. Firstly, the heat flux distribution using an equatorial aiming strategy is compared with the data available from the reference model proposed by Sánchez - González [27]. Table 3.5 shows the approximate amount of energy that one pipe in the receiver could gain. It is calculated by using the cosine effect between the arriving heat flux and the pipe surface. It is assumed the half of the pipe is receiving radiation and the other half is insulated. The pipe surface is divided into several

nodes along the axial and angular dimensions. Then the total absorbed radiation is obtained through a numerical integration.

The results show that the proposed model obtained lower energy than the reference model. This difference is noticeable at the initial four panels. This result leads to the second approach of comparison. Differences might be due to either the cosine efficiency or the blocking and shading effect. Therefore, the developed algorithm is compared at different hours during summer solstice against the results given by Solar Pilot © [39]. Figure (3.5) displays the deviation percentages for the cosine efficiency, indicating that these differences are small.

Figure (3.6) shows the deviation percentages of the blocking and shading effect. This comparison shows that there are noticeable differences between the reference and the proposed models. The blocking and shading effect is seen in Fig. (3.7) shows that the differences between the reference and the proposed model are lower using the blocking and shading factor obtained from Solar Pilot. Regarding spillage loss and the maximum heat flux point along the day, Table 3.6 shows that there are small discrepancies between the models.

With regards to the field efficiency, η_{field}, its variation along the day is shown in Table 3.7. These values are obtained using the ratio between the total heat reaching the central receiver, $Q_{Rec,\,Inc}$, and the total solar radiation that is reaching the solar field, $Q_{Field,\,Inc}$. An approximate value of this efficiency is calculated by using Eq. (3.10), since this way is based on average values, there is a slight discrepancy on the developed model.

$$\eta_{field} = \eta_{bs} \cdot \eta_{\cos} \cdot \eta_{Refl} \cdot \eta_{clean} \cdot \eta_{at} \cdot (1 - \eta_{spillage}) \tag{3.10}$$

where:

η_{bs}: Blocking and shading efficiency.

$\eta_{\cos}$: Cosine efficiency.

η_{Refl}: Mirror reflectivity.

η_{clean}: Mirror cleanliness.

η_{at}: Atmospheric attenuation.

$\eta_{spillage}$: Spillage efficiency.

Even though the proposed model shows some discrepancies with the reference model, it is important to highlight its advantages. Firstly, this model will be used to test aiming strategies, which means that flexibility is required to manipulate and integrate all the components of the solar field in a dynamic iterative loop. It is a characteristic that is restricted in available software packages. Secondly, the control

Table 3.4: Main characteristics used for modeling Gemasolar Solar Field [46, 27]

Parameter	Value
Location	Andalucía, Spain
Latitude	$37.56N$
Number of Heliostats	2650
Field distribution	See Fig. 3.4
Reflective Area per Heliostat	$115.7\ m^2$
Heliostat height	$9.752\ m$
Heliostat width	$12.305\ m$
Mirror reflectivity	0.88
Mirror cleanliness	0.95
Standard deviation of sunshape (σ_{sun})	$2.51\ mrad$
Standard deviation of surface error (σ_{slp})	$2.6\ mrad$
Standard deviation of tracking error (σ_{trk})	$2.1\ mrad$
Receiver's diameter	$8.5\ m$
Receiver's number of panels	18
Heliostat pedestal height	$5\ m$
Height from ground until receiver's equator	$125\ m$
Total optical height (THT)	$120\ m$
Day under study	Summer solstice

strategy to be implemented by this research is developed independently of the model used. It means that despite these differences, the proposed aiming strategy could be implemented without constraints in any central solar receiver system.

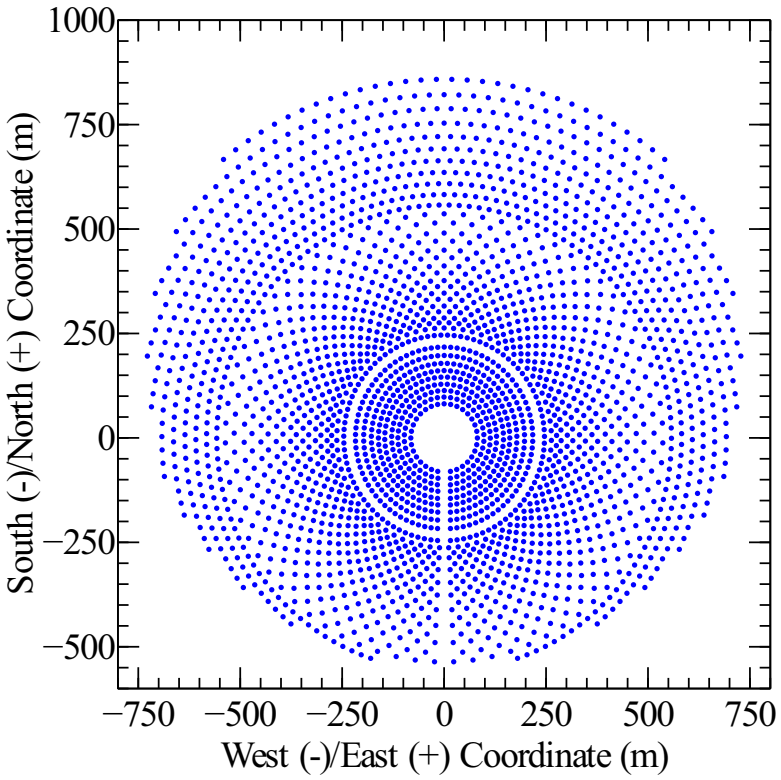

Figure 3.4: Gemasolar heliostat distribution. Data taken from [27]

.

Table 3.5: Energy reaching the receiver panels using an equatorial aiming strategy at summer solstice noon. Reference model [27]

Panel	Developed Model (MW)	Reference Model (MW)	Deviation (%)
W_1	0.449	0.478	-6.07
W_2	0.44	0.469	-6.18
W_3	0.427	0.454	-5.95
W_4	0.409	0.431	-5.10
W_5	0.388	0.402	-3.48
W_6	0.364	0.375	-2.93
W_7	0.338	0.343	-1.46
W_8	0.315	0.315	0.00
W_9	0.291	0.294	-1.02
Total	3.421	3.561	-3.93

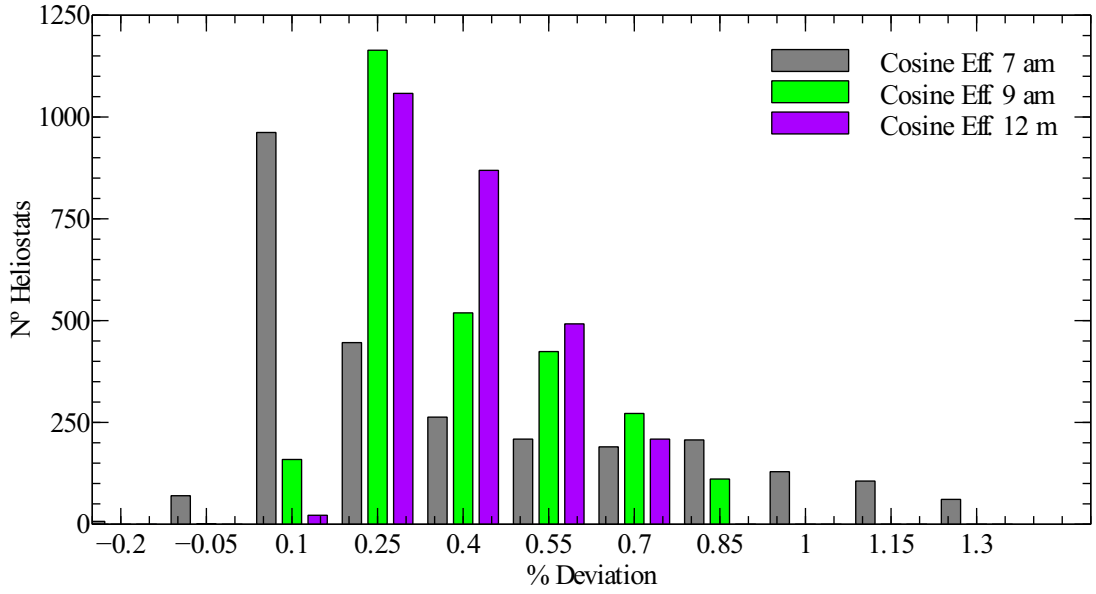

Figure 3.5: Cosine efficiency deviation respect results using Solar Pilot at different solar times

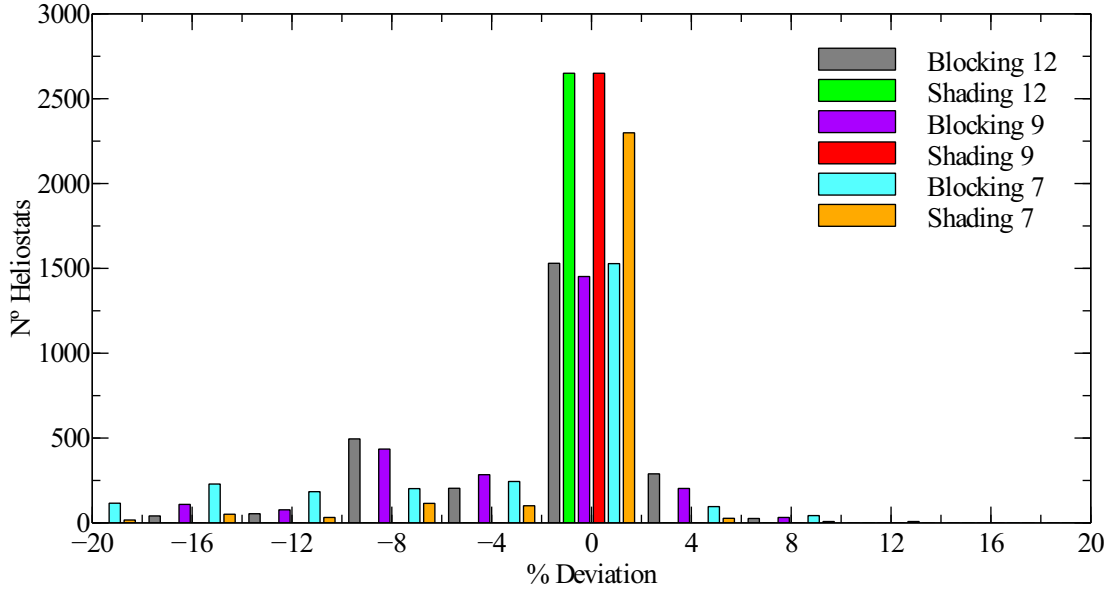

Figure 3.6: Blocking and Shading deviation respect results using Solar Pilot at different solar times

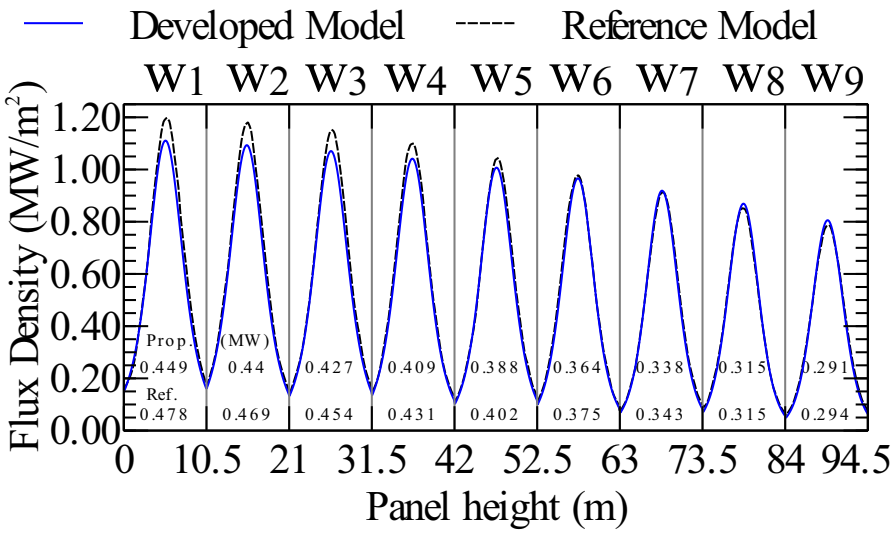

Figure 3.7: Flux density profiles comparison throughout West panels with equatorial aiming at summer solstice noon. Ref. Model [27]

Table 3.6: Equatorial aiming comparison between reference and developed models at different solar times (ST). Reference model [27]

ST	DNI (W/m^2)	Reference Model		Developed Model		Developed Model using f_{bs} from Solar Pilot	
		F_{max} (MW/m^2)	$\eta_{Spil.}$ (%)	F_{max} (MW/m^2)	$\eta_{Spil.}$ (%)	F_{max} (MW/m^2)	$\eta_{Spil.}$ (%)
6	600	0.533	20.7	0.500	19.6	0.526	19.6
7	770	0.880	19.8	0.786	19.0	0.890	18.4
8	860	1.060	19.1	0.962	18.6	1.070	18.1
9	910	1.157	18.7	1.057	18.6	1.146	18.2
10	920	1.188	18.3	1.086	18.7	1.158	18.3
11	930	1.210	18.2	1.105	18.7	1.168	18.3
12	930	1.208	18.1	1.121	18.7	1.164	18.4

Table 3.7: Field efficiency variation along the day for the proposed model

Solar time	Proposed Model	Proposed Model using f_{bs} from Solar Pilot
6	31.21	32.73
7	38.52	41.40
8	42.56	45.20
9	45.01	47.12
10	46.75	48.40
11	47.82	49.16
12	48.32	49.43

3.3 Central receiver's heat transfer model

The central receiver studied here has a 360° cylindrical tubular configuration [53, 54]. Each panel is composed of a bundle of pipes where the heat transfer fluid goes from a temperature around 290 °C until it reaches around 565 °C. Figure (3.8) exhibits a basic sketch of this receiver. Table 3.8 presents the main characteristics and design parameters for modeling the receiver.

Since the model to be developed requires taking into account the transient operation, modeling the whole receiver as in the real process is a difficult task that requires a strong hardware support. Hence, it is required to make some simplifications and assumptions. The first important simplification proposes to study the temperature variations over only one pipe per panel. Then it is assumed all pipes within the same panel have the same temperature distribution. The side effect of this assumption is not significant due to heat flux per panel is very similar. For example, Figure 3.9a shows the heat flux distribution over a central receiver (E_n, W_n: East and West side panels respectively). The same information can be displayed as seen in Fig. 3.9b, where each line in the same panel represents heat flux for a differential element along the width of the panel. Then it is possible to observe that differences are small, which means that all the pipes receive around the same amount of energy. Consequently, temperature distribution over all the pipes can be considered the same.

The second assumption considers that the heat transfer takes place as shown in

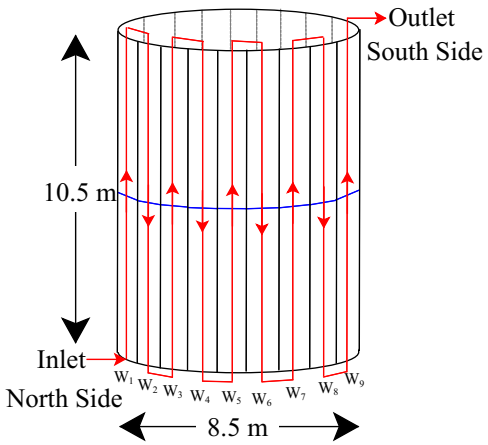

Figure 3.8: Basic scheme of the modeled open central receiver

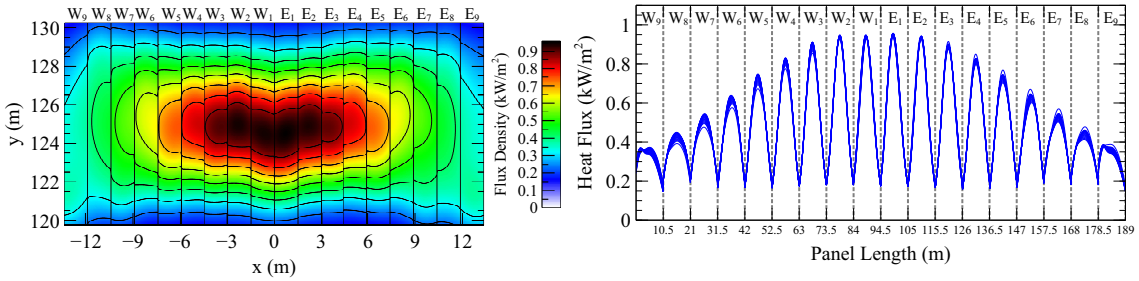

(a) (b)

Figure 3.9: (a) Unfolded heat Flux map over the a central receiver, (b) Heat Flux distribution for every differential element in the x direction along the panel length (y direction)

Fig. 3.10. It is considered energy coming from the field perpendicularly hits an imaginary plane parallel to the receiver. The heat input to the pipe is due only to the energy coming from the solar field, taking into account the angle between incoming solar radiation and the surface of the pipe. Energy losses considered in this model are due to the reflectivity of the absorber paint, to radiation, and to convection. It is considered that the back of the pipe is insulated, and there is no radiation between adjacent pipes.

In this way, the temperature distribution in the pipe, T_w, can be obtained using the equation of energy with constant density and thermal conductivity in the cylindrical coordinate reference system. [55]

$$\rho_w \cdot C_{p_w} \cdot \frac{\partial T_w}{\partial t} = k_w \cdot \left[\frac{1}{r} \cdot \frac{\partial}{\partial r} \left(r \cdot \frac{\partial T_w}{\partial r} \right) + \frac{1}{r^2} \cdot \frac{\partial^2 T_w}{\partial \theta^2} + \frac{\partial^2 T_w}{\partial z^2} \right] \tag{3.11}$$

Table 3.8: Main characteristics and design parameters used to model the open molten salt receiver

Parameter	Value	Parameter	Value
Receiver height (m)	10.5	Number of flow paths	2
Receiver diameter (m)	8.5	Number of panels	18
Pipe external diameter (mm)	42.2	Pipes per panel	32
Pipe wall thickness (mm)	1.65	Sky emissivity, ϵ_{sky}	0.895
Pipe separation (mm)	2	Ground emissivity, ϵ_{gr}	0.955
Salt inlet temperature (°C)	290	Emissivity of absorber paint, ϵ_{abs}	0.9
Salt outlet temperature (°C)	565	Reflectivity of absorber paint, ρ_{abs}	0.03
Ambient temperature (°C)	25	Sky temperature (°C)	20
Material	Inconel 625		

$$\rho_f \cdot Cp_f \cdot \left(\frac{\partial T_f}{\partial t} + Vz \cdot \frac{\partial T_f}{\partial z} \right) = A_i \cdot \bar{h}_f \cdot (T_{w_{inner}} - T_f) \tag{3.12}$$

Where:

T_w: Temperature distribution in the pipe.

ρ_w, ρ_f: Density of the pipe and density of the fluid.

k_w: Thermal conductivity

Cp_w, Cp_f: Heat capacity of the pipe and the fluid.

T_f: Fluid's temperature.

Vz: Fluid's velocity.

Solving previous *PDE* requires following boundary conditions:

- Inner side of the pipe:

$$k_w \cdot \left. \frac{\partial T_w}{\partial r} \right|_{inner} = \bar{h}_f \cdot (T_{w_{inner}} - T_f) \tag{3.13}$$

- Outer side of the pipe:

$$k_w \cdot \left. \frac{\partial T_w}{\partial r} \right|_{outer} = q_{inc} - q_{loss} \tag{3.14}$$

- Heat losses:

$$\dot{\mathbf{q}}_{loss} = \rho_{abs} \cdot \dot{\mathbf{q}}_{inc} + \dot{\mathbf{q}}_{loss,rad} + \dot{\mathbf{q}}_{loss,conv} [=] \frac{W}{m^2} \tag{3.15}$$

The Heat transfer coefficient inside the pipe, $\bar{h}_f$, is calculated as follows:

$$\bar{h}_f = \frac{Nu_f \cdot k_f}{2 \cdot r_{inner}} [=] \frac{J}{s \cdot m^2 \cdot K} \tag{3.16}$$

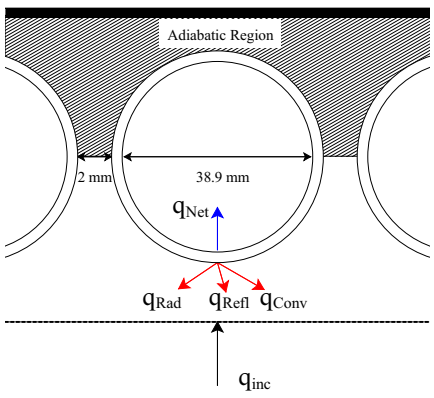

Figure 3.10: Heat transfer considered for modeling the molten salt receiver

The Nusselt number for the fluid is calculated using the Dittus & Boelter correlation [56]:

$$Nu_f = 0.023 \cdot Re_f^{0.8} \cdot Pr_f^{0.4} \tag{3.17}$$

$$Re_f = \frac{\rho_f \cdot v_f \cdot 2 \cdot r_{inner}}{\mu_f} \tag{3.18}$$

$$v_f = \frac{\dot{m}}{\rho_f \cdot \pi \cdot r_{inner}^2} \tag{3.19}$$

$$Pr_f \quad = \quad \frac{Cp_f \cdot \mu_f}{k_f} \tag{3.20}$$

Following molten salt properties correspond to 60% $NaNO_3$ - 40% KNO_3, and can be found in [57, 58]:

$$\mu_f = \frac{22.714 - 0.12 \cdot T_f + 2.281 \times 10^{-4} \cdot T_f^2 - 1.474 \times 10^{-7} \cdot T_f^3}{1000} \,[=]\, Pa \cdot s,\; T_f \,[=]^\circ C \tag{3.21}$$

$$k_f = 0.443 + 1.9 \times 10^{-4} \cdot T_f \,[=]\, \frac{W}{m \cdot K},\; T_f \,[=]^\circ C \tag{3.22}$$

$$Cp_f = 1443 + 0.172 \cdot T_f \,[=]\, \frac{J}{kg \cdot K},\; T_f \,[=]^\circ C \tag{3.23}$$

$$\rho_f = 2090 - 0.636 \cdot T_f \,[=]\, \frac{kg}{m^3},\; T_f \,[=]^\circ C \tag{3.24}$$

Radiation losses can be determined as follows:

$$\dot{\mathbf{q}}_{loss,\,rad} = \epsilon_{abs} \cdot \sigma \cdot \left[T_{w_{outer}}^4 - T_a^4\right],\; T_{w_{outer}}, T_a \,[=]\, K \tag{3.25}$$

$$T_a^4 = \frac{\epsilon_{sky} \cdot T_{sky}^4 + \epsilon_{gr} \cdot T_{amb}^4}{\epsilon_{sky} + \epsilon_{gr}},\; T_{sky}, T_{amb} \,[=]\, K \tag{3.26}$$

$$\sigma = 5.6704 \times 10^{-8} \frac{W}{m^2 K^4} \tag{3.27}$$

Convection losses are calculated as:

$$\dot{\mathbf{q}}_{loss,\,conv} = h_{loss} \cdot (T_s - T_{amb}) \tag{3.28}$$

Where the heat transfer coefficient is formed by the natural and forced convection, h_{nc} and h_{fc} respectively [59].

$$h_{loss} = \begin{cases} \left(h_{nc}^{3.2} + h_{fc}^{3.2}\right)^{\frac{1}{3.2}} & \rightarrow v_{wind} > 0 \\ \\ h_{nc} & \rightarrow v_{wind} = 0 \end{cases} \tag{3.29}$$

The forced convection coefficient is calculated as Eq. (3.30), using the Churchill and Bernstein correlation in Eq. (3.31) [60].

$$h_{fc} = \frac{Nu_{fc} \cdot k_{air}}{D_{rec}} \tag{3.30}$$

$$Nu_{fc} = \frac{0.3 + 0.62 \cdot Re_{air}^{0.5} \cdot Pr_{air}^{0.33}}{\left[1 + \left(\frac{0.4}{Pr_{air}}\right)^{\frac{2}{3}}\right]^{\frac{1}{4}}} \cdot \left[1 + \left(\frac{Re_{air}}{282000}\right)^{\frac{5}{8}}\right] \tag{3.31}$$

$$Re_{air} = \frac{\rho_{air} \cdot v_{wind} \cdot D_{rec}}{\mu_{air}} \tag{3.32}$$

The natural convection term is analogously obtain as:

$$h_{nc} = \frac{Nu_{nc} \cdot k_{air}}{H_{rec}} \tag{3.33}$$

$$Nu_{nc} = 0.098 \cdot \frac{\pi}{2} \cdot Gr_H^{\frac{1}{3}} \cdot \left(\frac{T_w}{T_\infty}\right)^{-0.14} \tag{3.34}$$

$$Gr_H = \frac{g \cdot \beta_{air} \cdot (T_s - T_\infty) \cdot H_{rec}}{\nu_{air}^2} \tag{3.35}$$

$$Cp_{air} = 1006 \, \frac{J}{kg \cdot K} \tag{3.36}$$

$$k_{air} = 0.026 \, \frac{W}{m \cdot K} \tag{3.37}$$

$$\rho_{air} = 1.184 \, \frac{kg}{m^3} \tag{3.38}$$

$$\mu_{air} = 1.845 \times 10^{-5} \, \frac{kg}{m \cdot s} \tag{3.39}$$

$$\beta_{air} = 0.003363 \, \frac{1}{K} \tag{3.40}$$

Therefore, Fig. (3.11) shows the steady state temperature distribution using an equatorial aiming strategy.

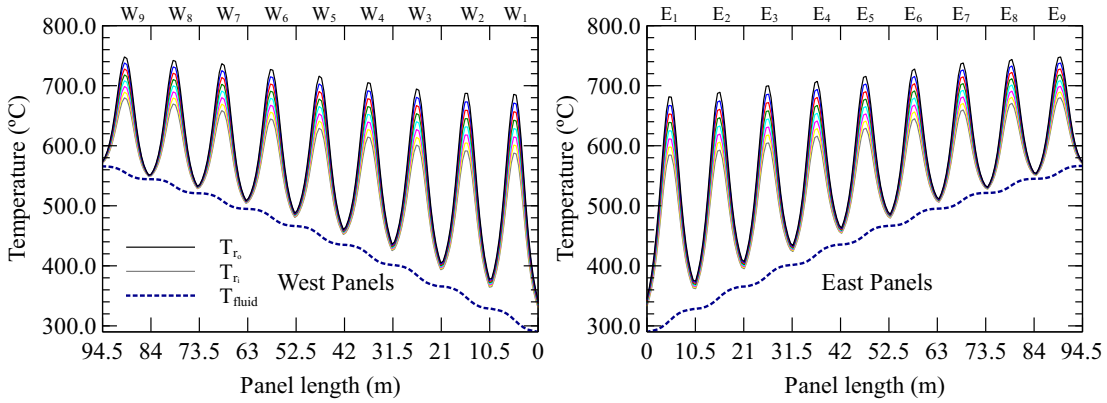

(a) Temperature profiles along pipe's length at the front section of the tube ($\theta = 0°$) and at several radial locations

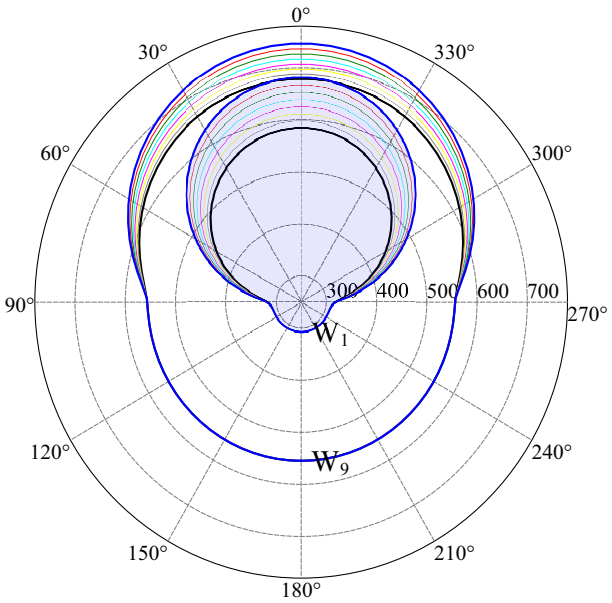

(b) Temperature profiles for several angular and radial locations at the middle section of panel W_1 and W_9

Figure 3.11: Temperature profiles over receiver's pipes and fluid using an equatorial aiming strategy

3.4 Stress Model

Determining the maximum heat flux input that the receiver can handle requires calculating the maximum thermal stresses in the pipe. This research follows the approach shown by Jin-Soo Kim *et al.* [61], which explains that the highest stress in the central receiver's pipes is the tangential stress located on the inner front surface of the pipe. That stress value is obtained as follows:

$$\sigma_{\theta\theta_{Total}} = \sigma_{\theta\theta_{Thermal}} + \sigma_{\theta\theta_{Pressure}} \tag{3.41}$$

The tangential pressure stress is calculated as:

$$\sigma_{\theta\theta_{Pressure}} = \frac{P_i \cdot {r_i}^2}{{r_o}^2 - {r_i}^2} \left(1 + \frac{{r_o}^2}{r^2}\right), \tag{3.42}$$

where P_i is the pipe internal pressure, and r_i & r_o are the inner and outer pipe radius. The tangential thermal stress is obtained following the analytical solution for nonaxisymmetrically heated pipes [61, 62, 63] as:

$$\begin{aligned}\sigma_{\theta\theta_{Thermal}} =& \frac{\alpha \cdot E \cdot B_0}{2 \cdot (1-\nu)} \left[-1 - ln\left(\frac{r}{r_i}\right) + \frac{r_o^2}{r_o^2 - r_i^2} \cdot \left(1 + \frac{r_i^2}{r^2}\right) \cdot ln\left(\frac{r_o}{r_i}\right)\right] \\ &+ \frac{\alpha \cdot E \cdot r}{2 \cdot (1-\nu) \cdot (r_i^2 + r_o^2)} \cdot \left(3 - \frac{r_i^2 + r_o^2}{r^2} - \frac{r_i^2 \cdot r_o^2}{r^4}\right) \cdot \\ &\cdot (C_0 \cdot \cos\theta + D_0 \cdot \sin\theta),\end{aligned} \tag{3.43}$$

where α is the thermal expansion coefficient, E represents the modulus of elasticity, and ν is the Poisson's number. The values of these parameters for the Inconel 625 are 1.51×10^{-5} m/m-K, 1.68×10^5 MPa, and 0.321 respectively. The coefficients A_0, B_0, C_0, C_1, D_0, D_1, C'_0, C'_1, D'_0, and D'_1 are obtained using the temperature distribution data from the heat transfer model (at the inner and outer side of the pipe), and a curve fitting procedure using the following analytical distribution:

$$\begin{aligned}T(r,\theta) =& A_0 + B_0 \cdot ln\left(\frac{r}{r_i}\right) + \left(\frac{C_0}{r} + C_1 \cdot r\right) \cdot \cos\theta + \left(\frac{D_0}{r} + D_1 \cdot r\right) \cdot \sin\theta \\ &+ \left(\frac{C'_0}{r^2} + C'_1 \cdot r^2\right) \cdot \cos 2\theta + \left(\frac{D'_0}{r^2} + D'_1 \cdot r^2\right) \cdot \sin 2\theta\end{aligned} \tag{3.44}$$

Figure (3.12) shows the maximum allowable temperature due to thermal stresses for the Inconel 625 using ASME data from Boiler & Pressure Vessel Code [64]. Hence, the maximum allowable inner wall temperature for receiver's pipes is the

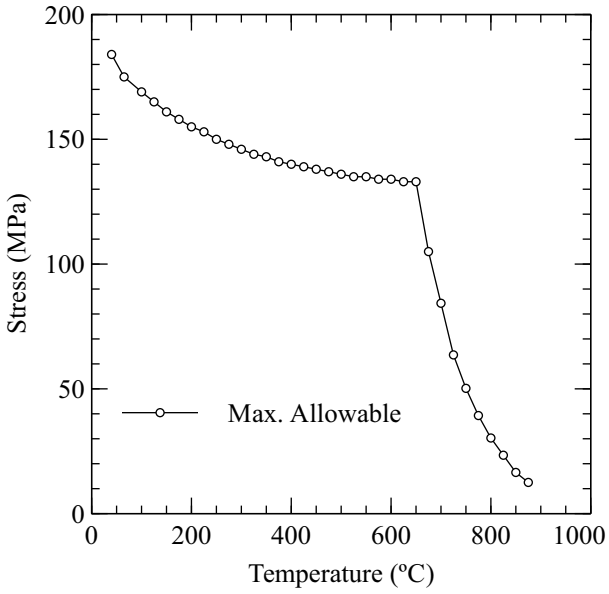

Figure 3.12: Maximum allowable stress values for Inconel 625. Data taken from [64]

minimum value between the allowed temperature due to the thermal stress, and the corrosion limit caused by the high-temperature molten salt (630°C, [27, 65]). Figure (3.13) shows these profiles for the equatorial aiming strategy temperature distribution presented above. These profiles indicate that the corrosion limit is more critical than the stresses caused by the temperature gradient.

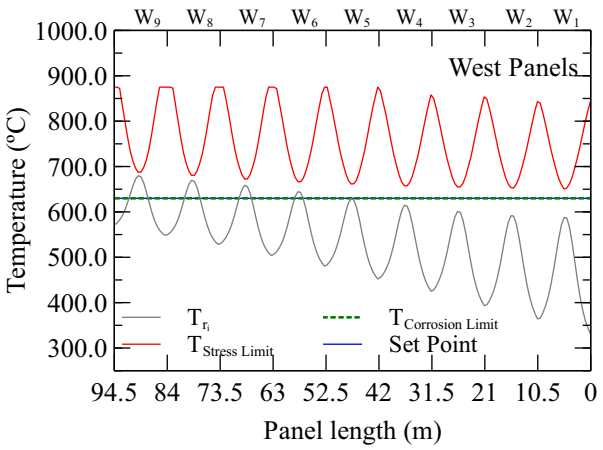

(a)

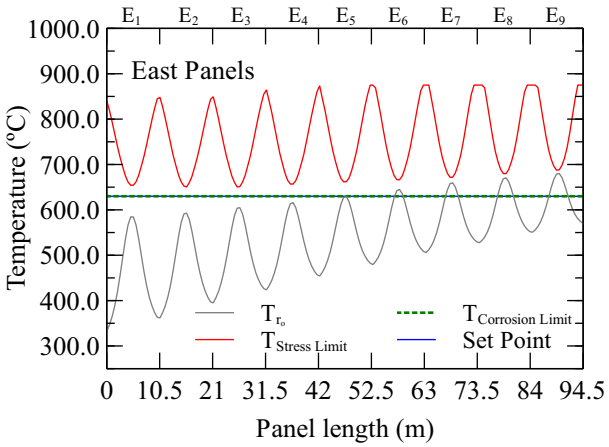

(b)

Figure 3.13: Maximum allowable temperature profile for receiver's pipes using the equatorial aiming temperature distribution.

Chapter 4

Modeling cloud shading: A biomimetic approach

Clouds are a complex phenomenon which is the result of the interaction of several parameters. These are defined as a type of hydrometeor, that is, a group of liquid or solid water particles suspended in the air. According to the World Meteorological Organization (WMO), clouds classification has *ten* different groups depending on the height of the cloud [66]. Names of these groups come from Latin roots such as stratus (*layer*), cumulus (*heap or puffy*), cirrus (*curl of hair*) [67]. Modeling this phenomenon using physical principles has been proposed by many investigations based on momentum, continuity, and energy balances. Various studies have shown that this kind of approach is useful for studying the impact of variables such as temperature, pressure, and velocity on cloud formation [67, 68, 69, 70]. In this way, after implementing the model, it is possible to determine the shading patterns over the surface. However, this complex model calculates several physical variables, and therefore solving these partial differential equations is computationally demanding. For this reason, several approaches are using graphic tools for modeling clouds and that consequently are useful for developing cloud shading. Among these approaches, there are some visual tools which use the same principles drawn up in computer games. Examples of these methods are the polygon, procedural noise, textures sprite, metaball, particle system, or voxel volumes. Wang *et al.* [71] showed that these methods could be combined to obtain better results.

There are several impacts of clouds on the earth. One of these is the attenuation of solar radiation, mainly the direct normal irradiance [72, 73]. Several approaches for taking into account clouds in the solar radiation analysis have been proposed. Some of them are built to match data from specific places and then develop solar radiation maps [74, 75]. Arias-Castro *et al.* [76] analyzed the solar radiation changes

through the representation of clouds as a set of circles. These rings are spread in a two-dimensional space following the similar spatial Poisson process. Another approach is shown by [77], in which clouds are represented by fractal surfaces truncated at different heights. There are also models whose core consists of a statistical analysis of time data series or all-sky images to predict solar radiation changes [78, 79].

Solar radiation changes throughout the day caused by clouds are commonly sudden and highly heterogeneous. Some models have proposed to study the effect of clouds over a solar field by using a plane that completely covers the area, therefore radiation goes from its clear-day value to zero, and it is maintained in this lower limit value [80]. However, clouds are moving most of the time, and in some cases, they might not impact the entire solar field. Therefore this kind of approach may not be suitable.

Studying the transient effect of clouds movement on the solar field requires developing a flexible model which can emulate the dynamic of this type of phenomena. The cloud shadows model allows studying the dynamic performance of solar plants while there are various changes in solar radiation over the solar field.

This project develops a cloud shading Agent-Based Model (AbM) through a biomimetic approach, explicitly based on a bacterial growth colony. In this kind of models, agents are taken into either single-member or multiple-member groups. AbMs do not require specifying a global growth law such as the exponential, instead, according to the rules given to the agents for interacting with its environment, and then the growing global law will emerge [81]. The proposed model is evaluated both qualitative and quantitative by comparing it with real cloud images and the fractal model proposed by [77].

Figure 4.1 presents a graphical explanation of the developed model in this research. This image illustrates the movement of a cloud at two different times (t_1 and t_2). In time t_2 the cloud is located in another place and has a different shape as compared to the same cloud at time t_1. Likewise, the individuals of a bacteria colony are initially located in a place, and then they move and reproduce according to the characteristics of their surroundings. Therefore, the dynamic of the bacterial growth colony has the potential to match the general behavior of cloud shading over a period by using a simple mathematical structure which requires a little computational usage.

4.1 Proposed model

As defined by [81], agent-based models may fall in four main categories: *scale models*, *ideal-type models*, *analogical models*, and *equation-based models*. Hence the proposed

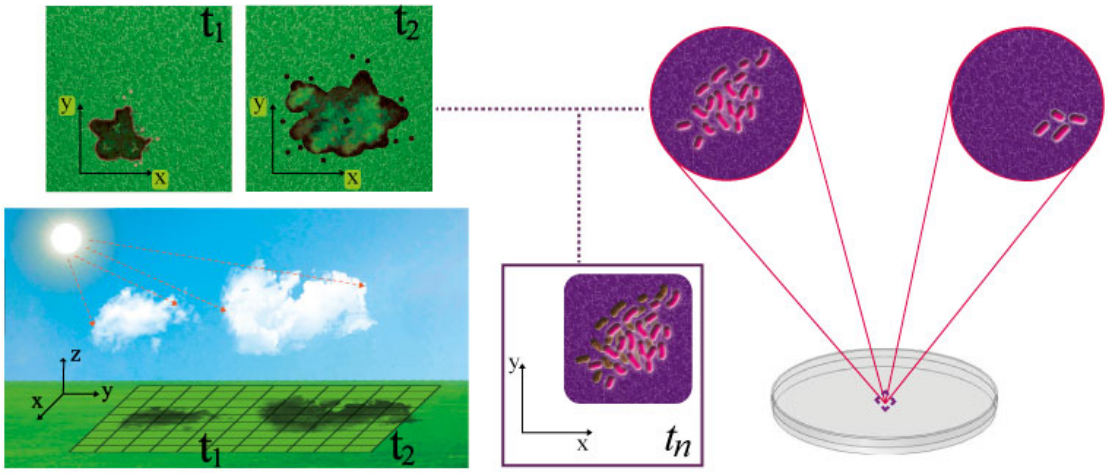

Figure 4.1: Graphical representation of the analogy between bacterial colony growth and cloud-shading dynamics used in the model proposed at this research.

model fits two of these categories *analogical* and *ideal-type*. First, because it accomplishes an analogy between the bacterial-growth system and the cloud-shading phenomenon, and second due to some of the characteristics of the model are simplified.

The implemented model is based on the research developed by [82], and its rules are dominated by interactions such as substrate consumption, metabolism, and maintenance behavior of each agent. Although it is well known that bacteria colonies use quorum sensing mechanisms for growing and moving, this model does not include either the representation of the self-inducing communication molecules or its effect on the colony. The main features to be accomplished are:

1. Dynamic behavior (movement and shape) for representing the cloud shading
2. Easy implementation
3. Uses little computational resources.

4.1.1 Implemented interactions among agents

The interactions for the bacterial analogy model are explained more broadly to maintain a more general and appealing terminology for an easier comprehension. The following characteristics represent the behavior of agents:

- Modification of its surroundings: Agents are spread over a heterogeneous surface, this characteristic gives them the ability to change that surface. It can

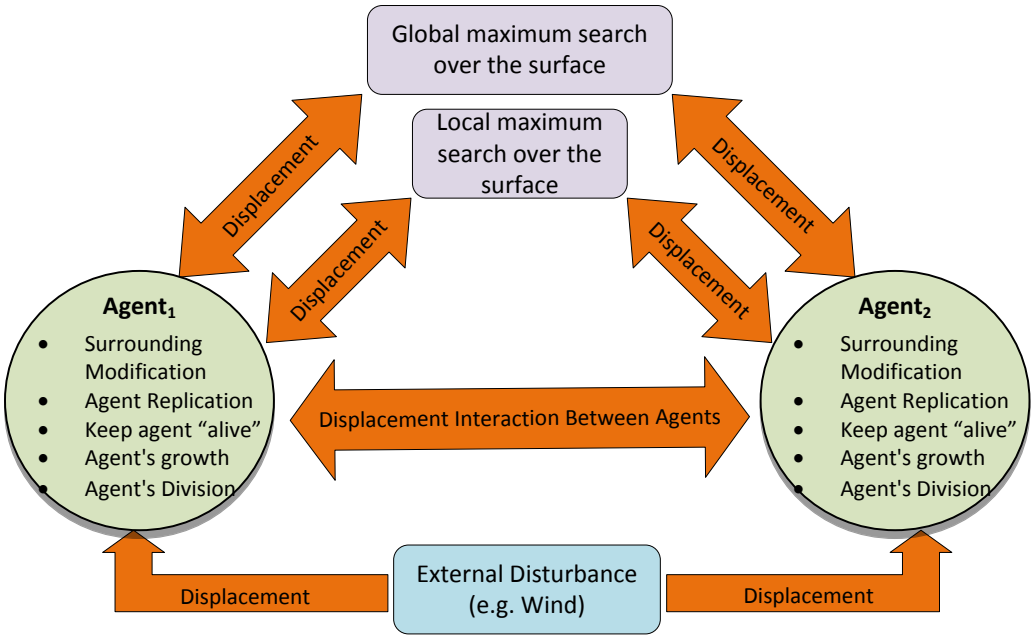

Figure 4.2: Features integrated into the proposed model. Each agent changes according the features implemented while interacting with its surroundings.

be seen as a representation of *"food"* consumption. This feature allows cloud shades to change its size and shape over time and space. The rate of change for this feature depends on:

  - Replication of the agent within the simulation.
  - Keeping the agent *"alive"*.

- Displacement: This component enables agents to move in the spatial domain. As explained in following subsections, it allows linking the model to real parameters such as wind patterns. Additionally, in conjunction with the surrounding-modification feature, it gives to the clouds shades a spatiotemporal thickness distribution, which is related to the transmissivity of the clouds.

Those elements are explained in following subsections. Figure 4.2 shows a scheme about the integration of all the features added to the model. As seen, each agent has several aspects such as growing and division; then its displacement depends on the interaction among agents and its surroundings.

4.1.1.1 Modification of agent's surrounding environment

To allow agents to increase its size and quantity, it is required to supply some kind of *"fuel"*. The rate of change for this feature consists of a first order differential equation

proposed by [83, 82] and is derived from the bacterial analogy. This expression is given by:

$$-\frac{ds}{dt} = v = \frac{M \cdot V_{max} \cdot s}{K_m + s} \tag{4.1}$$

where s represents the value assigned to the surface in the spatial domain (environment), M is the size of the agent, and v is the rate of change of s. V_{max} and K_m are constants used for tuning the agents' growth rate in the model. Eq. (4.1) assumes that the rate of change in the surrounding environment is proportional to the size of agents (M).

4.1.1.2 Replication of agents.

This process allows converting the resources taken from the environment to create new agents or grow the old ones. The expression used for modeling this process is as follows [82, 84]:

$$\frac{dM}{dt} = \frac{v}{Y_{max}}, \tag{4.2}$$

where Y_{max} represents the maximum efficiency of resource conversion to agent constituents.

4.1.1.3 Preserving the agent *"alive"*

This term allows estimating how much of the resources taken from the environment are used for maintaining the agent running the simulation. It is also derived from the bacterial analogy proposed by [85]. The expression used for modeling the variation due this feature is given by [82]:

$$\frac{dM}{dt} = -M \cdot m_r \cdot Y_{max}, \tag{4.3}$$

where m_r is the maintenance rate, and Y_{max} is the maximum yield, which are used for tuning the model. Adding Eq. (4.2) and Eq. (4.3) give the net growing of each agent as shown in the following expression:

$$\frac{dM}{dt} = \frac{v}{Y_{max}} - M \cdot m_r \cdot Y_{max} \tag{4.4}$$

Therefore, the total effect is given by the equation system defined through Eq. (4.1) and Eq. (4.4).

4.1.1.4 Displacement

The following four key features define the movement of each agent:

1. Avoiding overlap among agents.
2. Local maximum search over the surface in the neighborhood of the agent.
3. Global maximum search over the surface in the space domain.
4. Reacting to the effect of an external disturbance.

The description of each feature is presented below.

Displacement to avoid overlap among agents An important issue that must be considered consists of avoiding -as much as possible- agents to occupy the same physical space in the domain, but it is also required not to separate each one permanently. This movement is useful for arranging the *old-agents* once *new-ones* are born. Thus, for adding this characteristic, it was set a movement proportional to the distance between the pair of agents minus the radius of both agents. The movement is calculated as:

$$\Delta D = k_1 \cdot d_{1-2} - k_2 \cdot (r_1 + r_2) \tag{4.5}$$

where k_1 and k_2 are constants used for setting how fast the movement is, r_1 and r_2 are the radius of the agents, and d_{1-2} is the distance between two agents.

Using this distance, and the equation of the straight line formed between the centers of each agent, the movement of each agent along axes x and y is calculated as:

$$\Delta x = \sqrt{\frac{\Delta D^2}{1 + m^2}} \tag{4.6}$$

$$\Delta y = m \cdot \sqrt{\frac{\Delta D^2}{1 + m^2}} \tag{4.7}$$

The magnitude and the direction of the movement vector for each agent have been previously defined without sign. The sign is included by applying the following Equations: For agent 1:

$$\Delta x_{agent_1} = C_1 \cdot \Delta x \cdot sign\,(\Delta D) \tag{4.8}$$

$$\Delta y_{agent_1} = C_1 \cdot \Delta y \cdot sign\,(\Delta D) \tag{4.9}$$

For agent 2:

$$\Delta x_{agent_2} = C_2 \cdot \Delta x \cdot sign\left(\Delta D\right) \tag{4.10}$$

$$\Delta y_{agent_2} = C_2 \cdot \Delta y \cdot sign\left(\Delta D\right) \tag{4.11}$$

In these equations, m stands for the slope of the straight line, C_1 is a constant that is +1 if agent 1 is on the left of agent 2, and -1 if agent 1 is on the right of agent 2. Moreover, C_2 is opposed to C_1, meaning that if C_1 is +1 then C_2 is -1. Once the movement is defined along the x axis, there are only two possible movements along y, meaning that C_1 and C_2 can be used for defining Δy. There are multiple pairs of agents, then for the same agent is possible to obtain several values for changes in x and y. Therefore, for obtaining a single value in each axis, the average among all the values was used.

Displacement for finding high-substrate concentration at the neighborhood of the agent To allow the agent to modify its environment for growing and replication requires giving the agent the ability to move from its original position to another one. This displacement allows the agent to find places -in the space domain- with better environmental conditions. Two methods give this characteristic: Local maximum search near the agent and for finding the overall maximum in the domain. The first approach consists of treating each agent as a processing unit that interprets some input parameters using predefined rules which result in some behaviour of the unit. Vlachos *et al.* [86] developed the rule-based system used here. This system uses the fuzzy logic theory (Figure 4.3) for interpreting input signals into some outputs through applying pre-established rules. Therefore in this case, there is only one kind of environmental resource, then the input signal is a vector composed by the environmental resource (R_1), the first derivative of the environmental resource, and the energy of the agent under study (ϵ_i). This input vector is given by:

$$Inputs = \left[\begin{array}{cccc} R_1 & \frac{\partial R_1}{\partial x} & \frac{\partial R_1}{\partial y} & \epsilon_i \end{array} \right] \tag{4.12}$$

As output parameters, a vector with three values is obtained:

$$a_i = \left[\begin{array}{ccc} A_1 & A_2 & A_3 \end{array} \right] \tag{4.13}$$

These three values are related to the position and the energy of each agent as:

$$\begin{array}{c} \epsilon_i\left(t+1\right) = \epsilon_i\left(t\right) + \left(2 \cdot A_1 - 1\right) \cdot w_1 \cdot R_1\left(t\right) \\ x_i\left(t+1\right) = x_i\left(t\right) + \left(2 \cdot A_2 - 1\right) \cdot \sigma_x + \rho_x \\ y_i\left(t+1\right) = y_i\left(t\right) + \left(2 \cdot A_3 - 1\right) \cdot \sigma_y + \rho_y \end{array} \tag{4.14}$$

where w_1 is a positive coefficient that determines the maximum amount of R_1 that can be converted into energy at any time. σ_x and σ_y are positive integer coefficients that determine the maximum movement step size in the x and y directions, respectively, while ρ_x and ρ_y are normally distributed random noise sources. Table 4.1 shows the membership functions used in the fuzzy inference system and Figure 4.4 exposes a graphical representation. Table 4.2 presents the rules that connect each input and output variables.

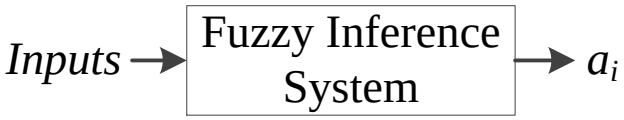

Figure 4.3: Fuzzy Inference System

Table 4.1: Membership functions used in the fuzzy inference system. The representation of L and H is shown in Figure 4.4

Variable	Function	Type	Values
R_1			
$\frac{\partial R_1}{\partial x}$	L	Trapezoidal	$\begin{bmatrix} x: & 0 & 0 & 0.1 & 0.9 \\ y: & 1 & 1 & 1 & 0 \end{bmatrix}$
$\frac{\partial R_1}{\partial y}$	H	Trapezoidal	$\begin{bmatrix} x: & 0.1 & 0.9 & 1 & 1 \\ y: & 0 & 1 & 1 & 1 \end{bmatrix}$
ϵ_i			
A_1	L	Trapezoidal	$\begin{bmatrix} x: & 0 & 0 & 0.2 & 0.9 \\ y: & 1 & 1 & 1 & 0 \end{bmatrix}$
	H	Trapezoidal	$\begin{bmatrix} x: & 0.1 & 0.8 & 1 & 1 \\ y: & 0 & 1 & 1 & 1 \end{bmatrix}$
A_2 A_3	L	Triangular	$\begin{bmatrix} x: & 0 & 0 & 0.6 \\ y: & 1 & 0 & 0 \end{bmatrix}$
	Z	Triangular	$\begin{bmatrix} x: & 0 & 0.5 & 1 \\ y: & 0 & 1 & 0 \end{bmatrix}$
	H	Triangular	$\begin{bmatrix} x: & 0.4 & 1 & 1 \\ y: & 0 & 1 & 1 \end{bmatrix}$

Displacement to find the overall maximum environmental resource In addition to allowing the agent to find higher environmental resources at its surrounding, it was also set that each agent should follow the location of the maximum

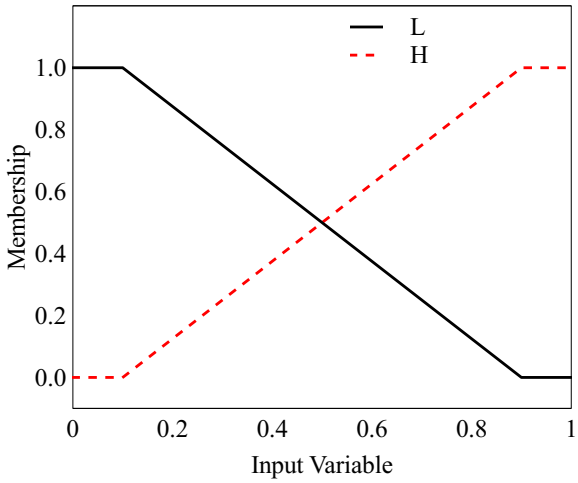

Figure 4.4: Graphical example for membership functions of R_1, $\frac{\partial R_1}{\partial x}$, $\frac{\partial R_1}{\partial y}$, and ϵ_i

Table 4.2: Rules used in the fuzzy inference system

R_1	$\frac{\partial R_1}{\partial x}$	$\frac{\partial R_1}{\partial y}$	ϵ_1	A_1	A_2	A_3
L	L	L	L	L	–	–
H	H	H	H	H	–	–
L	L	L	L	–	Z	Z
L	L	L	H	–	L	L
L	L	H	L	–	Z	Z
L	L	H	H	–	L	H
L	H	L	L	–	Z	Z
L	H	L	H	–	H	L
L	H	H	L	–	Z	Z
L	H	H	H	–	H	H
H	L	L	L	–	Z	Z
H	L	L	H	–	L	L
H	L	H	L	–	Z	Z
H	L	H	H	–	L	H
H	H	L	L	–	Z	Z
H	H	L	H	–	H	L
H	H	H	L	–	Z	Z
H	H	H	H	–	H	H

environmental resources in the domain space. For adding this characteristic, the maximum displacement along the straight line between the center of the agent and the maximum point of the environmental resource, d_{max}, is determined as:

$$d_{max} = k_3 \cdot \sqrt{(x_{max} - x_{agent})^2 + (y_{max} - y_{agent})^2} \tag{4.15}$$

where k_3 is a constant used for tuning how fast the displacement is. The movements along each axes are calculated as:

$$\Delta d_{x_{max}} = \sqrt{\frac{d_{max}^2}{1 + m_{max}^2}} \tag{4.16}$$

$$\Delta d_{y_{max}} = m_{max} \cdot \sqrt{\frac{d_{max}^2}{1 + m_{max}^2}} \tag{4.17}$$

where m_{max} is the slope of the line where the movement takes place. The displacements on each axes are determined as:

$$\Delta x_{max} = C_3 \cdot \Delta d_{x_{max}} \cdot sign\left(d_{max}\right) \tag{4.18}$$

$$\Delta y_{max} = C_3 \cdot \Delta d_{y_{max}} \cdot sign\left(d_{max}\right) \tag{4.19}$$

where C_3 can take the value of $\pm$ 1 depending on the position of the agent respect to the point with the maximum environmental resource.

Displacement due to the effect of an external disturbance An important parameter that must be considered in the model is the wind velocity [87]. This effect is added to the model as an external force that is acting over the agents. It is implemented by assuming that the wind follows a certain pattern. For simplicity, the wind velocity is assumed to behave according to the following mathematical expression:

$$V_{wind} = -\sin\left(k_4 \cdot y\right) - k_5 \cdot x \tag{4.20}$$

where x and y represents the axes of the space domain. It is important to mention this expression can be changed to follow any required pattern. Additionally, it was not used a simple expression to show the flexibility of the proposed model. Then, the displacement of each agent is obtained from the first derivative of this function as:

$$\Delta x = k_6 \cdot \frac{\partial V_{wind}}{\partial x} \tag{4.21}$$

$$\Delta y = k_7 \cdot \frac{\partial V_{wind}}{\partial y} \tag{4.22}$$

where k_4, k_5, k_6, and k_7 are constants used for tuning the model. The vector field created by this wind pattern is shown in Figure 4.5.

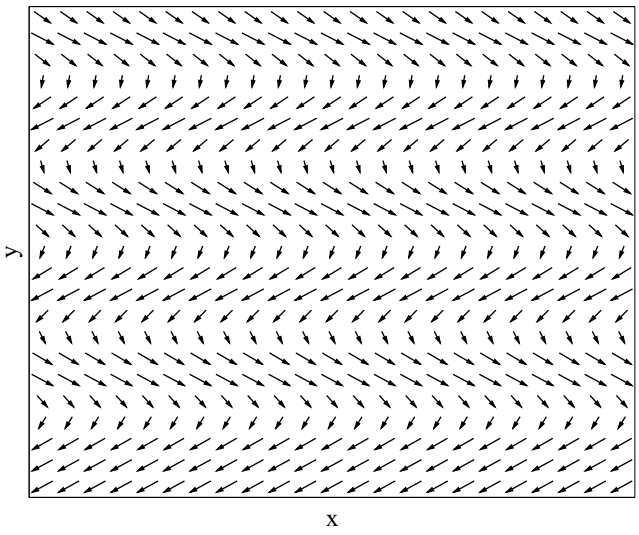

Figure 4.5: Vector field of the external disturbance created by the wind pattern in Eq. (4.20).

Each agent has a displacement respect to the other agents and the environmental resource. It means that there are several displacements along x and y for each one. Therefore, for each agent, all these movements are added, and a single movement along x and y takes place.

4.1.2 Additional subjects about the model

Some aspects are important to mention to give a better idea about the way the model works. A brief description of these items is presented below.

4.1.2.1 Initial distribution of the environmental resource

Given that the agents follow the maximum environmental resource, it is important then to set some environmental resource gradient. In this research, the environmental resource distribution proposed by [88] is used. The expression of this distribution is given by:

$$S = e^{-\frac{(x-x_{center})^2+(y-y_{center})^2}{k_8}} \tag{4.23}$$

where x_{center} and y_{center} are the coordinates where the maximum concentration is located, and k_8 is a constant to adjust the magnitude of the substrate gradient.

4.1.2.2 Agent shape

Agents can take many forms, however in this study is assumed that each agent has a circular shape. A bell shape function was used rather than a circumference expression. A two-dimensional representation of this bell function is a circumference that is not homogeneous inside. This feature allows having cloud shadows with different covering tones. The following expression is used to simulate the agent shape:

$$Agent = e^{-\frac{(x-x_{agent})^2+(y-y_{agent})^2}{\sigma_{agent}}} \tag{4.24}$$

where σ_{agent} is used for determining the size of the agent. Hence, this size is related to the growth of the agent by:

$$\sigma_{agent} = k_9 \cdot r_{agent} \tag{4.25}$$

$$r_{agent} = \sqrt[3]{\frac{3}{4 \cdot \pi} \cdot V_{agent}} \tag{4.26}$$

$$V_{agent} = \frac{M}{\rho_{agent}} \tag{4.27}$$

4.1.2.3 Reproduction and death of the agents

Once an agent modifies its surroundings, immediately start to grow. However, it does not keep growing unrestrictedly, once it reaches a predefined limit value, then the agent is divided. This division process consists of creating a new agent with an initial volume (V_u), then the initial agent reduces its size until it has a volume equal to the volume before division (V) minus the volume of the new agent (V_u). Now the death process of the agents is relatively straightforward. A timer in installed on each agent and is used to register its age. Then, after the timer reaches a predefined value, the agent is deactivated. It is worth mentioning that not all the agents are born at the same time, then they all do not suddenly disappear.

4.1.2.4 Coding features

It is important to be aware of some issues can arise during the implementation of the proposed model. Firstly, there is a considerable amount of agents so that it is not suitable to run a routine for each one of them. The code was developed by using $2D$ or $3D$ arrays rather than for-loops. Therefore, taking advantage of the matrix

operations and some functions of Matlab, it was possible to create a routine with a single for-loop used for each time step.

4.2 Preliminary Results

Initially, the results are focused on the versatility of the proposed model. Two configurations are proposed (Figure 4.6):
Configuration 1:

$$S = e^{-\frac{(x+2.8)^2+(y+2.5)^2}{k_8}} \tag{4.28}$$

Configuration 2:

$$S = e^{-\frac{x^2+(y+2.5)^2}{k_8}} + e^{-\frac{(x+2.8)^2+(y-2.5)^2}{k_8}} \tag{4.29}$$

Table 4.3: Set of parameters used for showing versatility of the model

Parameter	Config. 1	Config. 2
V_{max}	0.0180	0.0270
K_m	0.07	0.07
Y_{max}	0.4	0.4
m_r	6×10^{-4}	6×10^{-4}
V_u	6.897×10^{-4}	6.897×10^{-4}
V_d	2.3×10^{-3}	2.3×10^{-3}
σ_x	0.1	0.1
σ_y	0.1	0.1
ρ_x	$[-0.05 \ \ +0.05]$	$[-0.05 \ \ +0.05]$
ρ_y	$[-0.05 \ \ +0.05]$	$[-0.05 \ \ +0.05]$
w_1	0.1	0.1
k_1	4.8	4.8
k_2	33.6	33.6
k_3	0.06	0.1
k_4	2	2
k_5	1	1
k_6	1.5	1.5
k_7	1.5	1.5
k_8	50	10
k_9	0.43	0.43
Initial Subs. Distr.	Eq. (4.28)	Eq. (4.29)
Initial agent $x-y$ position	Random	Random

Table 4.3 shows the parameters used for obtaining two different responses from the proposed biomimetic model. It is worth mentioning that some of this values

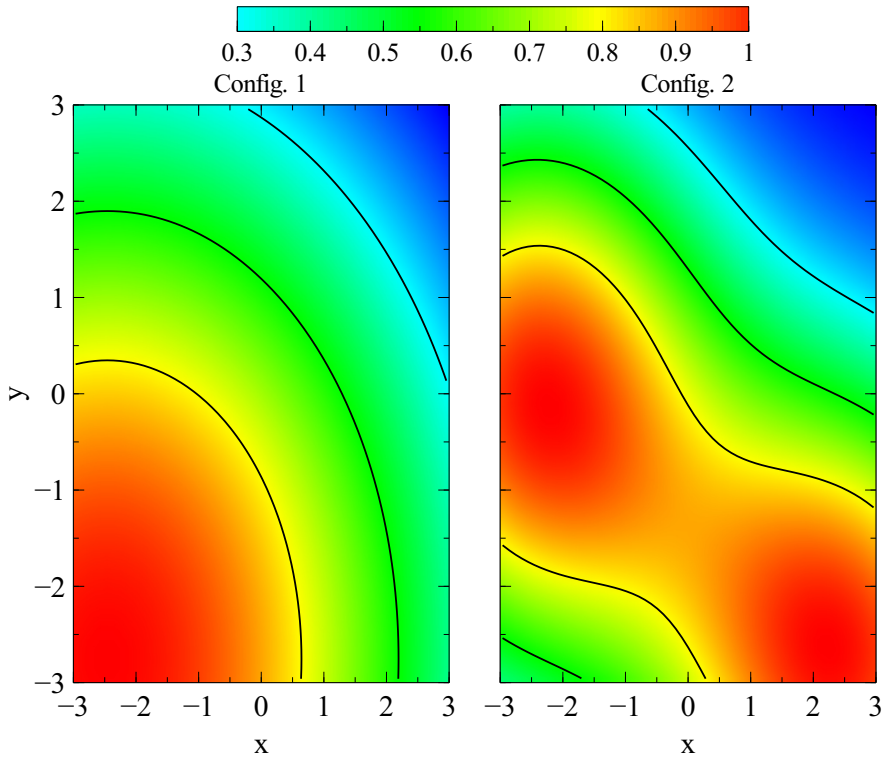

Figure 4.6: Substrate distribution used for Configurations 1 and 2.

were taken from the references mentioned in this paper, and other values were set while constructing the model and therefore, the proposed model is not constrained to work using those values. The idea behind this comparison is to show the potential and flexibility of the model. Other investigations can be focused on optimizing these parameters according to their requirements.

Figure 4.7 & 4.8 show how sensitive is the proposed model for the input parameters so that changing a few of them lead to completely different responses. It shows that the proposed model can adapt and emulate different situations and scenarios.

4.3 Evaluation of Results

Once the model is implemented, it is important to validate the results obtained with the real phenomenon data. The comparison between data sets is accomplished in two parts. The first one consists of a qualitative comparison among real images (Figure 4.9a), clouds using the fractal method developed by [77] (Figure 4.9b), and the proposed biomimetic model (Figure 4.9c). Real images are data published by the National Renewable Energy Laboratory (NREL), which were taken on August 05, 2014 and reported by [89].

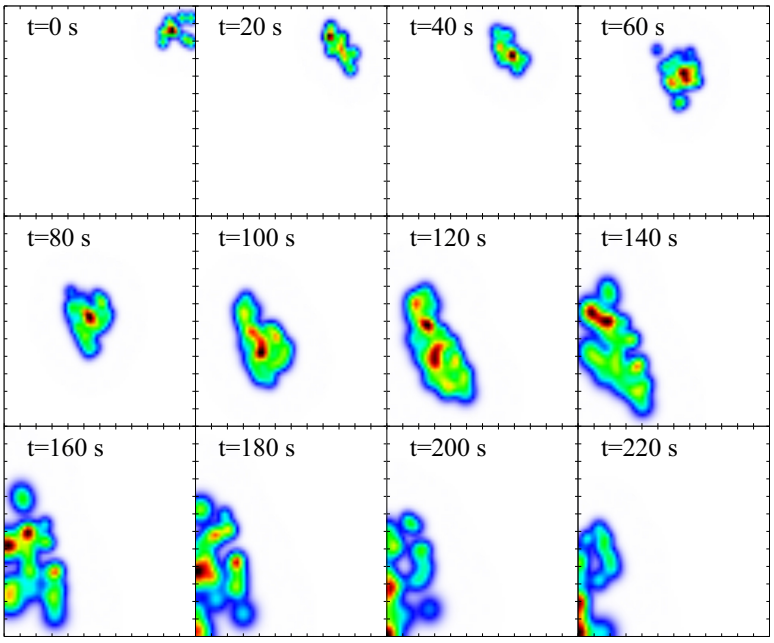

Figure 4.7: Response obtained using parameters of configuration 1

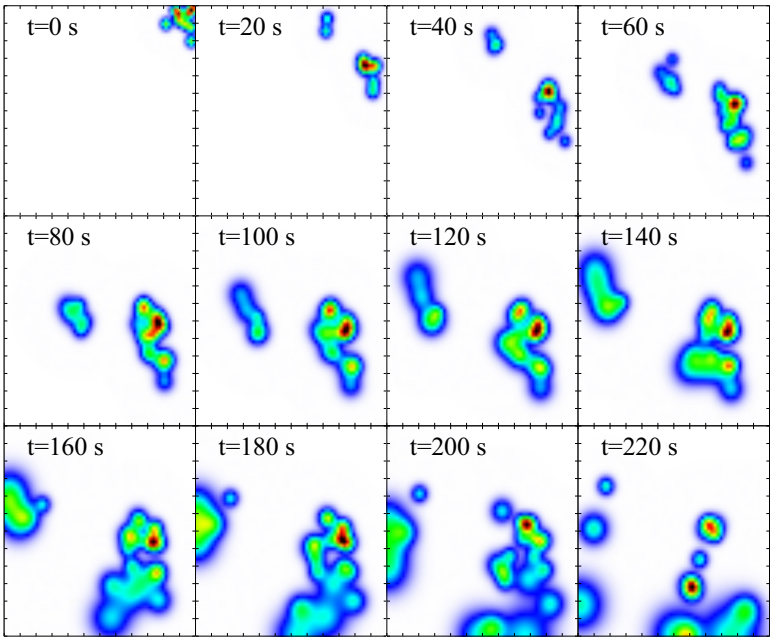

Figure 4.8: Response obtained using parameters of configuration 2

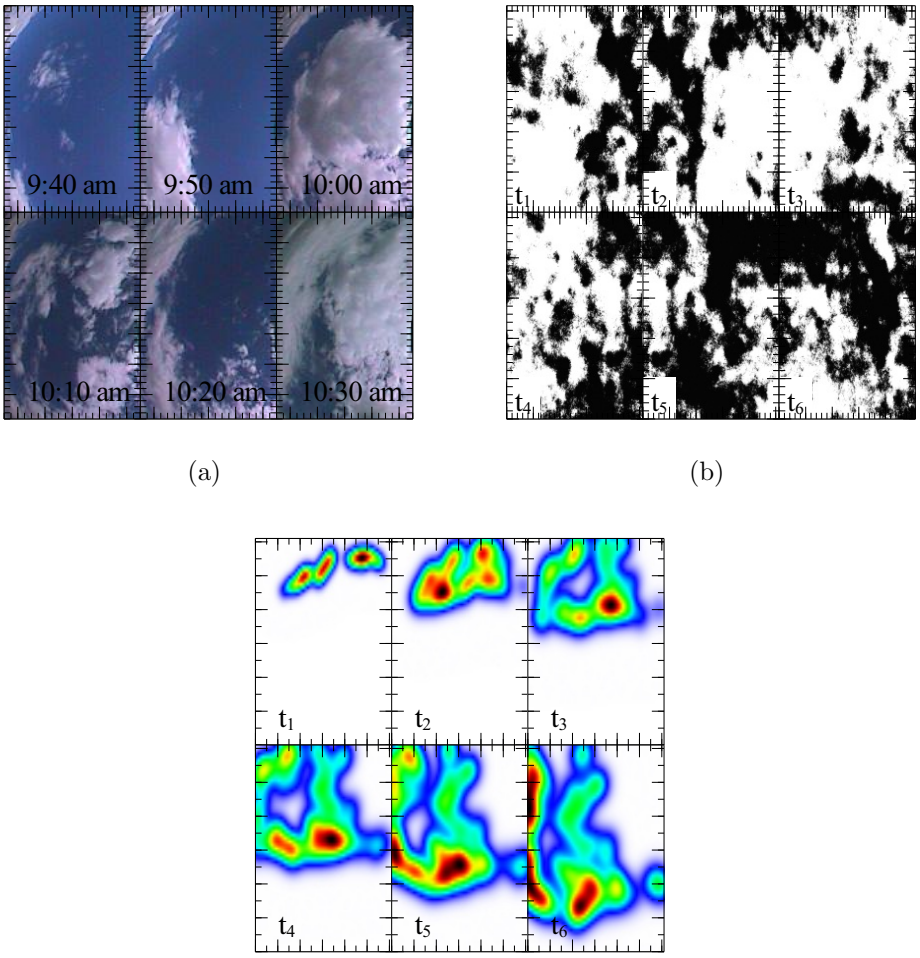

(a) (b)

(c)

Figure 4.9: Comparison between real cloud patterns, and patterns created by the fractal model and the proposed model. (a) Real images of clouds for a time series every 10 minutes obtained from [89]. (b) Fractal methodology proposed by [77]. (c) Proposed biomimetic model

As shown in Figure 4.9a, real clouds behavior is a very complex phenomenon, whose shapes are continuously varying. Therefore, the cloud shadows have also complex behavior over time as well. These images also show that it is possible to have sudden changes of the cloud shadows in a small period and the light passing through the clouds can vary even though they have the same shape. It is an important feature that our model can replicate, especially for solar applications. The fractal surface model showed similar cloud patterns to those presented by the real clouds (Black regions in Figure 4.9b). However, the simulations revealed that this model lacks a proper transient behavior since only shows a static image that moves over a fixed frame, which is an assumption that may not be suitable to simulate some clouds. The proposed model showed shadows whose shapes are continuously changing and moving, a behavior that is closer to the dynamic seen in the real phenomenon. Besides, different cloud's attenuations of direct solar radiation can be obtained by optimizing the parameters previously described to follow the responses shown in real direct radiation curves. Due to its simplicity, this approach allows having a flexible model which can follow some desired characteristics. For example, two different sets of clouds shadows can be overlapped to create a more complex shadow pattern.

The second approach, quantitative comparison, is accomplished by analyzing the Fourier Descriptors (FD) of the images. The Fast Fourier Transform (FFT) is an analysis employed to convert a signal to the frequency domain. The discrete form of this transform is expressed as follows [90].

$$F(p,q) = \sum_{m=0}^{M-1} \sum_{n=0}^{N-1} f(m,n)\, e^{-\frac{2\pi mp}{M} i} e^{-\frac{2\pi nq}{N} i} \tag{4.30}$$

where $p = 0,\ 1, \cdots,\ M-1$; $q = 0,\ 1, \cdots,\ N-1$. N and M are the dimensions of the image.

A direct application of the $2D$ FFT in any image is an option. However, it is not practical due the captured features are not rotation invariant. For this reason, the approach developed by [91] is used. This procedure uses the Polar Fourier Transform, and a variation of the Zernike Moment Descriptors (VZM) for obtaining the normalized Generic Fourier Descriptors (GFD) [91]. A Matlab code for getting the GFDs is available in the MathWorks official web page by [92]. In consequence, for analyzing the differences among cloud shapes, the procedure proposed includes four stages. These steps are described below.

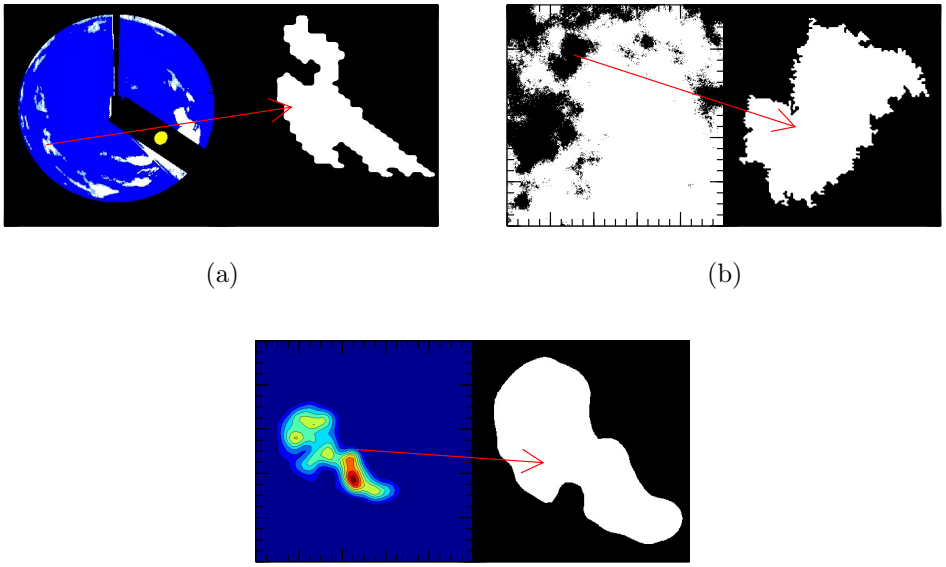

(a) (b)

(c)

Figure 4.10: Silhouette extraction from cloud pictures for shape analysis. (a) Processed real image of clouds from [89]. (b) Image from fractal methodology proposed by [77]. (c) Image from proposed biomimetic model.

4.3.1 Stage 1: Image conditioning

For the FFT analysis, it is required to have binary images with a single object centered at its centroid. In consequence, the silhouette of each cloud from the pictures must be extracted. Figures 4.10a, 4.10b, and 4.10c show examples of image conditioning for real photographs, for the fractal model, and for the biomimetic model respectively. As it respects to the size of the images, each one is fixed to have a width and a height of 300 pixels. Provided all the images are set to the same reference, then the shape of the cloud is the main source of variation.

4.3.2 Stage 2: Obtaining the GFDs

At this point, the Generic Fourier Descriptors are obtained using m and n radial and angular divisions. For this study m and n are 30 and 100 respectively and a total of 3101 Fourier Descriptors are obtained ($m \times n + n + 1$). Figures 4.11 shows that the number of proposed Fourier Descriptors are enough to take into account even minimal values.

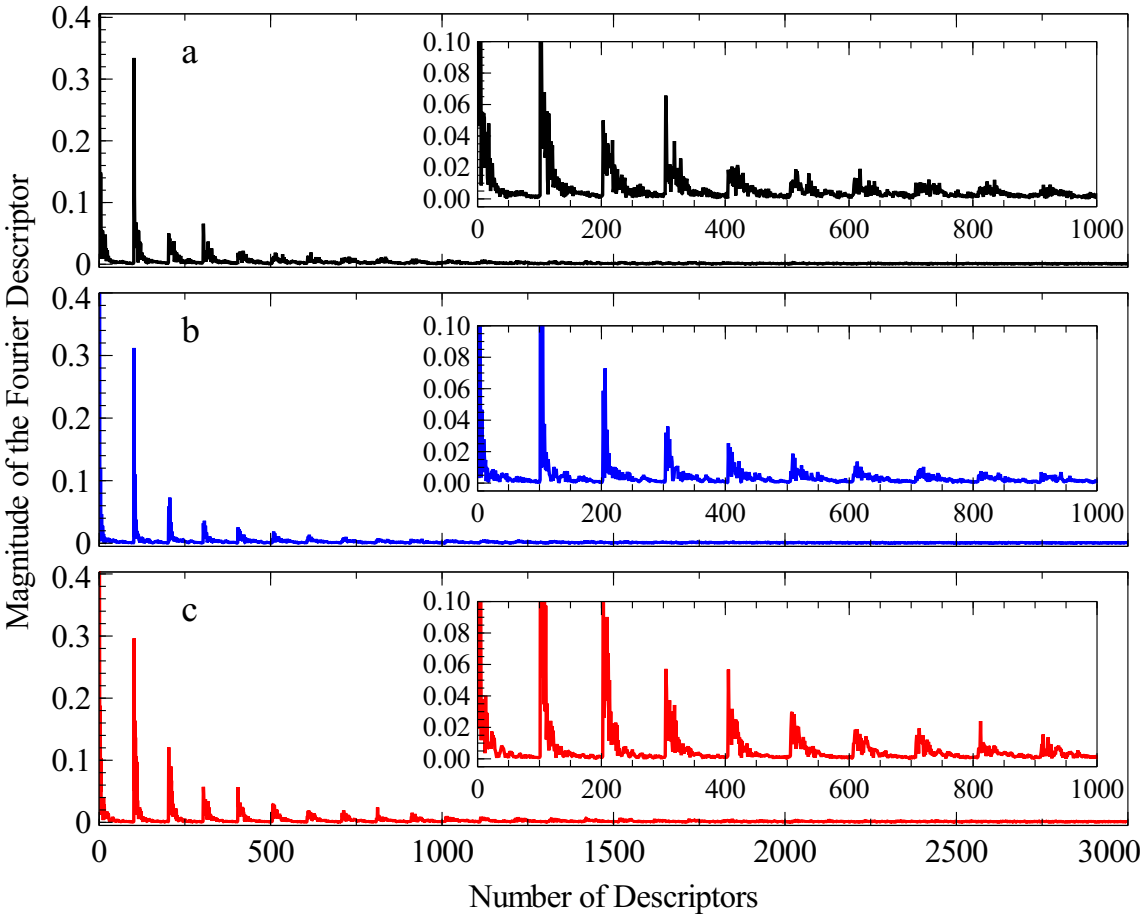

Figure 4.11: Generic Fourier Descriptors for (a) Real image of cloud from [89]. (b) Image from fractal methodology proposed by [77]. (c) Image from proposed biomimetic model.

4.3.3 Stage 3: Overall response variable

As stated by [91], the similarity of two images represented by two sets of Fourier Descriptors can be measured through the Euclidean distance (a scalar value) between the two vectors. However, the difference between pairs of images is not directly measured. Instead, each image is compared with a reference image. In this case, the standard image is a circle of the same size as the conditioned images. This approach allows measuring and comparing the general performance among the groups of images through a single value.

4.3.4 Stage 4: Statistical analysis

Once the images are prepared, and the response variable is defined, an Analysis Of Variance (ANOVA) is executed. For this analysis, images were divided into four groups: two sets of real images, one group for fractal images, and another group for biomimetic images. For guaranteeing a statistical power of 0.9, each group has a sample of 50 images. Therefore a total of 200 images were analyzed. Parameters used for the biomimetic model are shown in Table 4.4. These values were obtained using an optimization procedure carried out by manipulating some of its tuning inputs. The primary goal of this optimization consists of getting a behavior near the patterns seen in the real phenomenon. Figure 4.12 shows the results for the Least Significance Difference (LSD). The analysis reveals that there is no statistical difference between the real images groups, as expected. With regards to the proposed model, the statistical analysis shows there that is no statistical difference between the actual pictures and the proposed model. However, there is a significant difference between the fractal model and real images/the proposed model. The results demonstrated that the biomimetic model is flexible enough to be tuned for closely matching the actual responses.

4.4 Solar Radiation Transient

Solar radiation is a renewable energy source that inevitably changes as the earth moves around the sun and its axis, and due to atmospheric conditions. It causes quick DNI changes in very short periods. Nevertheless, there is not a clear agreement about what “short” means. According to Tomson [93] an intuitive “short interval” should be around 1 min, considering hourly or daily basis solar radiation measurements. However, as also proposed by Tomson [93], the transient behavior in solar radiation

Table 4.4: Set of parameters used for obtaining the images for the quantitative evaluation

Parameter	Value	Parameter	Value
V_{max}	0.0165	k_1	2.5451
K_m	0.1606	k_2	12.5773
Y_{max}	0.8235	k_3	0.0047
m_r	3.9719×10^{-4}	k_4	2
V_u	0.5778	k_5	1
V_d	0.0039	k_6	0.2515
σ_x	0.1184	k_7	0.6430
σ_y	0.1493	k_8	50
ρ_x	$[-0.05 \ \ +0.05]$	k_9	0.43
ρ_y	$[-0.05 \ \ +0.05]$	Initial Distr.	Eq. (4.28)
w_1	0.0320	Initial agent $x-y$ position	Random

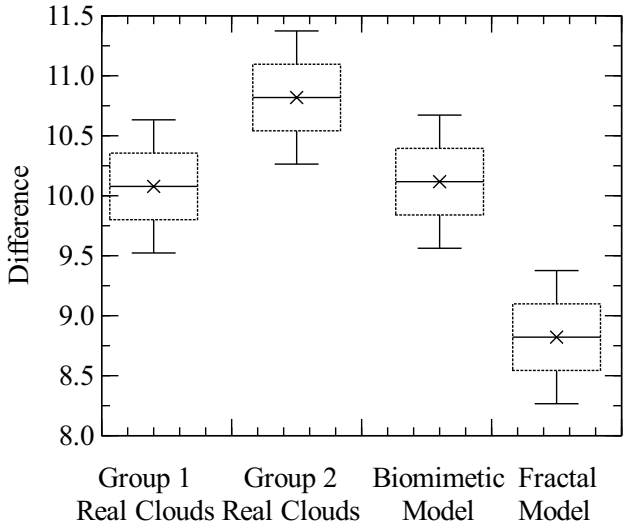

Figure 4.12: Graphical LSD results among the studied groups.

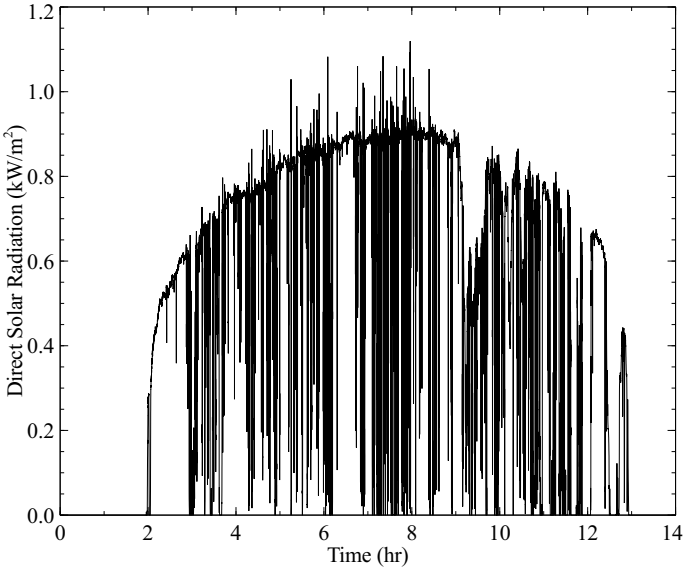

Figure 4.13: Sample curve of direct solar radiation for April 01, 2010. Oahu Solar Measurement Grid (NREL), UTC-10 [94]

.

processes is captured by having a sampling period under 5 seconds. Figure (4.13), using data from Sengupta and Andreas [94], presents a typical direct solar radiation curve under atmospheric disturbances. This figure shows how solar radiation abruptly decreases during some periods, and then it quickly increases again. These sudden changes indicate clouds are passing over the measuring station and blocking the direct solar radiation. The procedure implemented in this research proposes to tune the previous cloud shading model to create DNI transients for a 2D region. The expected results can be used to analyze the dynamic performance of a solar system under radiation disturbances in a short period. Since the model is addressed to produce transient disturbances during short time periods, small sections of 10 min. from the actual measurements are taken for developing the tuning procedure. Figure (4.14) shows a small period of data from Fig. (4.13). It is worth mentioning that this curve is only one sample of data used during the optimization process. Following sections show a better description of this procedure.

4.5 Optimization Procedure

The next step consists of adjusting tuning parameters to obtain transient responses like those seen in direct solar radiation measurements. For tuning and validation of the results achieved through the model, it would be ideal to have DNI measurements time

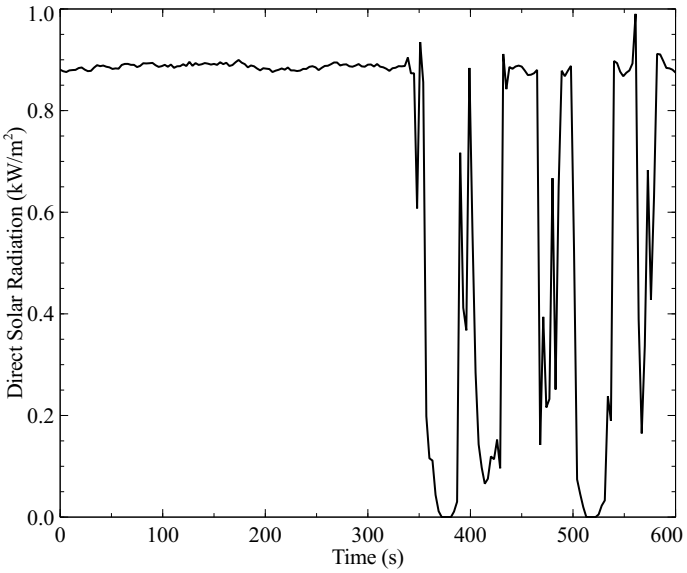

Figure 4.14: Reduced curve of direct solar radiation for April 01, 2010 from 12:00 to 12:10. Data taken from Ref. [94]

series at several points on a grid. However, this kind of data is not commonly available. That is the main reason to carry out the procedure proposed in this research. The developed model gives a series of images over time, which means that each location (pixel) in those images represents a model time series of direct solar radiation similar to the curve shown in Fig. (4.14). The philosophy behind this procedure consists of finding a set of parameters that allows having responses as close as possible to those found in measured data. However, the most important issue is not to reproduce each curve, but to tune the model, so that DNI transients follow the tendency seen in the actual data.

Using this procedure also implies that only some locations in the image will have the same values as the measured data while other sites will follow the same trend without matching it. The fitting between modeled time series and measurements is performed using a statistical index between them. Afterward, those matches with the highest index are selected. This statistical index involves using three parameters: the mean square error (MSE) coefficient (r^2), the variance ratio between both curves (VR), and a weighting parameter obtained from the Hotelling T^2 statistic. A brief definition to each one of these parameters is presented below.

4.5.1 Mean Square Error correlation coefficient (r^2)

Let n_p be the number of positions (pixels) in the images obtained from the model and let n_c be the number of real radiation curves, corresponding to the number of days in

the data set. In this case April, July, September, and December of 2010 from 12:00 to 12:10 [94]. The r^2 coefficient indicates the fitting degree between two data sets [95]. For each one of the model time series, and each measurement the mean-square error correlation coefficient is calculated as:

$$r^2 = 1 - \frac{\sum_{i=1}^{i=n} (y_i - f_i)^2}{\sum_{i=1}^{i=n} (y_i - \overline{y})^2}, \tag{4.31}$$

where f_i represents the model time series and y_i are the measurements. It is worth point out that images using the model have 61×61 pixels (n_p). Hence, there are 3721 curves (n_c), and for every single location, there will be n_c values of r^2 stored in vector R_i.

4.5.2 Variance Ratio

This parameter takes into account the presence of a similar disturbance rather than the interval of time where it takes place. The variance ratio, VR, is calculated as:

$$\mathrm{VR} = \frac{1}{\left|1 - \frac{\sigma^2_{Pixel\ Curve}}{\sigma^2_{Actual\ Curve}}\right| \cdot \left(\left|1 - \frac{\sigma^2_{Pixel\ Curve}}{\sigma^2_{Actual\ Curve}}\right|\right)_{max}} \tag{4.32}$$

A variance ratio value close to 1 means both variances are similar and near to *zero* means they diverge. For each location i, values of VR_i are stored in a diagonal matrix.

4.5.3 Hotelling T^2 statistic

Using the T^2 statistic is convenient because it allows sorting measurements from those that are a standard representation of the phenomena to those considered as outliers. This statistic is commonly calculated by the Principal Component Analysis (PCA) method. PCA also allows studying data where observations describe several inter-correlated quantitative variables. Thus, it is possible to obtain a lower dimensional representation that preserves the correlation structure between process variables. Getting this statistic involves autoscaling of training data, get the spectral decomposition of the covariance matrix, obtain the reduced statistical model, and determine the T^2 statistic.

Autoscaling is required to avoid an inappropriate dominance of particular variables in the dimension reduction procedure. Thus, let $X \in \mathbb{R}^{n \times m}$ a matrix representation of m variables with n observations in time, represented as:

$$X = \begin{bmatrix} x_{11} & x_{12} & \cdots & x_{1m} \\ x_{21} & x_{22} & \cdots & x_{2m} \\ \vdots & \vdots & \ddots & \vdots \\ x_{n1} & x_{n2} & \cdots & x_{nm} \end{bmatrix} \tag{4.33}$$

The autoscaling for this matrix can be obtained as:

$$X_{as} = (X - I_n \cdot b_m) \cdot J \ , \tag{4.34}$$

where I_n is a column vector of size n filled with *ones*, b_m is a row vector that contains the mean value of each column of the matrix X, and J is a diagonal square matrix of m elements where each one represents the inverse of the standard deviation for each column of matrix X. Then, it is required to extract the information from each set of data. This extraction is done using the spectral decomposition of the covariance matrix, which indicates the cross correlation among the m variables of the matrix X [96, 97]. The covariance matrix, S_m is calculated as:

$$Sm = \frac{1}{n-1} X^T \cdot X \tag{4.35}$$

and the spectral decomposition is determined by:

$$Sm = V \cdot \Lambda \cdot V^T \ , \tag{4.36}$$

where Λ is a diagonal matrix that contains the eigenvalues of S (Sorted from the highest to the lowest), and V is an orthogonal matrix that has in each column the eigenvector corresponding to the eigenvalue in Λ.

The reduced statistical model can be obtained from different methodologies [98, 99, 100]. The method used is the percentage variance test. This method selects the required variables to explain a variance percentage arbitrarily fixed, for this case a value of $\sigma_{PCA} \geq 0.95$ was selected. The explained variance is calculated by:

$$\sigma_{PCA} = \frac{\sum_{i=1}^{i=a} \Lambda_{i,i}}{\sum_{i=1}^{i=m} \Lambda_{i,i}} \ , \tag{4.37}$$

where a indicates the number of variables used for representing properly the original data set [101, 102, 103, 104]. The reduced model can be written as:

$$Sm_R = V_R \cdot \Lambda_R^{-2} \cdot V_R^T \tag{4.38}$$

V_R represents the eigenvector matrix with the first a columns of the original matrix, and similarly, Λ_R represents a diagonal matrix with the a first eigenvalues of the original obtained. The T^2 statistic characterises the variability of an m-dimensional space using a scalar. This scalar is obtained by:

$$T^2 = x_{Day} \cdot Sm_R \cdot x_{Day}^T \, , \tag{4.39}$$

where x_{Day} is a row vector that, in this case, contains the radiation curve for a particular day. Therefore, applying this equation to all the measurement curves, a set of T^2 is obtained. The higher the value of this statistic, the more different this measurement time series is among the other curves. For this optimization procedure, a new statistic W_{T^2} is introduced:

$$W_{T^2} = 1 - \frac{T^2}{(T^2)_{max}} \tag{4.40}$$

The new variable W_{T^2} takes values close to *zero* for high values of T^2 and close to *one* for low values of T^2. Values for W_{T^2} are stored in a diagonal matrix, W.

4.5.4 Performance Parameter

Let P_i be called the performance parameter for location i, which is defined by:

$$P_i = R_i^T V_{R_i} W = \begin{bmatrix} r_{i,1}^2 VR_{i,1} W_{T^2}^1 \\ r_{i,2}^2 VR_{i,2} W_{T^2}^2 \\ \vdots \\ r_{i,n_c}^2 VR_{i,n_c} W_{T^2}^{n_c} \end{bmatrix} \tag{4.41}$$

For every location i there will be a P_i vector. Let P_i^{max} be the largest element of vector P_i whose location is given by k_i^{max}. For all the locations, the values of P_i^{max} and k_i^{max} are stored in P^{max} and K^{max}, respectively. The overall performance parameter, P^{max}, and its locations' vector, K^{max}, are defined as:

$$P^{max} = \begin{bmatrix} P_1^{max} & P_2^{max} & \cdots & Pn_c^{max} \end{bmatrix}^T \tag{4.42}$$

$$K^{max} = \begin{bmatrix} k_1^{max} & k_2^{max} & \cdots & kn_c^{max} \end{bmatrix}^T \tag{4.43}$$

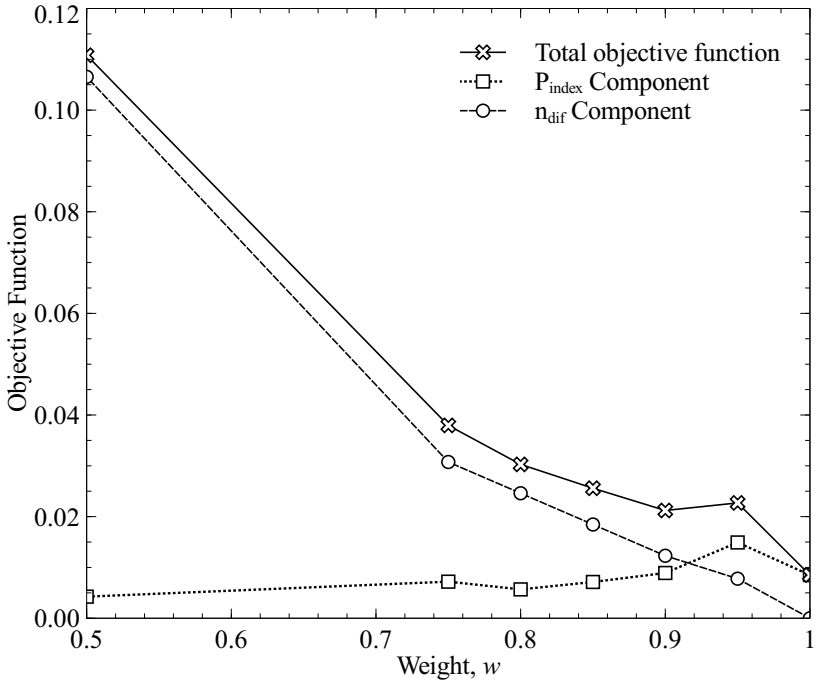

Figure 4.15: Variation of both components of the objective function

These two vectors will be used to define the objective function.

4.5.5 Objective Function

It is required to set an objective function to measure the performance of the entire model. In this project, two parameters P^{max} and K^{max} are proposed. It is desired to take into account the diversity of curves chosen during the performance of each parameter calculation. Hence, the objective function value is expected to be higher if a larger set of measurement time series is used. For this purpose, vector K^{max} is transformed into K^{max}_{red} using the standard MATLAB function *unique*, which returns a vector with no element repeated and, then, with a lower dimension $n_{red} < n_c$. The proposed objective function is given by:

$$f = w \left[\frac{1}{n_p} \left(P^{max} \right)^T I_{n_p} \right] + (1 - w) \frac{n_{red}}{n_c} , \tag{4.44}$$

where I_{n_p} is a column vector containing n_p ones and w is a weighting factor that considers the magnitude order of each component to avoid an overlapping of the larger component over the smaller one. The expression $(1/n_p) \left(P^{max} \right)^T I_{n_p}$ is the mean of vector P^{max}.

Once the objective function has been defined, with the optimization algorithm (standard MATLAB *fmincon* in this case), it is possible to find a set of tuning

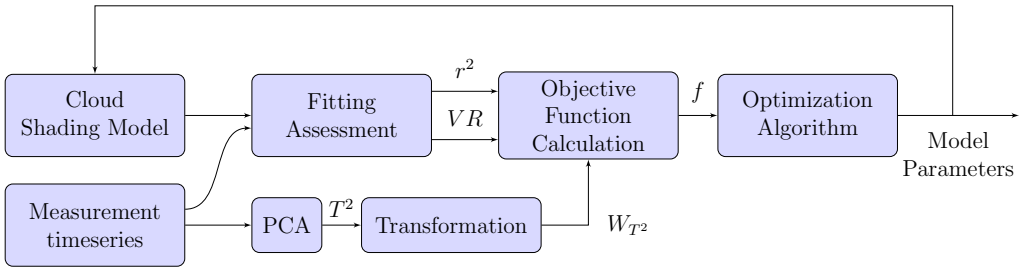

Figure 4.16: Optimization procedure flowchart

Table 4.5: Initial agent distribution for configuration 1 and 2.

Agent	Config. 1		Config. 2	
	x	y	x	y
1	2.727	2.886	2.914	2.433
2	2.723	2.565	2.027	2.917
3	2.274	2.156	2.801	2.499
4	2.250	2.370	2.910	2.914
5	2.648	2.180	2.457	2.748
6	2.046	2.927	2.838	2.827
7	2.048	2.020	2.995	2.967
8	2.400	2.280	2.454	2.124
9	2.283	2.033	2.369	2.942
10	2.103	2.652	2.607	2.532

parameters in the model which maximize this function. It means that the model output is performing as close as possible to real measurements. This optimization procedure was carried out using different values for the weighting factor w. The input model parameters and functions used for this procedure are shown in Table 4.3 and 4.5. The results showed (Figure (4.15)) that a w value close to 0.9 should be used to have a similar order of magnitude for both components of the objective function. Figure (4.16) presents a flowchart summarizing the optimization procedure.

4.5.6 Procedure followed

This process initiates with an optimization method to set the tuning parameters of the model. It is worth mentioning that, in the proposed model, three input functions are qualitative and kept unchanged during each simulation. These three inputs functions are the environmental resource (*"food"*) consumption law used for the agents, the initial environmental resource distribution, and the wind pattern used.

Hence, it is important to study the impact of these three functions on the model's performance. For studying their effect, a 2^3 factorial design is proposed, which means

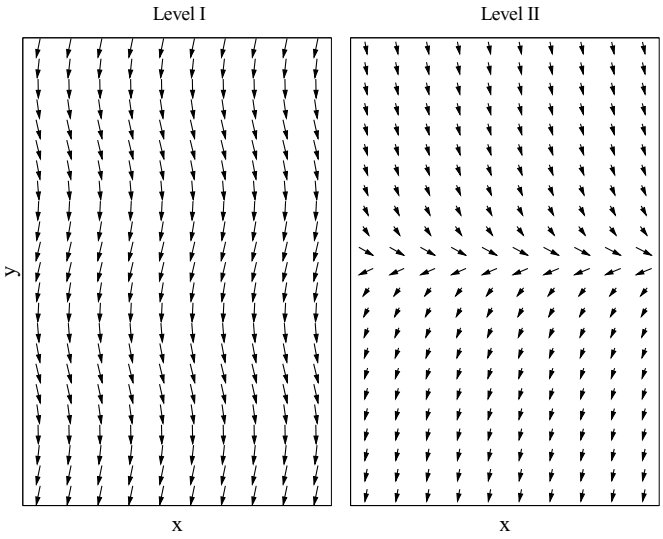

Figure 4.17: Wind vector field used for Level I and II in the factorial design

the qualitative variable has two levels (Table 4.6), for a total of eight simulating conditions. It is important to clarify that there are infinite possibilities to define these functions according to the specific requirements and experimental conditions. For each simulating conditions, the optimization procedure previously described is carried out for obtaining solar radiation transients similar to those found in real measurements. These different states allow having several shapes of cloud shadows, and as a consequence different spatial distributions of the solar radiation are obtained. Figure (4.6) and (4.17) show the distribution assumed for the environmental resource and wind pattern, respectively. The assumed wind patterns are not intended to reproduce any particular behavior. Hence basic functions have been used for simplicity.

Table 4.6: Levels used for qualitative variables

	Environmental Resource Consumption Law
Level I	$-\frac{ds}{dt} = v = \frac{M \cdot V_{max} \cdot s}{K_m + s}$
Level II	$-\frac{ds}{dt} = v = V_{max} \cdot \left(1 - k_{11} \cdot e^{-\frac{S}{K_m}}\right)$
	Environmental Resource Distribution
Level I	$S = e^{-\frac{(x+2.8)^2+(y+2.5)^2}{50}}$
Level II	$S = e^{-\frac{x^2+(y+2.5)^2}{10}} + e^{-\frac{(x+2.8)^2+(y-2.5)^2}{10}}$
	Wind Pattern
Level I	$V_{wind} = -\sin(2 \cdot y) - x$
Level II	$V_{wind} = -0.1 \cdot x + \sqrt{\lvert 0.1 \cdot x \cdot y + y \rvert}$

Table 4.7: Objective function values after optimization of each condition

N	Environmental Resource Consumption Law	Environmental Resource Distribution	Wind Pattern	f
1	I	I	I	0.0210
2	I	I	II	0.0262
3	I	II	I	0.0288
4	I	II	II	0.0330
5	II	I	I	0.0249
6	II	I	II	0.0168
7	II	II	I	0.0361
8	II	II	II	0.0260

4.6 Results

After running the optimization procedure described in previous sections, Figure (4.18) and (4.19) show a comparison between solar radiation measurements and curves obtained from the proposed model. Each figure shows two sets of curves (the proposed model and real measurements) for each condition described in Table 4.7. As seen in these graphs, there is an appropriate matching between both curves for almost all cases, which indicates that the optimization procedure works suitably according to its design. In some cases, Fig. (4.19) (condition 6, July 5-2010), some further disturbances take place, which for the objective of this research is admissible. This kind of transient behaviors is useful to carry out a test of any control strategy in a solar thermal plant. On the other hand, the results also showed that the direct solar radiation rate of change obtained by the model fits well the values given by real measurements, which is an important characteristic for carrying out subsequent dynamic studies or for testing control strategies.

Values of the objective function after the optimization procedure are shown in Table 4.7. Although the objective function slightly varies, the analysis of variance (ANOVA) indicates that the qualitative variables do not have a statistically significant effect, which means that the proposed optimization procedure can tune the model regardless initial conditions.

Figure (4.20) shows a spatial distribution of solar radiation. Four snapshots are presented based on the behavior exhibited by condition 4. As seen in Fig. (4.20), solar radiation is not homogeneously distributed and has a dynamic behavior, which means that its spatial effect on any solar model or study is different as compared to the effect given by previous models found in the literature.

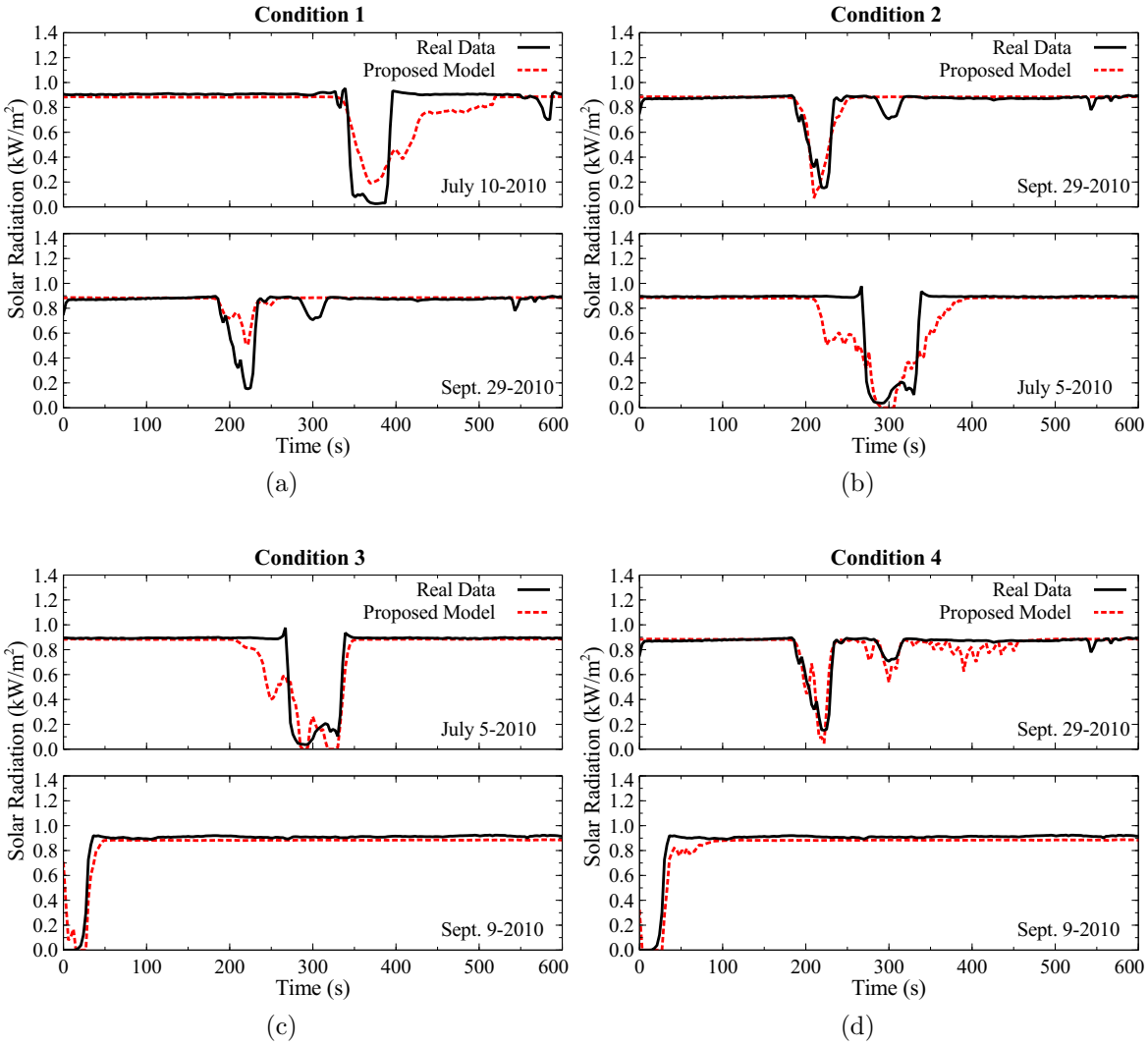

Figure 4.18: Comparison between real measurements and model results for each one of the eight experimental conditions

The variability of the results obtained by the proposed model is also characterized using an *arrow head* plot. This kind of graph shows the clear sky index (K_T) as a function of the variability index (VI) [105, 106]. This plot allows distinguishing variability in a large amount of solar radiation time series. Since the model used creates solar disturbances along time over a 2D region, then each spatial location represents a DNI time series. Figure (4.21) shows the *arrow head* plot for the results obtained using the proposed model also for condition 4. These results confirm the high variability that this model is pursuing, which is evident because it shows clear sky indexes larger than 0.6 and also variability indexes larger than 10.

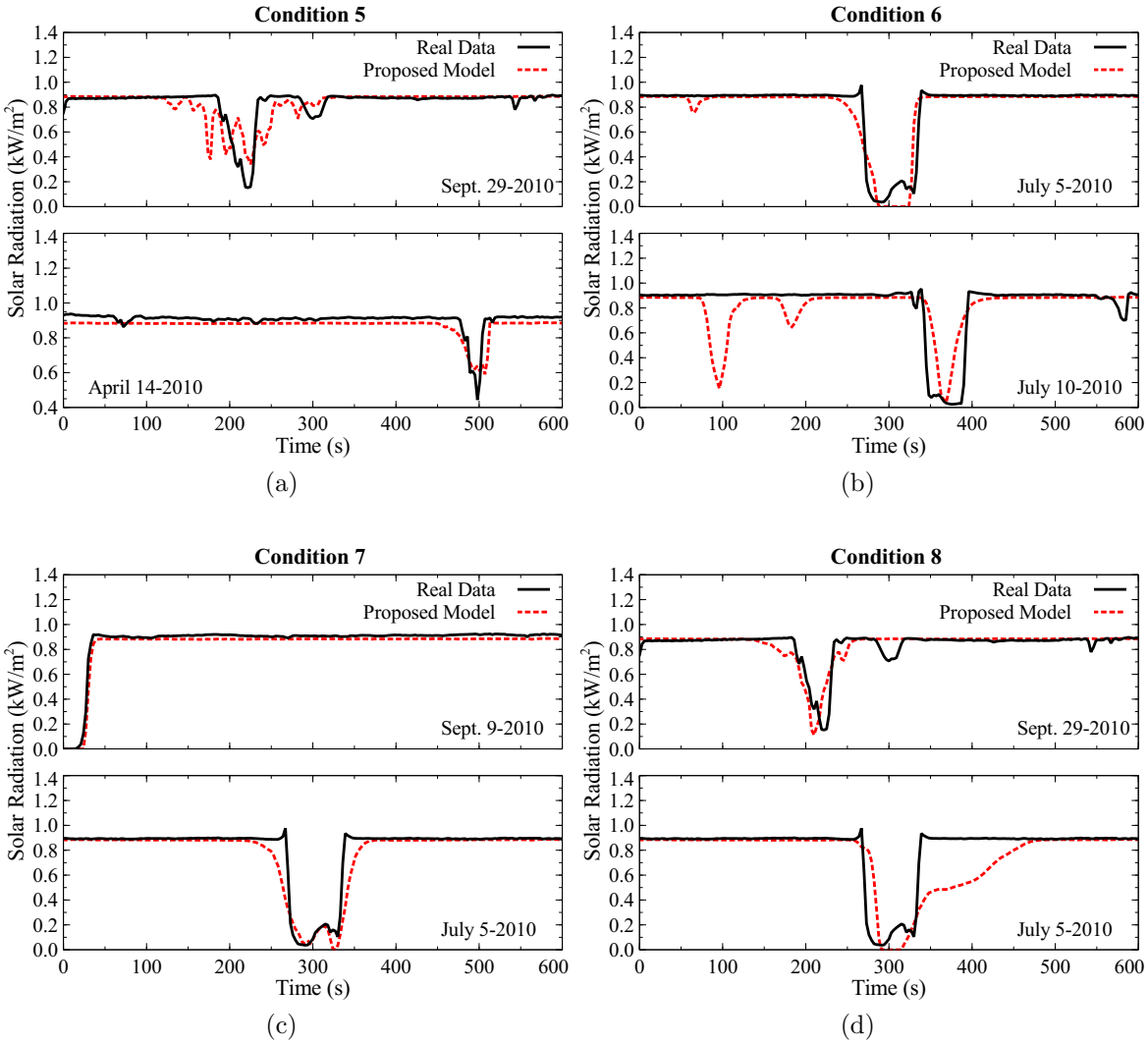

Figure 4.19: Comparison between real measurements and model results for each one of the eight experimental conditions

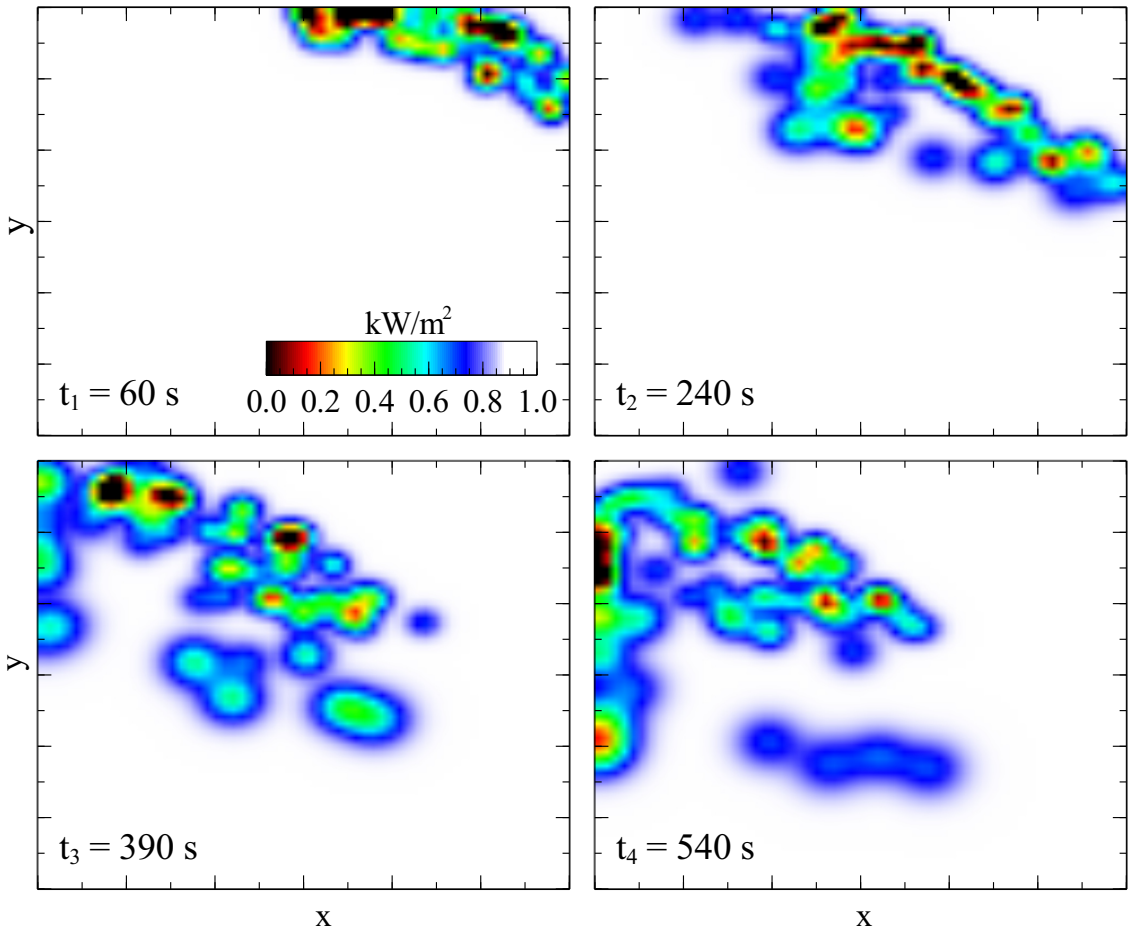

Figure 4.20: Variation of direct solar radiation (W/m^2) for several snapshots over time in a 2D domain

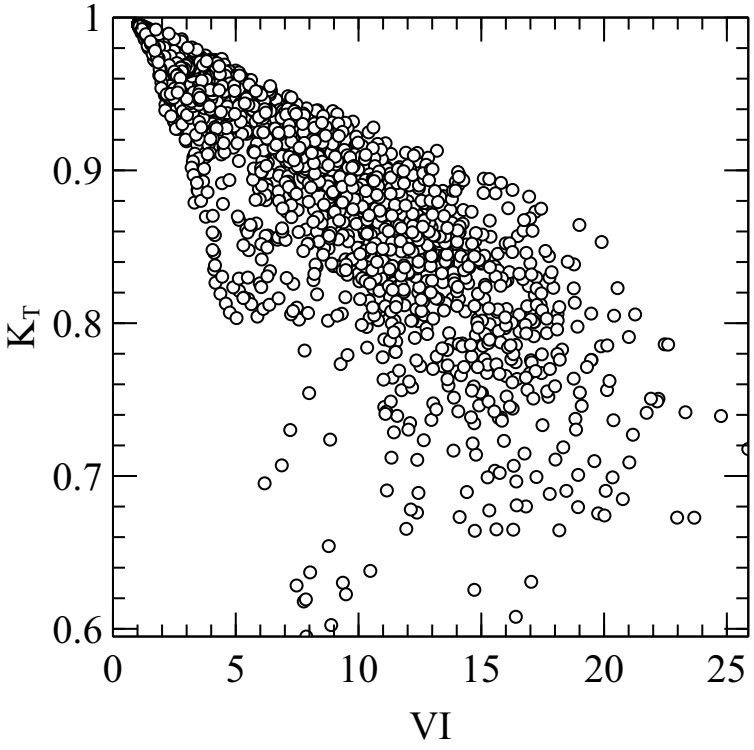

Figure 4.21: *Arrow head* plot for each time series created using the cloud shading model

Chapter 5

Implemented aiming strategy

Regularly, aiming strategies use as a manipulated variable target's location for each heliostat. It means there is an enormous amount of target's combinations for achieving a particular heat flux distribution. It is a task that becomes even harder if it is required to manage random atmospheric disturbances. In this research, it is proposed an aiming strategy based on a continuous control close loop, without directly using aiming points location as the manipulated variable. Following sections explain the proposed approach.

5.1 Manipulated variable

As explained above, due to the huge amount of heliostats in a regular solar field, calculating each aiming point is a complex task. Moreover, the effect of target's location movement for a single heliostat will probably be non-significant in the heat flux distribution over the central receiver. Thus, firstly it is proposed to develop a group behavior among heliostats' targets, this approach will allow reducing the number of manipulated variables, and its impact on the receiver will be larger.

5.1.1 Implemented group behavior

In a regular continuous process, valves are the commonly manipulated variables used by a control strategy. Its effect on the process depends on its aperture percentage. Present research proposes grouping heliostats in a way that its behavior can be related to a control valve per group. Let n be the number of heliostats whose target's location behavior will be linked. It is noteworthy n does not represent the total amount of heliostats in the solar field. Instead, it is a small fraction of it. Selecting the heliostats that belong to a particular group is a decision of the aiming strategy designer. The

Table 5.1: Even distribution of heliostats along x, in ascending order according its distance to the central receiver.

Distance	x
d_1	$x_1 = -a$
d_2	$x_2 = x_1 + \Delta x$
d_3	$x_3 = x_2 + \Delta x$
d_4	$x_4 = x_3 + \Delta x$
d_5	$x_5 = x_4 + \Delta x = +a$

number of heliostats within a group will not change during the execution of the aiming strategy (Just as valve size does not change in a regular process).

The first step consists of an even distribution of each heliostat within the group along with a variable "x"inside the interval $[-a; +a]$. In this research, the distribution is done beginning with the nearest heliostat to the central receiver. That is, assuming a particular group contains five heliostats, then its distribution along x is shown in Table (5.1). Assigning the x value using a different criterion (Distance to the receiver in this case), will probably not change the subsequent performance of the control strategy. It is because a group of heliostats should be composed by those with a similar location respect to the central receiver, then the amount of sun radiation redirected by each one should also be similar.

Once the x value is assigned, it is calculated value, r, according to Eq. (5.1). It means r is distributed as shown in Fig. (5.1). As can be seen, value r distribution depends on the value that κ takes. The higher κ then r will also be larger.

$$r = \frac{\kappa}{1 + \left|\frac{x}{\kappa}\right|^{2\cdot\kappa}} \tag{5.1}$$

This r value represents a radius around each target point of those heliostats in the group. Then each aiming point has to accomplish two tasks:

1. Try to reach the centroid of the whole group while respecting its assigned radius.

2. Make the centroid of the group to coincide with the fix aiming point designated to the entire group.

5.1.1.1 Distributing target points according to the assigned radius

It is important to respect the assigned r value given to each target point. However, all the heliostats into a group should be close each other. Adding this characteristic

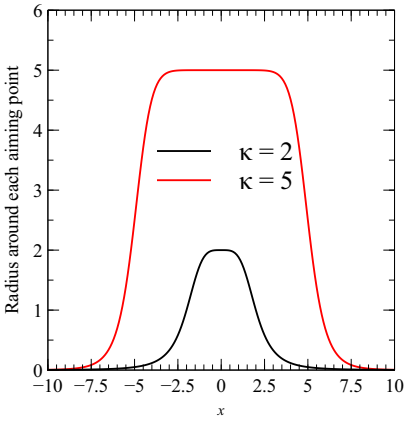

Figure 5.1: Distribution of r value for two different values of κ parameter

is done by setting a movement proportional to the distance between pairs of target points minus the radius of both. The movement is calculated as:

$$\Delta D = k_1 \cdot [d_{1-2} - (r_1 + r_2)] \tag{5.2}$$

where k_1 is a constant used for setting how fast the movement is, r_1 and r_2 are the assigned radii, and d_{1-2} is the distance between two target points.
Using this distance, and the equation of the straight line formed between the centers of each target point, the movement of each one along axes x and y is calculated as:

$$\Delta x = \sqrt{\frac{\Delta D^2}{1 + m^2}} \tag{5.3}$$

$$\Delta y = m \cdot \sqrt{\frac{\Delta D^2}{1 + m^2}} \tag{5.4}$$

The magnitude and the direction of the movement vector for each target point have been previously defined without sign. The sign is included by applying the following Equations:
For target point 1:

$$\Delta x_{TP_1} = C_1 \cdot \Delta x \cdot sign\,(\Delta D) \tag{5.5}$$

$$\Delta y_{TP_1} = C_1 \cdot \Delta y \cdot sign\,(\Delta D) \tag{5.6}$$

For target point 2:

$$\Delta x_{TP_2} = C_2 \cdot \Delta x \cdot sign\,(\Delta D) \tag{5.7}$$

Table 5.2: Average movements calculation for a five-agent group.

Pair of target points		Target point number				
A	B	1	2	3	4	5
1	2	Δx_{TP_1}	Δx_{TP_2}	-	-	-
1	3	Δx_{TP_1}	-	Δx_{TP_3}	-	-
1	4	Δx_{TP_1}	-	-	Δx_{TP_4}	-
1	5	Δx_{TP_1}	-	-	-	Δx_{TP_5}
2	3	-	Δx_{TP_2}	Δx_{TP_3}	-	-
2	4	-	Δx_{TP_2}	-	Δx_{TP_4}	-
2	5	-	Δx_{TP_2}	-	-	Δx_{TP_5}
3	4	-	-	Δx_{TP_3}	Δx_{TP_4}	-
3	5	-	-	Δx_{TP_3}	-	Δx_{TP_5}
4	5	-	-	-	Δx_{TP_4}	Δx_{TP_5}
Avg. Movement		$\overline{\Delta x_{TP_1}}$	$\overline{\Delta x_{TP_2}}$	$\overline{\Delta x_{TP_3}}$	$\overline{\Delta x_{TP_4}}$	$\overline{\Delta x_{TP_5}}$

$$\Delta y_{TP_2} = C_2 \cdot \Delta y \cdot sign\left(\Delta D\right) \tag{5.8}$$

In these equations, m stands for the slope of the straight line, C_1 is a constant that is +1 if target point 1 is on the left of target point 2, and -1 if target point 1 is on the right of target point 2. Moreover, C_2 is opposed to C_1, meaning that if C_1 is +1 then C_2 is -1. Once the movement is defined along the x axis, there are only two possible movements along y, meaning that C_1 and C_2 can be used for defining Δy. There are multiple pairs of target points, then for the same target point is possible to obtain several values for changes in x and y. Therefore, for obtaining a single value in each axis, the average among all the values is used (Table 5.2 shows a clearer explanation using a group with five heliostats as an example).

5.1.1.2 Coinciding the centroid of the group with an assigned central point

Each group moves around a fix point, it is done by making the centroid of the group to overlap this fix point. Adding this feature is done using the same set of equations shown before. The movements along x and y are calculated as:

$$\Delta x_{Centroid} = \sqrt{\frac{\Delta D^2_{Centroid}}{1 + m^2_{Centroid}}} \tag{5.9}$$

$$\Delta y_{Centroid} = m \cdot \sqrt{\frac{\Delta D^2_{Centroid}}{1 + m^2_{Centroid}}} \tag{5.10}$$

Where $\Delta D_{Centroid}$ is the distance between group's centroid and the assigned central point multiplied by a constant that can be used for setting how fast the movement is, as follows:

$$\Delta D_{Centroid} = k_2 \cdot \sqrt{(y_{fix\,point} - y_{Centroid})^2 + (x_{fix\,point} - x_{Centroid})^2} \tag{5.11}$$

Then displacements along x and y for all target points in the group are shown in Eq. (5.12) and Eq. (5.13), respectively. Where C_3 is -1 if the centroid is on the right side of the fixed point, and -1 if it is on the left side.

$$\Delta X_{Group} = C_3 \cdot \Delta x_{Centroid} \tag{5.12}$$

$$\Delta Y_{Group} = C_3 \cdot \Delta y_{Centroid} \tag{5.13}$$

The location of every target point is recalculated several times, according to Eq. (5.14) and Eq. (5.15), until the assigned radius to each target point is accomplished. Each iteration is part of the behavior of the whole group. It means that moving from a particular κ (In Eq. (5.1)) to another one is not a sudden movement. Figure 5.2 shows the movement of target points in one group from a smaller κ value to a larger one.

$$x_{TP_n} = x_{TP_n}^{Previous} + \overline{\Delta x_{TP_n}} + \Delta X_{Group} \tag{5.14}$$

$$y_{TP_n} = y_{TP_n}^{Previous} + \overline{\Delta y_{TP_n}} + \Delta Y_{Group} \tag{5.15}$$

It important to mention that in this research x_{TP_n} and y_{TP_n} refers to positions in a matrix, e.g. $x_{TP_1} = 10$ and $y_{TP_1} = 50$ indicates target point of heliostat 1 is located at row 50 and column 10 of a $2D$ matrix. This approach allows avoiding distortions due to the order of magnitude in the mesh used for determining the heat flux distribution. It also means that the result in Eq. (5.14) and Eq. (5.15) applied over the receiver is the rounded value. However, the $Previous$ value used for calculating the next time step (Eq. (5.14) and Eq. (5.15)) is still the unrounded value. As it refers to values k_1 and k_2 in Eq. (5.2) and Eq. (5.11) were set in a value of 0.35 to maintain the movement of the heliostats below a particular speed limit. According to the specification sheet published by SENER [107], the tracking speed of the system is $9°/min$ in the Elevation range, and $12°/min$ in the Azimuth range. Even though these values might not be a speed limit, they are a conservative initial guess point to

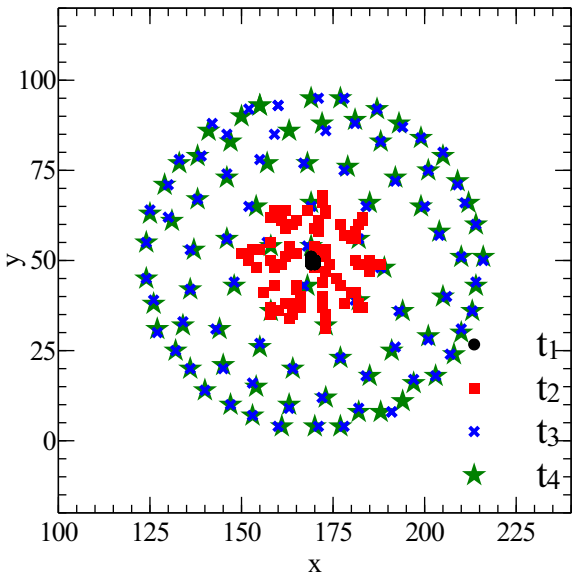

Figure 5.2: Target points movement from a low κ value until a large one at four time instants.

develop the strategy. Figure 5.3 shows the maximum Azimuth and Elevation speed obtained in a step test going from a κ value of 1 until 20 and back again to 1. Each iteration in the calculation of target point positions represents a sample time of 3 s, which is a value where fast DNI transients due to clouds can be seen.

Finally, after seeing the response of heliostats' target points as a group, it is evident that κ, and the assigned central point are crucial. For the aiming strategy that will be presented, these two variables per group are used as the manipulated variables.

5.1.2 Dividing heliostats in the solar field into groups

Once the behavior of each group can be manipulated using the procedure explained above, it is required to specify how the heliostat field is divided into groups. The primary goal is to maintain the same group those heliostats whose performance is similar. The first noticeable approach consists of dividing the field according to the distance between every heliostat and receiver's panels. The closest heliostats compose each section to a particular panel. Since there are 18 panels, the solar field is initially divided into 18 sections. Then, it is important to recognize that those heliostats in the same section have a different performance depending on its location respect to the receiver. Then, heliostats in the same section are divided into three groups. First

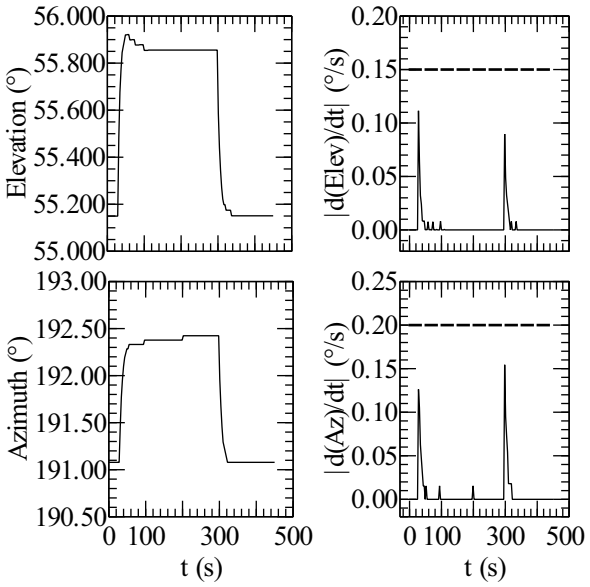

Figure 5.3: Maximum speed in Elevation and Azimuth obtained using k_1 and k_2 equal to 0.35 in a step test going from a κ value of 1 until 20 and back again to 1

two groups are composed by those heliostats whose distance to the receiver is lower than $400\,m$. Moreover, to have two groups with around the same *weight*, each row is intercalated. This grouping approach is explained in Fig. 5.4. Red heliostats belong to group 1, green ones to group 2, and blue to group 3. It has also been made a distinction between sections using star and round markers. Thus, since there are 18 sections, and three groups per section, therefore, there are 54 groups. It means there are 54 κ-values and 54 central points to assign. That is, the control strategy will determine 108 manipulated variables. It is important to remind that this is just one grouping approach, there might be other methods depending on the employed criteria.

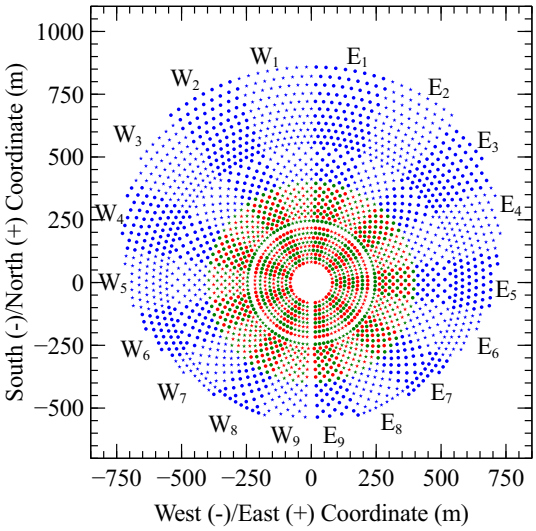

Figure 5.4: Distribution of the solar field in 54 groups to implement the proposed aiming strategy

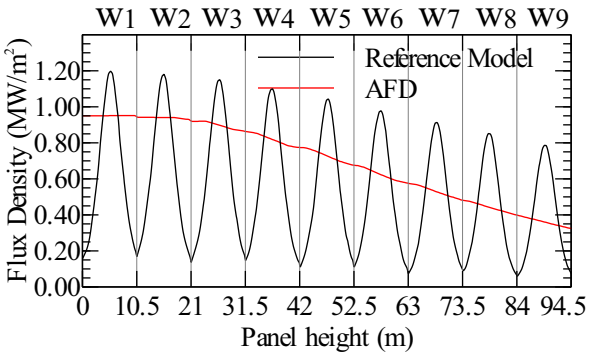

Figure 5.5: Allowable flux distribution (AFD) and real flux distribution for Gemasolar case during solstice summer noon [47].

5.2 Controlled variable

In daily basis operation, heat flux distribution over the central receiver must be very high but not over a defined limit. In the research presented by Sánchez-González [47], an allowable flux limit (AFD) is calculated to maintain receiver's operation below the allowable thermal stresses and corrosion limits. Figure 5.5 shows the AFD in summer solstice noon for Gemasolar solar plant [47]. It also shows the flux distribution using an equatorial aiming strategy. This graph explicitly shows average heat flux distribution along each panel of the central receiver. The proposed control strategy in this research uses as the controlled variable the difference between the maximum flux distribution per panel and its respective AFD value. Therefore, since there are 18 panels, there are also 18 controlled variables. Finally, the goal of the aiming strategy is to maintain these differences at zero (ideally) or lower, but never over this limit.

5.3 Dynamic Matrix Control

As shown in previous sections, the aiming strategy must handle a Multiple-Inputs Multiple-Outputs (MIMO) system with 18 controlled variables and 108 manipulated ones. In this kind of multivariate systems there is usually an interaction between input and output variables, that is, a manipulated variable will probably have an effect on several controlled variables. Classic control approaches do not easily handle this kind of interactions. Thus it might not be a right option to choose. On the other hand, a popular method is Model Predictive Control (MPC) techniques, which allow integrating all input/output variables into a single structure. In literature there are many MPC strategies [108]. The approach followed here is Dynamic Matrix Control

(DMC). It is one of the most popular techniques found at industrial level due it can be implemented using either data coming from either the actual process or a validated computational model. In a general overview, what a DMC strategy does is to take process responses stored in a matrix and then it solves a linear system by finding the values of the manipulated variables that minimize the differences between the setpoint and the controlled variables measurement.

5.3.1 Process identification

The first step for implementing a DMC strategy is to find the responses to construct the initial matrix. One way consists of finding the coefficients of a step response test in each manipulated variable and then record its effect on every controlled variable. It can be better explained using as an example group 1 of panel E_1 (Red star markers in Fig. (5.4)). A sudden change in its κ-value, going from $\kappa = 1$ until $\kappa = 20$ creates the responses shown in Fig. (5.6). It is noteworthy these responses are shown as deviation variables, meaning that to each point it is subtracted the initial steady state value. As explained above, the location of group's centroid is defined by the value assigned to the fix aiming point given to the group. In this research the movement of that point is horizontally constrained to be at the center of the panel, and vertically to that side of the panel where mass flow input stream is located. Meaning therefore that in the case of section E_1 this point can be moved towards the bottom of the receiver. A step change response for the fix aiming point of group 1 in section E_1 from $y_{Fix\ Aiming} = 0$ until $y_{Fix\ Aiming} = 20$ is shown in Fig. (5.7). Both graphs show a decrease in the controlled variable, where the larger change is seen in the panel belonging to that group. However, as expected, there is also an effect in neighbor panels.

5.3.2 DMC control law

The primary goal of a DMC strategy consist of solving the linear equation system showed in Eq. (5.16) for Δu –which is a vector that contains the changes in the manipulated variables –. Moreover, $\boldsymbol{A}$ is a matrix that contains the step test responses found previously (A) and the tuning parameter matrix ($\boldsymbol{\lambda}$), as shown in Eq. (5.17).

$$\boldsymbol{A} \cdot \Delta u = E \tag{5.16}$$

$$\boldsymbol{A} = \begin{pmatrix} A \\ \boldsymbol{\lambda} \end{pmatrix} \tag{5.17}$$

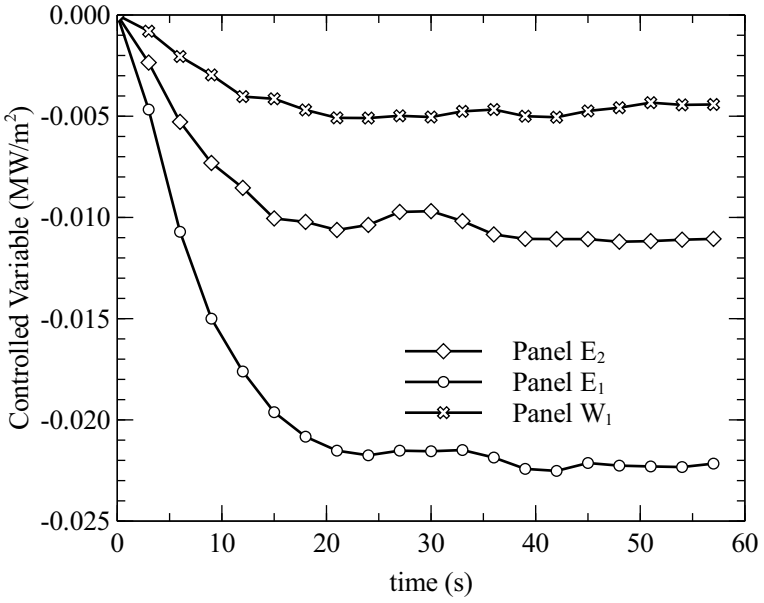

Figure 5.6: Step test response in κ-value of group 1 of section E_1

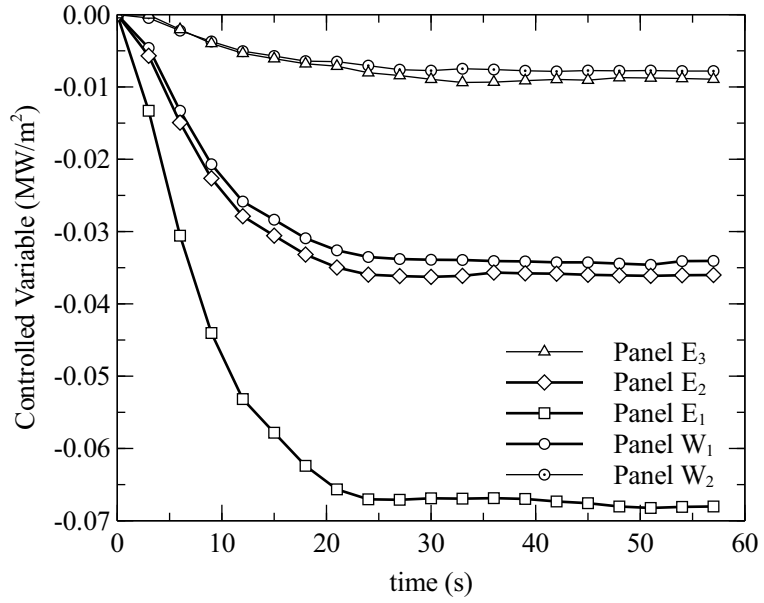

Figure 5.7: Step test response in the fix aiming point of group 1 of section E_1

Since it is a MIMO system, matrix A is built as follows.

$$A = \begin{array}{c} \\ C_1 \\ C_2 \\ \vdots \\ C_i \end{array} \begin{array}{c} \begin{array}{cccc} M_1 & M_2 & \cdots & M_j \end{array} \\ \begin{pmatrix} A_{11} & A_{12} & \cdots & A_{1j} \\ A_{21} & A_{22} & \cdots & A_{2j} \\ \vdots & \vdots & \ddots & \vdots \\ A_{i1} & A_{i2} & \cdots & A_{ij} \end{pmatrix} \end{array} \tag{5.18}$$

Where each A_{ij} corresponds to the step test responses in C_i by changing the manipulated variable M_j. Each matrix A_{ij} is built as shown in Eq. (5.19). Originally, the step test response is a vector $\boldsymbol{a} = [a_1,\ a_2,\ a_3, \cdots,\ a_p]$, however most MPC techniques are ideally meant to find its setpoint after a defined number of control steps, a value usually called control horizon (CH). On the other hand, PH stands for prediction horizon. This value depends on the number of terms contained in vector $\boldsymbol{a}$ and CH. This value can be considered a tuning parameter. It is tightly linked to the λ-values shown below [108]. Therefore, the CH is fixed now and tuning the strategy will be done through the λ-values. A stable strategy requires a large enough CH value, regularly between 5 and 10. In this research, it is fixed at 8. Since each step test response contains 20 values, then PH is equal to 27. Considering there are 54 controlled variables and 108 manipulated, then matrix A contains 486 rows and 864 columns.

$$A_{nm} = \text{PH} \left\{ \begin{array}{c} \overbrace{\phantom{\begin{pmatrix} a & a & a & a \end{pmatrix}}}^{\text{CH}} \\ \begin{pmatrix} a_1 & 0 & 0 & 0 \\ a_2 & a_1 & 0 & 0 \\ a_3 & a_2 & a_1 & 0 \\ a_4 & a_3 & a_2 & a_1 \\ a_5 & a_4 & a_3 & a_2 \\ \vdots & \vdots & \vdots & \vdots \\ a_{p-1} & a_{p-2} & a_{p-3} & a_{p-4} \\ a_p & a_{p-1} & a_{p-2} & a_{p-3} \\ a_p & a_p & a_{p-1} & a_{p-2} \\ a_p & a_p & a_p & a_{p-1} \\ a_p & a_p & a_p & a_p \end{pmatrix} \end{array} \right. \tag{5.19}$$

Furthermore, $\boldsymbol{\lambda}$ is a matrix that contains the values used as tuning parameters. In view there are 108 manipulated variables, then there are also 108 tuning parameters

(λ_j). This matrix is built as follows.

$$\boldsymbol{\lambda} = \begin{pmatrix} \lambda_1 \cdot \boldsymbol{I}_{CH\times CH} & 0 & \cdots & 0 \\ 0 & \lambda_2 \cdot \boldsymbol{I}_{CH\times CH} & \cdots & 0 \\ \vdots & \vdots & \ddots & 0 \\ 0 & 0 & \cdots & \lambda_j \cdot \boldsymbol{I}_{CH\times CH} \end{pmatrix} \tag{5.20}$$

Where $\boldsymbol{I}_{CH\times CH}$ stands for the Identity matrix with CH rows and columns.

Regarding vector E in Eq. (5.16), it is formed by concatenating the difference between the setpoint values and the updated prediction of the controlled variables (C_{P_U}), and a vector of zeros as follows:

$$E = \begin{bmatrix} C_{set} - C_{P_{t_U}} \\ \vec{0} \end{bmatrix} = \begin{bmatrix} c_{set_1} - c_{P_{U_1}} \\ c_{set_2} - c_{P_{U_2}} \\ c_{set_3} - c_{P_{U_3}} \\ \vdots \\ c_{set_i} - c_{P_{U_i}} \\ \vec{0} \end{bmatrix} \tag{5.21}$$

Where c_{set_i} represents the setpoint for the i^{th} controlled variable, and $c_{P_{U_i}}$ the updated prediction of the same i^{th} variable. Since there are 18 controlled variables, then i goes from 1 to 18. The vector of zeros must contain $CH \times j$ coefficients, where j is the amount of manipulated variables.

Each $c_{P_{U_i}}$ is calculated as:

$$c_{P_{U_i}} = \tilde{c_{P_i}} + e_{m_i} \tag{5.22}$$

e_{m_i} stands for modeling error, and it is obtained as:

$$e_{m_i} = c_i - \hat{c_{P_i}} \tag{5.23}$$

Where c_i is the current value of controlled variable i. In addition, previous equations (Eq. (5.22) & Eq. (5.23)) call for $\tilde{c_P}$ and $\hat{c_P}$. These two variables come from the predictions obtained using the responses in matrix A. Each controlled variable has an associated prediction vector (c_{P_i}) with PH coefficients. $\tilde{c_{P_i}}$ are the values of the vector c_{P_i} going from the second coefficient and repeating the last one to maintain the same length of vector c_{P_i}. Thus, first coefficient of c_{P_i} is called $\hat{c_{P_i}}$. It is used for determining the modelling error in Eq. (5.23). It is important to notice that the prediction vector, during the first iteration of the DMC algorithm, is a vector

containing the c_i value repeated PH times. From the second iteration onwards, the prediction vector is calculated as:

$$c_{P_i} = c_{P_{U_i}}^{Prev} + \tilde{A}_i \cdot \Delta u \tag{5.24}$$

Where $\tilde{A}_i$ is a sub-matrix of A as follows:

$$\tilde{A}_i = [A_{i1}\ A_{i2}\ A_{i3}\ \cdots\ A_{ij}] \tag{5.25}$$

Moreover, Δu is a vector containing the minimization solution of Eq. (5.16). If no constrains are included, the solution of the system can be calculated as:

$$\Delta u = [(\boldsymbol{A}^\intercal \cdot \boldsymbol{A})^{-1} \cdot \boldsymbol{A}^\intercal] \cdot E \tag{5.26}$$

On the other hand, if its required to include constrains, the problem can be treated using the quadratic programing approach as:

$$\Delta u = \underset{\Delta u}{min} \left(\frac{1}{2} \Delta u^\intercal Q \Delta u + f^\intercal \Delta u \right) \tag{5.27}$$

Where $Q = \boldsymbol{A}^\intercal \boldsymbol{A}$, $f = -2\boldsymbol{A}^\intercal E$ [109].

Solution vector Δu contains $CH \times j$ coefficients. The first CH values correspond to the first manipulated variable. Hence, to the process, it is sent just the first one. Following CH values belongs to the second manipulated variable, again just the first one is sent. The same applies to the other manipulated variables. Since $CH = 8$ in this case, then:

$$\tilde{\Delta u} = [\Delta u_1,\ \Delta u_9,\ \Delta u_{17},\ \cdots, \Delta u_{\,CH \times j - CH + 1}]^\intercal \tag{5.28}$$

Therefore, final control signal is:

$$u = u_{Prev} + \tilde{\Delta u} \tag{5.29}$$

Which is implemented in a feedback control loop as shown in Fig. (5.8). It is important to mention that here the sensor is assumed as a pure gain with a constant equal to 1.

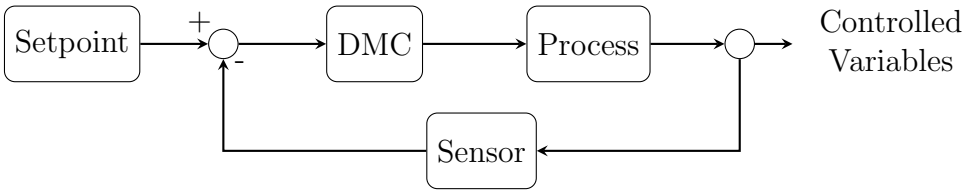

Figure 5.8: Feedback control loop using the DMC control law

Table 5.3: Levels used for carrying out the fractional factorial experiment 2^{6-1}

	Scattering			Centroid Movement		
Level	λ_1	λ_2	λ_3	λ_4	λ_5	λ_6
Low	0.05	0.05	0.05	0.05	0.05	0.05
High	0.15	0.15	0.15	0.15	0.15	0.15

5.3.3 Tuning procedure

Due to the high amount of parameters to determine, tuning this DMC strategy is a challenging task. As mentioned above, it is required to fix 108 tuning values. Since there are 3 groups per panel, then 3 values are linked to the *scattering* of the aiming points, and 3 values are associated with the position of each centroid. Here it is proposed to use the same set of 6 parameters for each section of the solar field, which highly reduces the complexity of this task. Its effect on the DMC strategy is statistically analyzed through an ANOVA (Analysis of variance). First, it is necessary to demarcate a first influence region. That is, specify the upper and lower boundaries for each parameter. As an initial guess, the strategy was tested by setting all the parameters at 1. This initial test showed that $\tilde{\Delta u}$ values are minimal, which implies that the control loop requires too much time for reaching the steady state. Then, to improve this behavior the initial test is done using 0.1, a lower value in the tuning parameters makes the control strategy more aggressive. Considering this first result showed a good performance, then it is proposed to carry out a fractional factorial design 2^{6-1} (32 runs), using limits presented in table 5.3. This fractional design is chosen due it provides a good resolution (VI), which means every principal effect is confounded with a 5-factor interaction. Moreover, executing 32 runs (which is half the full design) represent a lower time for running the whole test conditions.

The second aspect of developing the fractional factorial design consists of defining the response to be measured. For this analysis, it is used the area between the AFD limit and the actual flux distribution. The goal is to minimize this area. Ideally, it should be zero. Therefore, Table 5.4 shows the results obtained in each run of the

fractional design. It is important to mention this test is developed during the summer solstice at noon. Tuning parameters achieved in this configuration can be used for operation during any other time of the day, or even in other days of the year.

The ANOVA of these results is shown Table 5.5. It indicates that significant factors are λ_3 and λ_4, most important interactions are $\lambda_1\,\lambda_4$, $\lambda_1\,\lambda_5$, $\lambda_2\,\lambda_4$, and $\lambda_2\,\lambda_5$. Moreover, optimum tuning values are shown in Table 5.6. These results are fascinating because it is possible to withdraw some operation modes of the strategy. Let's assume a value of 0.05 in first three $\lambda's$ means the group may have a tendency to be quickly scattered if required (*Dispersed*). On the other hand, a value of 0.15 means this trend is lower (*Concentrated*). As it refers to λ_4, λ_5, and λ_6 a value of 0.05 means the group can easily move its centroid (*fast*), and a value of 0.15 produces a lower movement of the group (*slow*). Thus, optimum values indicate group 1 has to be *dispersed* and *slow*, while group 2 must be *concentrated* and *fast*. Even though tuning values for group 3 are not significant a value must be set, in this case it is chosen *dispersed* and *fast* due to its performance is slightly better (See Exp. Condition 18 and 22 in Table 5.4). Thus it allows its movement if required. The effect of tuning parameters can be seen in experimental conditions 18 (best), and 23 (second worst). Figure (5.9) shows a comparison between these two cases. Besides having a larger difference respect to AFD, experimental condition 23 takes too much time to reach the steady state. It is important to make clear these graphs show four controlled variables out of the 18 available. Non-shown responses have a behavior that is similar to these.

Table 5.4: Responses obtained for each experimental condition of the fractional factorial design

Exp. Condition	λ_1	λ_2	λ_3	λ_4	λ_5	λ_6	Response
1	0.05	0.05	0.05	0.05	0.05	0.05	42.2464
2	0.15	0.05	0.05	0.05	0.05	0.15	41.0244
3	0.05	0.15	0.05	0.05	0.05	0.15	40.9194
4	0.15	0.15	0.05	0.05	0.05	0.05	41.4474
5	0.05	0.05	0.15	0.05	0.05	0.15	42.2177
6	0.15	0.05	0.15	0.05	0.05	0.05	40.7863
7	0.05	0.15	0.15	0.05	0.05	0.05	41.2136
8	0.15	0.15	0.15	0.05	0.05	0.15	41.0482
9	0.05	0.05	0.05	0.15	0.05	0.15	44.3899
10	0.15	0.05	0.05	0.15	0.05	0.05	49.1010
11	0.05	0.15	0.05	0.15	0.05	0.05	40.6714
12	0.15	0.15	0.05	0.15	0.05	0.15	43.2585
13	0.05	0.05	0.15	0.15	0.05	0.05	43.7954
14	0.15	0.05	0.15	0.15	0.05	0.15	48.8187
15	0.05	0.15	0.15	0.15	0.05	0.15	40.6479
16	0.15	0.15	0.15	0.15	0.05	0.05	43.8122
17	0.05	0.05	0.05	0.05	0.15	0.15	44.9851
18	0.15	0.05	0.05	0.05	0.15	0.05	40.4172
19	0.05	0.15	0.05	0.05	0.15	0.05	49.6056
20	0.15	0.15	0.05	0.05	0.15	0.15	43.7294
21	0.05	0.05	0.15	0.05	0.15	0.05	44.8948
22	0.15	0.05	0.15	0.05	0.15	0.15	40.5281
23	0.05	0.15	0.15	0.05	0.15	0.15	49.8343
24	0.15	0.15	0.15	0.05	0.15	0.05	43.9236
25	0.05	0.05	0.05	0.15	0.15	0.05	44.3342
26	0.15	0.05	0.05	0.15	0.15	0.15	48.8430
27	0.05	0.15	0.05	0.15	0.15	0.15	48.8824
28	0.15	0.15	0.05	0.15	0.15	0.05	50.3158
29	0.05	0.05	0.15	0.15	0.15	0.15	44.6686
30	0.15	0.05	0.15	0.15	0.15	0.05	48.1375
31	0.05	0.15	0.15	0.15	0.15	0.05	48.4716
32	0.15	0.15	0.15	0.15	0.15	0.15	44.4298

Table 5.5: Analysis of variance of fractional factorial experiment results

Source	Sum of Squares	DoF	Mean Square	F_{ratio}	P_{value}	Significance ($P_{value} < 0.05$)
A: λ_1	0.1454	1	0.1454	0.07	0.8006	-
B: λ_2	0.2855	1	0.2855	0.13	0.7239	-
C: λ_3	1.5062	1	1.5062	0.70	0.4234	-
D: λ_4	59.8314	1	59.8314	27.68	0.0004	Significant
E: λ_5	80.0194	1	80.0194	37.02	0.0001	Significant
F: λ_6	0.7653	1	0.7653	0.35	0.5651	-
AB	6.4847	1	6.4847	3.00	0.1139	-
AC	1.2647	1	1.2647	0.59	0.4620	-
AD	60.1357	1	60.1357	27.82	0.0004	Significant
AE	25.4667	1	25.4667	11.78	0.0064	Significant
AF	1.7923	1	1.7923	0.83	0.3839	-
BC	0.4888	1	0.4888	0.23	0.6446	-
BD	21.4842	1	21.4842	9.94	0.0103	Significant
BE	54.4586	1	54.4586	25.19	0.0005	Significant
BF	2.2441	1	2.2441	1.04	0.3323	-
CD	1.5691	1	1.5691	0.73	0.4142	-
CE	0.9474	1	0.9474	0.44	0.5229	-
CF	0.0169	1	0.0169	0.01	0.9313	-
DE	0.3670	1	0.3670	0.17	0.6890	-
DF	0.6194	1	0.6194	0.29	0.6042	-
EF	0.3720	1	0.3720	0.17	0.6870	-
Total error	21.6169	10	2.1617			
Total (corr.)	341.8820	31				

Table 5.6: Optimum values of tuning parameters for DMC strategy

λ_1	λ_2	λ_3	λ_4	λ_5	λ_6
0.05	0.15	0.05	0.15	0.05	0.05

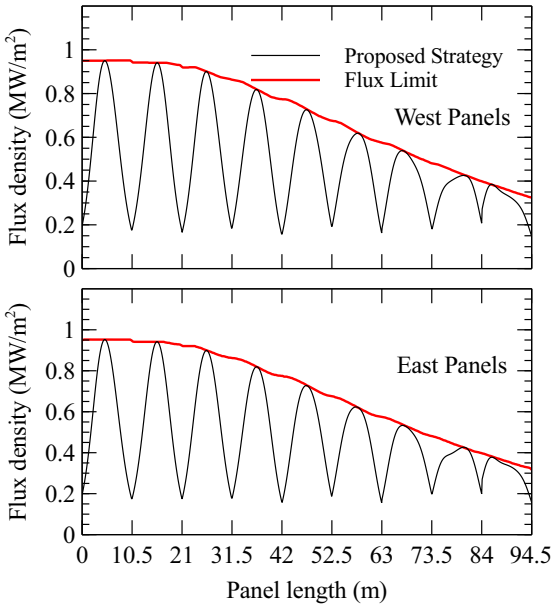

(a) Flux profiles Exp. Cond. 18

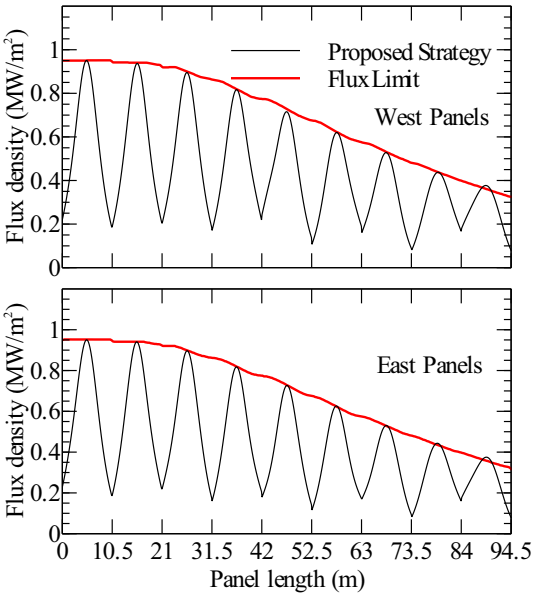

(b) Flux profiles Exp. Cond. 23

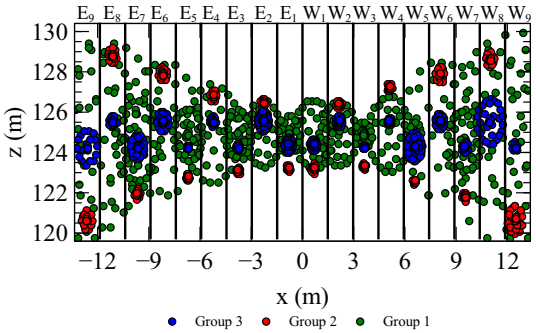

(c) Aiming points Exp. Cond. 18

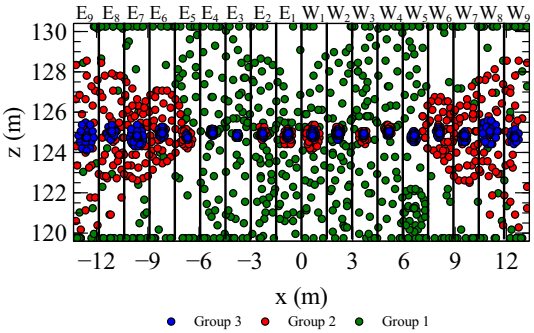

(d) Aiming points Exp. Cond. 23

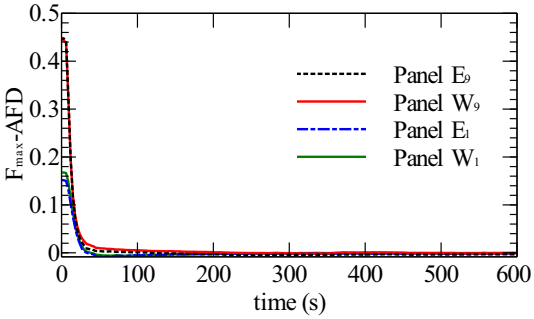

(e) Cont. var. responses for Exp. Cond. 18

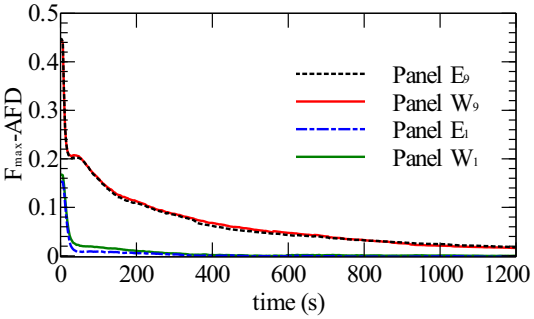

(f) Cont. var. responses for Exp. Cond. 23

Figure 5.9: Performance comparison between Exp. Cond. 18 and 23

Chapter 6

Heat flux distribution according to a predefined profile

6.1 Steady state responses

The performance of the developed strategy using similar AFD values is analyzed by comparing to the results shown in the reference paper [27]. This comparison is carried out at three different solar times i.e. 7 am, 9 am, and 12 pm and the corresponding heat flux profiles are shown in Fig. (6.1) to (6.3). For all cases, the fluid is divided into two separate loops, East and West, beginning at the bottom side of panels E_1 and W_1 and exiting at the top section of panels E_9 and W_9. This energy acceptance path of the fluid dictates the shape of the AFD curve so that the pipe material does not exceed allowable thermal's stresses and corrosion limits.

Figure (6.1) shows that the dissimilarities in performance for the last three panels are more noticeable than in previous panels comparing the proposed and reference aiming methodologies. It is because of the symmetrical aiming approach applied in the reference method. In this approach, rows of aiming points are shifted from the equator of the receiver towards the upper and lower edges to achieve the desired flux densities resulting in a two-shoulder like-shape profile. In contrast, the flat profile is less pronounced in the proposed methodology due to the displacement characteristics of heliostats closer to the tower and their dispersion behavior.

Figures (6.2) and (6.3) show the corresponding aiming point pattern and flux distribution over the receiver panels as seen in all the studied cases in Fig. (6.1). It can be observed that more concentrated aiming occurs in panels E_1 and W_1 where higher AFD is allowed, and a larger dispersion of aiming occurs in low AFD regions such as panels E_9 and W_9. The most dispersed case can be seen at the 7 am, especially on the East side. It is because lower solar irradiance in the early morning and markedly

lower on receiver's East side which requires lower mass flow rate to achieve the design fluid outlet temperature. It also implies a lower AFD is required.

Initially, the control strategy aims the heliostats of each section to the middle of its respective panel. Under clear sky conditions, each panel is receiving more energy than is allowed. Since the proposed aiming strategy is constrained to use all the solar field, it means some of the aiming points are relocated over nearby panels instead of being defocused. This sharing behavior contributes to the spillage. Nevertheless, using all the available heliostats is beneficial to maintain a balanced performance of the solar receiver in operating scenarios when moving clouds shade a particular section of the solar field, and nearby unshaded solar field could assist. This characteristic distinguishes the proposed methodology from the reference as aiming points in the latter are always restricted to movements across rows at different heights of the panel, and stay on the one panel associated with the particular section of the heliostat field.

Figure (6.4) shows the previously discussed sharing behavior among panels and the sections of the solar field. Blue bars represent the percentage of heliostats that are aimed over the main panel. Yellow bars represent those aiming points located at the panels that follow the main panels. In the same way, green and red bars account for the percentage of aiming points that are far from the main panels. As an example, all heliostats in section E_9 for the 12 pm case are not focused over panel E_9 , instead around 30% are focused to nearby panels W_8, W_9, E_8, and E_7.

Regarding the amount of harvested energy the proposed aiming strategy shows lower values compared to that obtained by Sánchez using a different aiming strategy (without sharing behavior among panels). There is around 5 % less total energy reaching on the receiver for the 12 pm case. Figure (6.5) shows in more detail the deviations between both strategies. These differences may be caused by variations in the solar field optical model as discussed in section 3.2.5, or the aiming procedure itself. Regarding the spillage results in Table 6.1 confirm that the proposed aiming strategy (with sharing behavior) does not significantly impact the reduction in energy collected by the receiver given the difference in spillage.

Another significant result is the robustness of the aiming strategy to different working conditions. As mentioned in the tuning parameters section, the aiming strategy was designed and optimized using the 12 pm case (Fig. (6.2a)). The general behavior is promoted using tuning parameters that maintain group 3 concentrated and close to the equator, group 2 spread as much as required, and group 1 moving along the panel's axial axis. It is a behavior that applies to achieve different AFD requirements at various solar times. It is because the logic behind the DMC algorithm

Table 6.1: Experimental conditions used to analyze the differences between the aiming strategies

Input Factors		Response Variables	
Type of strategy	Solar time	Total Energy (MW)	η_{Spill}
Developed Model	7	2.647	0.238
Developed Model	9	3.686	0.228
Developed Model	12	4.03	0.232
Reference Model	7	2.758	0.226
Reference Model	9	3.797	0.223
Reference Model	12	4.234	0.214

is not changing. In other words, operation under other conditions does not alter the fact that spreading and moving away two groups of heliostats reduces the heat flux gradients. It can be said that the aiming strategy will use these movements as much as necessary to reach the desired objective.

Results presented in this chapter also show that the DMC approach can successfully distribute solar radiation over the central receiver as per defined profile without a real-time parallel execution of an optical model such as HFLCAL. Matrices of data constitute the model used inside the DMC structure. This information is obtained in a first design stage from the optical model implemented here, and then for a subsequent implementation, it can be further fine-tuned using data from the actual process if necessary. In any case, the goal is to extract the relevant characteristics of the dynamic behavior of the system. Available aiming strategies commonly rely on detailed equation-based models to work, which can become an inconvenience due to random variations not taken into account by its model.

6.2 Cloud shading disturbance

The primary goal of this aiming strategy consists of correctly handling unexpected disturbances during solar field and receiver operations. As previously mentioned, one of the most shared and challenging disturbances to control are DNI variations due to a partially shaded solar field caused by moving clouds. The disturbance used here is designed to be relatively fast, which is around 2 min. so that control efforts are mainly focused on changing the aiming points instead of molten salt mass flow inside the receiver. This assumption allows working using a constant AFD curve at a constant mass flow rate. Figure (6.6a) shows the disturbance behavior at four different times, while Fig. (6.6b) shows some of the patterns generated and a comparison against actual measurements [94]. The cross marks shown in Fig. (6.6a) correspond to the

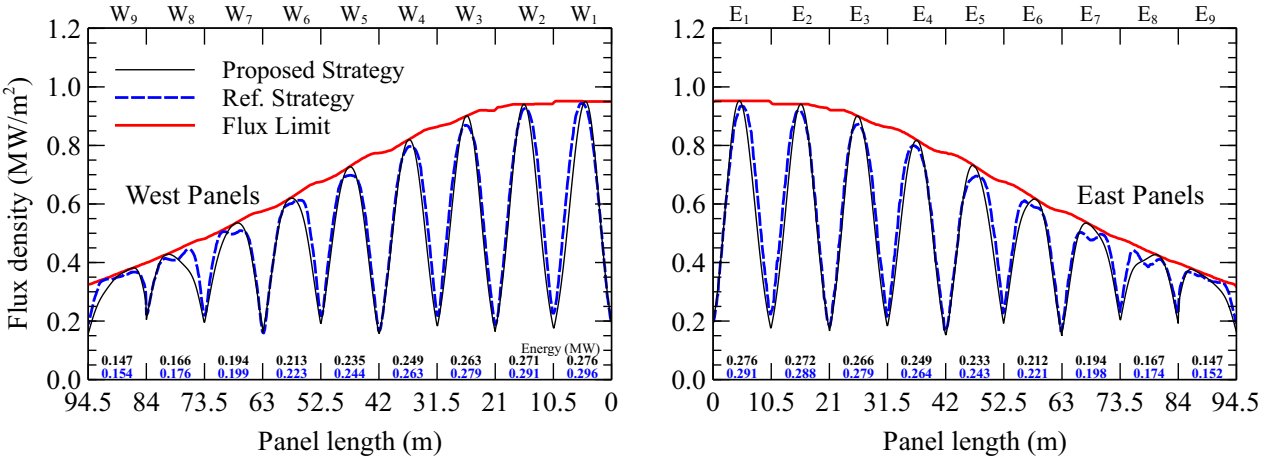

(a) 12 pm

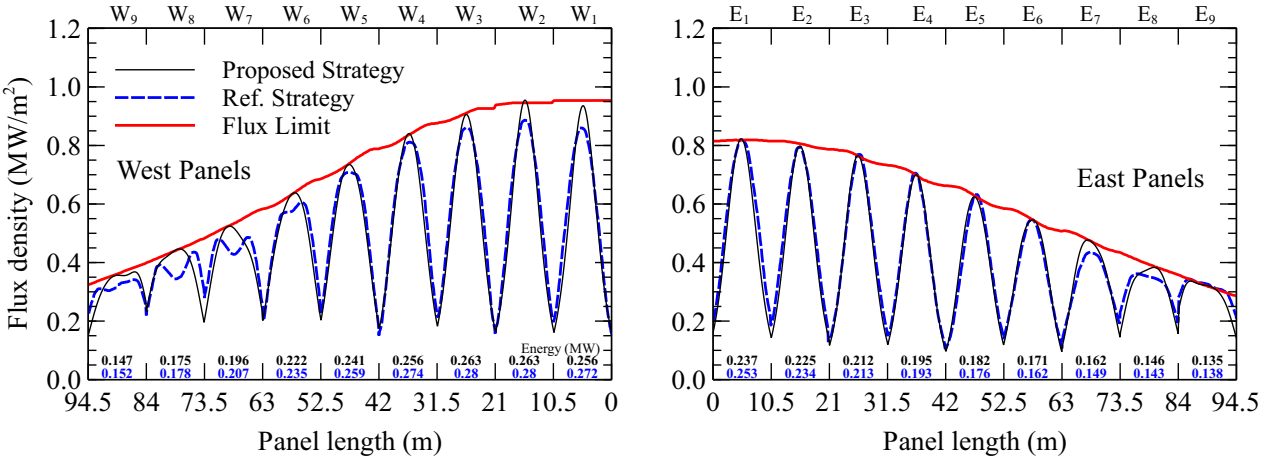

(b) 9 am

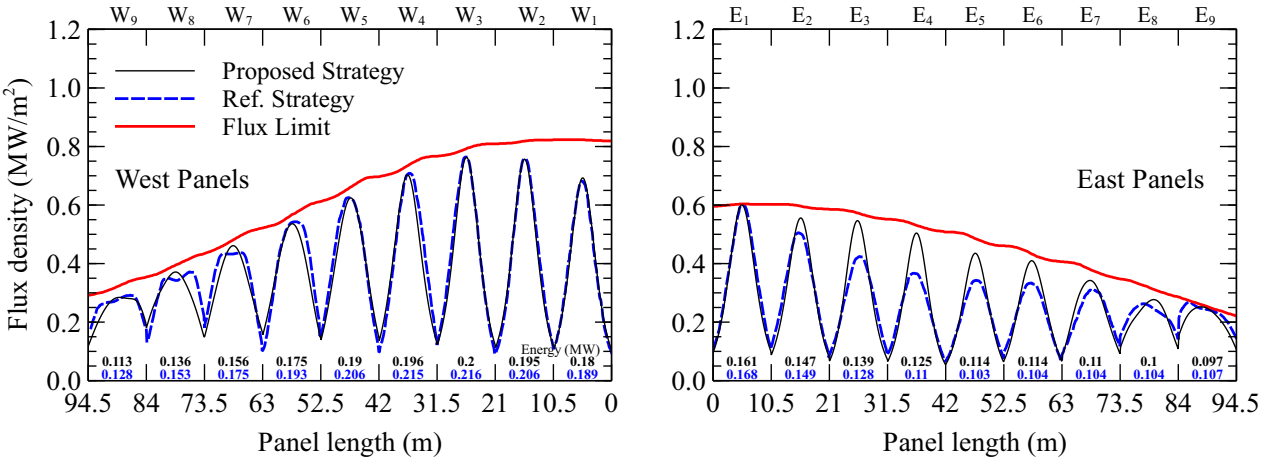

(c) 7 am

Figure 6.1: Comparison of the panel's flux density distribution throughout west and east panels between reference and proposed aiming strategies at different solar hours.

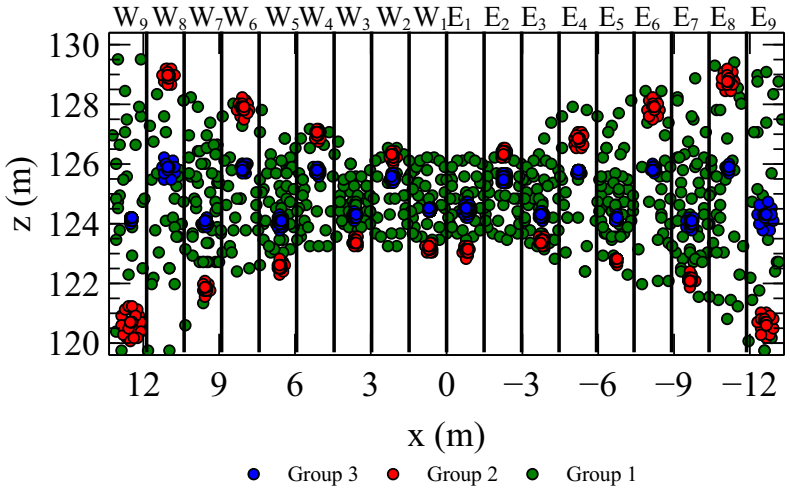

(a) 12 pm

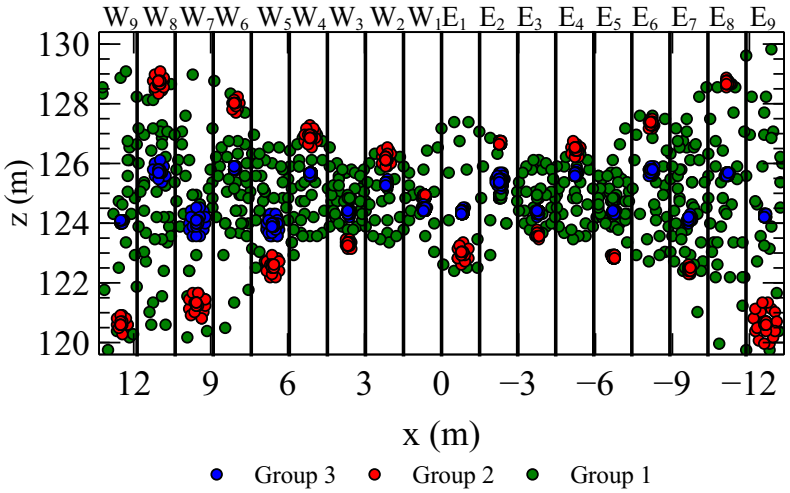

(b) 9 am

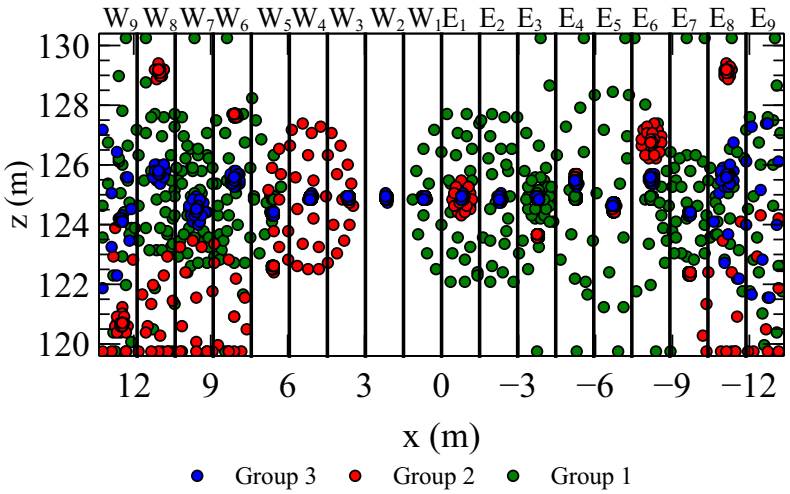

(c) 7 am

Figure 6.2: Aiming points distribution throughout west and east panels for the proposed aiming strategies at different solar hours.

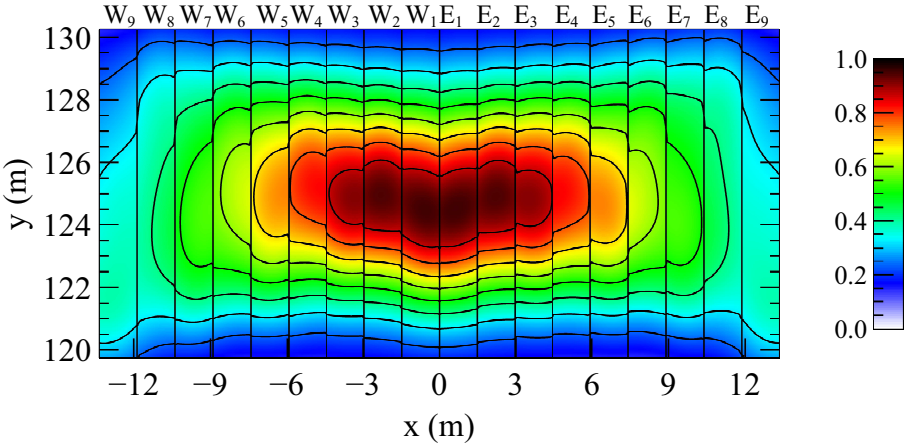

(a) 12 pm

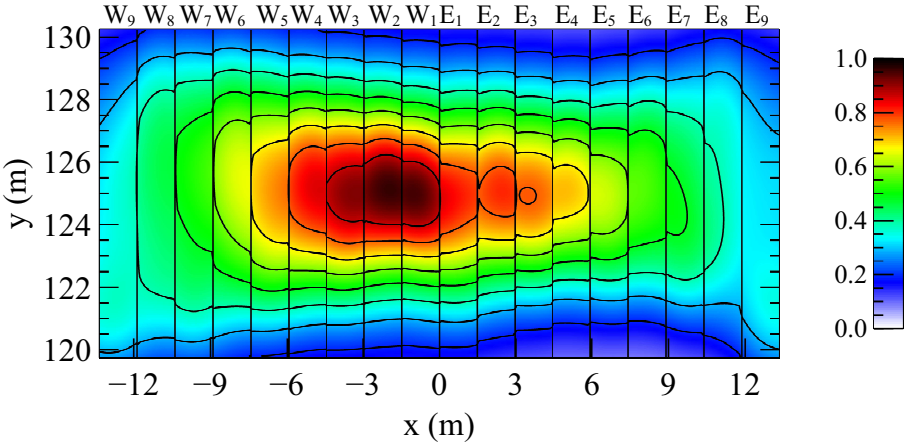

(b) 9 am

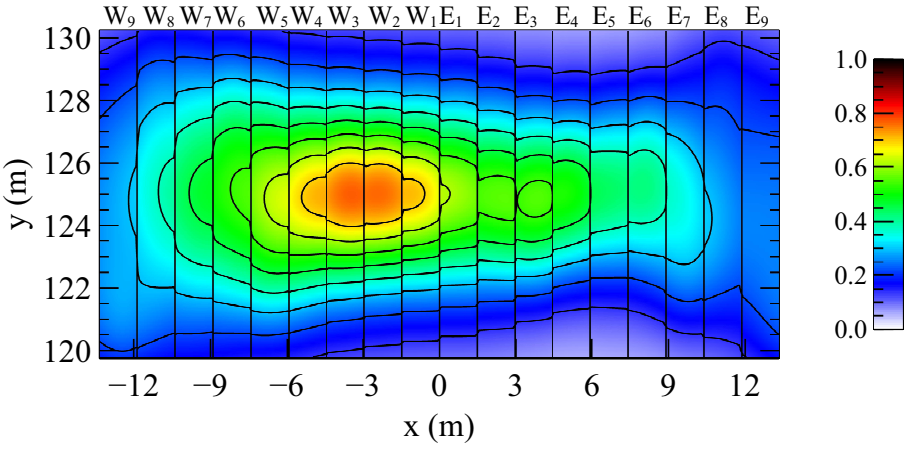

(c) 7 am

Figure 6.3: Flux distribution (MW/m^2) throughout west and east panels for the proposed aiming strategies at different solar hours.

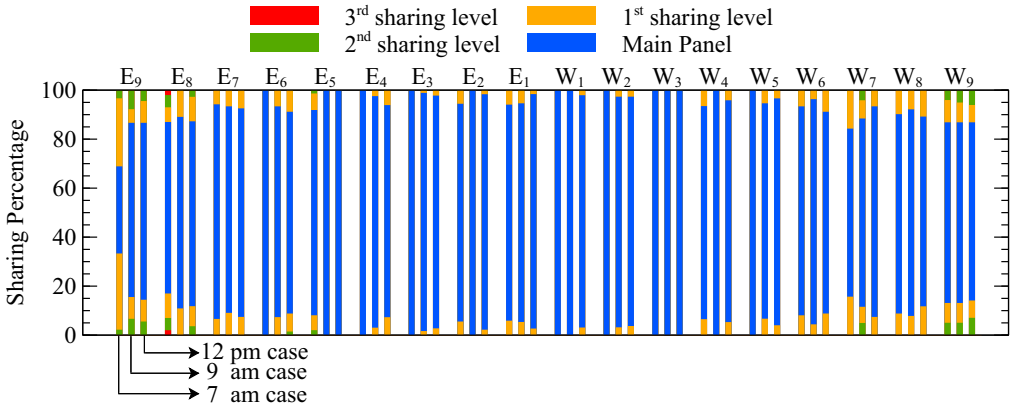

Figure 6.4: Amount of aiming points shared by the corresponding main and neighbor panels at solar time 7 am, 9 am, and 12 pm

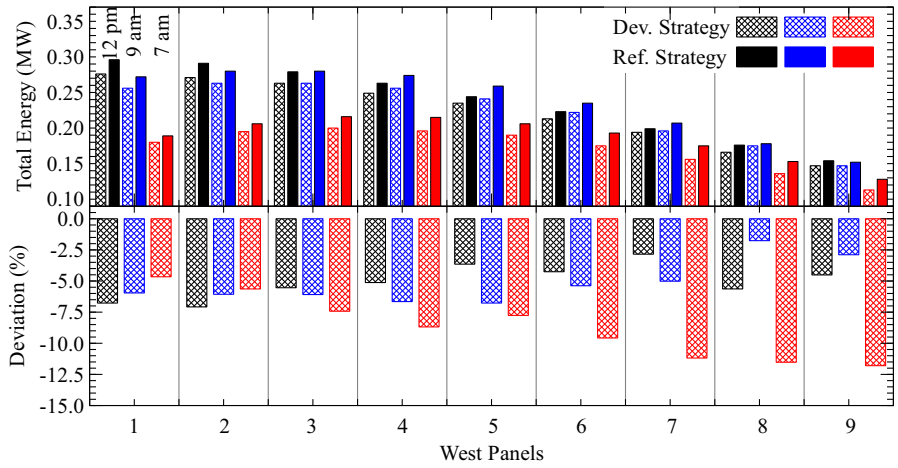

(a) West Side

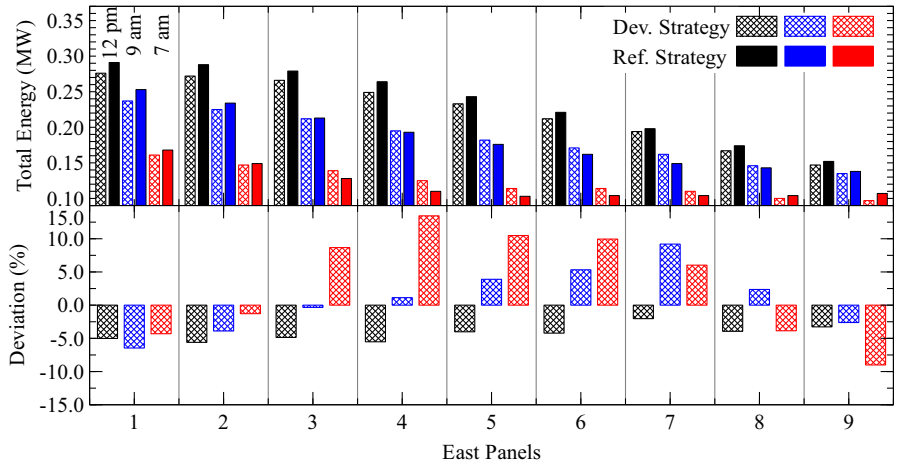

(b) East Side

Figure 6.5: Total energy obtained from each strategy at solar time 7 am, 9 am, and 12 pm

spatial location with the solar transient in Fig. (6.6b). The goal of this model is not to exactly represent a particular set of curves. Instead, it consists of generating DNI transients close to the actual phenomenon. Additionally, it is worth mentioning that the values in Fig. (6.6a) represent the ratio between the DNI at time instant t (DNI_t) and the clear sky DNI value (DNI_{cs}). Hence, the DNI is calculated as this ratio multiplied by the desired clear sky value. This project uses a clear sky value of 930 W/m^2 for solar noon, which is the same used by Sánchez-González [27].

6.3 Transient responses under a disturbance

6.3.1 Base aiming strategy

Once the desired disturbance has been developed in the cloud model and applied to the solar central receiver model, the aiming strategy is tested to assess its performance while facing DNI changes. The first test is performed using the feedback control loop as shown in Fig. (5.8) and the disturbances presented in Fig. (6.6). It is noteworthy to indicate the system is reaching the steady state operation at around 900 s and then the cloud disturbance is introduced to the solar field.

Figure (6.7) shows that the base aiming strategy can manipulate the target points to maintain the controlled variables at its set point during steady-state conditions. Once the cloud shade starts covering a section of the solar field, the available energy delivered to each panel decreases. It implies that the aiming strategy concentrates the target points to maintain the controlled variables close to zero (reach the AFD as close possible). Then, just right after the cloud has been clear from shading the solar field, a high amount of energy is expected to be directed to the spot where the aiming points are previously concentrated, which could severely damage the receiver panel. Hence the target points must be dispersed.

Figure (6.8) shows a transient response example of the aiming points that belong to a partially shaded sector of the solar field. This graph presents the x and y coordinates along time for those heliostats that belong to sector W_1, clearly indicating how the aiming points are concentrated and re-dispersed on the receiver panel.

Even though the base aiming strategy works well during steady-state operations, there are still two undesired operating conditions affecting the solar receiver. Firstly, this approach does not avoid the overshoot seen in the controlled variables. This energy peak takes place during a short period. However, this is not desired due to the risk of damaging the central receiver. Secondly, the rate of heating of the central

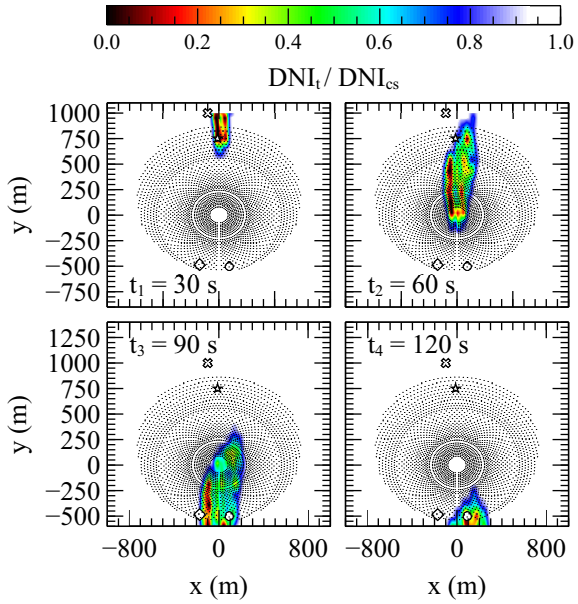

(a) DNI_t/DNI_{cs} variation along time caused by North-South cloud

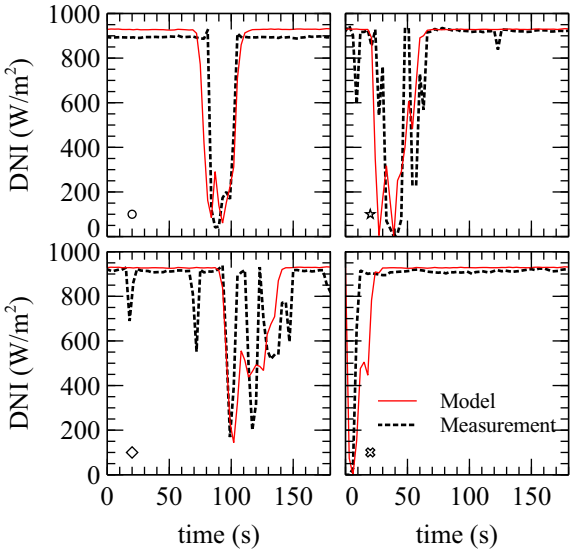

(b)

Figure 6.6: (a) DNI transient variation due to a moving cloud from North towards South, (b) Comparison of generated transient curves against real data [94]. Cross marks link the spatial location in (a) and the plotted DNI transients in (b).

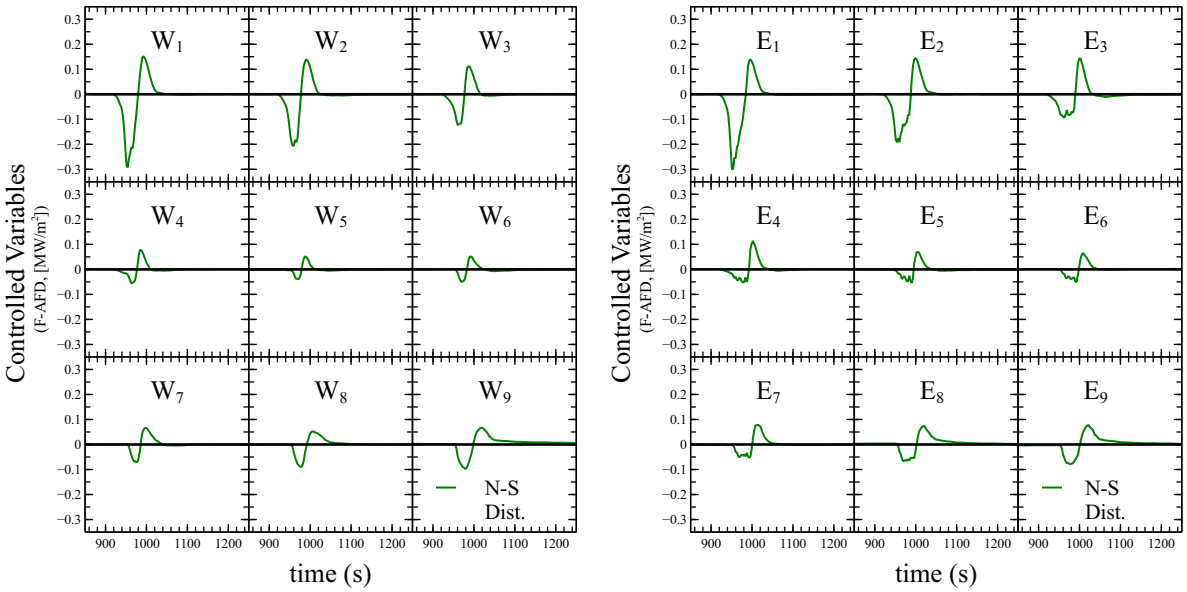

(a) West Side Panels

(b) East Side Panels

Figure 6.7: Base aiming strategy performance using the North-South cloud disturbance at solar noon.

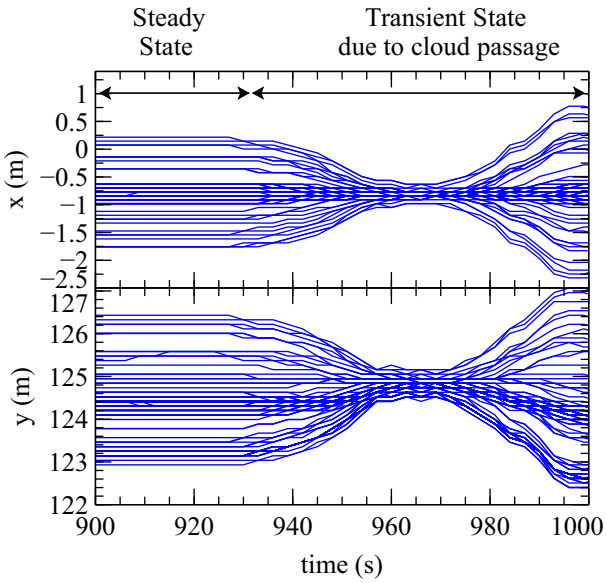

Figure 6.8: Aiming point variation along time for section W_1 of the solar field while North to South cloud disturbance takes place.

receiver is very high; it is reaching around 1000 $^{kW}/_{m^2 \cdot min}$ in panel W_1 which could potentially shorten the receiver operating life.

The results also show a stronger variation in panels W_1, W_2, W_3, E_1, E_2, and E_3. This behavior is attributed to the cloud direction and the solar field zones that it covers. For the North to South disturbance case, the sector with a larger number of heliostats (Northern section) is covered first, which initially generates a large decrement in heat flux. During this period, it is also evidenced the sharing behavior from the unshaded sector W_4 towards W_3 as an effort to maintain controlled variables close to their set points. When the cloud starts to disappear from those heliostats closer to the central receiver in the Northern field, it is harder for the control strategy to quickly respond to the sudden increase in energy availability resulting in overshooting seen in the controlled variables.

6.3.2 Modified aiming strategy

A solution to overcome the previously mentioned issues is analyzed through two different modifications to the base strategy.

6.3.2.1 Discrete adapting set point strategy

This modification consists of adapting the set point according to the rate of change of the controlled variables. Thus, if the controlled variables are quickly increasing, then the set point is decreased to promote a higher dispersion of the target points. This solution is implemented using the following rules:

(i) Under clear sky conditions, the steady-state set point is held at a value of zero. Otherwise, under DNI disturbances the set point is held at least in a safe value of -0.05.

(ii) When the system is under a cloud disturbance:

$$Set\ Point = \begin{cases} 0 & if \quad 0 \leq C(t) - C(t-1) \leq a \\ \mathrm{SP}_1 & if \quad a < C(t) - C(t-1) \leq b \\ \mathrm{SP}_2 & if \quad C(t) - C(t-1) > b \end{cases}, \tag{6.1}$$

where SP_1, SP_2, a, and b are values to be defined. The values used in this project are -0.1, -0.2, 0.005, and 0.01 respectively, based on the responses seen in the base case.

(iii) Once the previous rule is not triggered, the process gradually goes back to the steady-state set point. Triggering the last rule is achieved using the variance

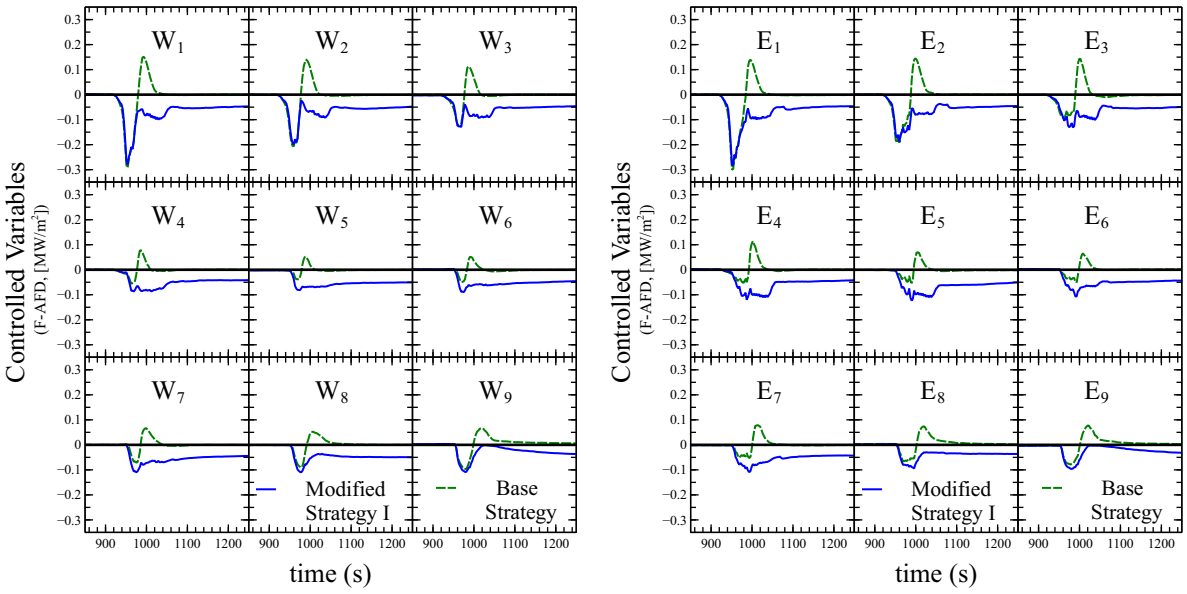

(a) West Side Panels

(b) East Side Panels

Figure 6.9: Discrete adapting set point strategy performance during the DNI transient from North towards South during summer solstice at noon.

increment along time of the controlled variables due to the decrement caused by the cloud presence.

Figure (6.9) exposes the results obtained using the base and modified aiming strategy presented in this section (Modified Strategy I). The whole response to the modified aiming strategy is not shown to make a clearer comparison with the base case. Nevertheless, the modified strategy reaches the steady state value at around 2500 s. With regards to the overshoots found in the original strategy, the implemented modifications show a significant improvement. The proposed changes prioritize receiver's safety by enhancing the settling time of the controlled variables and decreasing its original aggressiveness. Hence, due to the unknown high variability nature of the disturbance, the control strategy is forced to take this trade-off performance. Even though the overshoot issue is solved, there are still some panels with a high heating rate. This problem can be seen mainly on the north-side panels, with a heating rate similar as the given by the base strategy.

6.3.2.2 Continuous set point modification + PI controller transient backup

In this case, the modification involves moving the set point to the minimum value measured for each controlled variable. Once the cloud starts disappearing the con-

trolled variable starts increasing over the set point, which promotes a dispersion of the aiming points. This spreading behavior is not fast enough to counteract the fast DNI transient. Thus, to improve the performance of the DMC algorithm, it is added the effect of a PI controller proportional to the error between the set point and the controlled variable. The PI controller is implemented to accomplish several tasks. Firstly, it helps to spread group 1 more in each section, and also increase the spread for group 2 in sections W_8, W_9, E_8, and E_9. Secondly, this modified strategy add more movement to the centroid of groups 2 and 3 for all sections. It is worth mentioning that the set point is not maintained at the minimum value, instead once the controlled variables start increasing as the cloud is disappearing, the set point also increases but at a slow rate. Additionally, after the set point keeps rising, the PI controllers diminish its effect, and eventually, only the DMC algorithm is controlling the process.

Figure (6.10) shows the performance of this strategy (Modified Strategy II) and a comparison with the performance of previously seen cases. The results indicate the modified strategy accomplishes the two requirements to operate the central receiver under a cloud disturbance. It avoids an overshoot in the controlled variables and also makes possible a slow heating rate while taking the process back to the steady state. Compared to previous approaches, the controlled variables reach similar minimum values in panels W_1, W_2, E_1, and E_2. While in the rest of the panels those minimums values are lower. In fact, the settling time using the new modification is not as high as in the previous case, which is shown in the responses for panel W_1 in Fig. (6.11).

6.3.3 Aiming point performance analysis under different disturbances

The methodology in section 6.3.2.2 has proved to handle the DNI variation due to introducing North-South disturbance successfully. Now it is also important to study its performance and applicability of the control strategy under other cloud disturbances i.e. moving from West to East, and from North West to South East, as seen in Fig. (6.12). These clouds encompass a partial shading on sectors different from the North and South studied before and also promotes a lighter DNI variation while it crosses over the solar field.

Figure (6.13) shows the performance of the modified control strategy II to overcome transient operations due to N-S (cloud type 1), W-E (cloud type 2) and NW-SE (cloud type 3) disturbances. The responses demonstrate that the control strategy works in all the studied cases. For the north to south cloud disturbance case, the

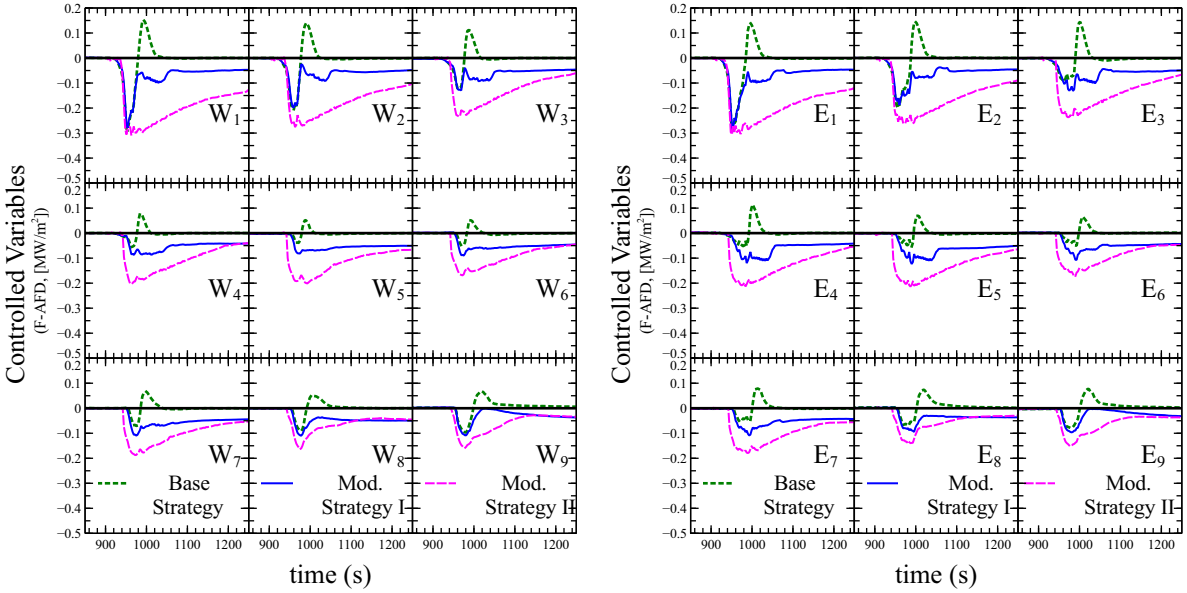

(a) West Side Panels

(b) East Side Panels

Figure 6.10: Base and modified aiming strategies I and II (presented in sections 6.3.2.1 and 6.3.2.2) performance during the DNI transient from North towards South during summer solstice at noon.

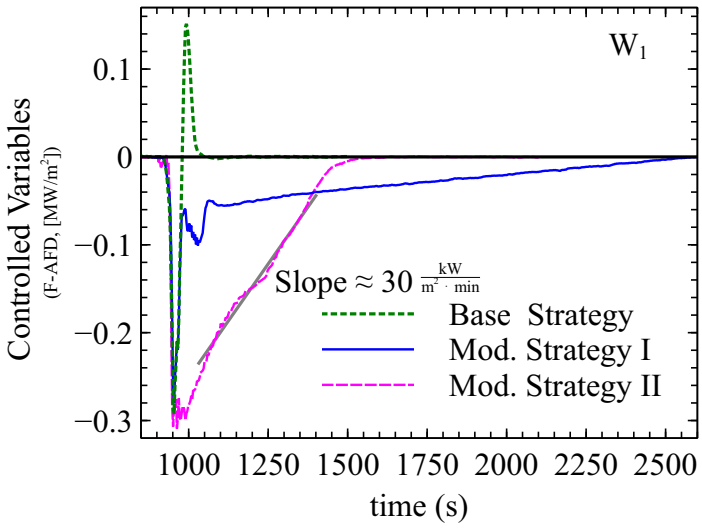

Figure 6.11: Zoom of the aiming strategies performance during the whole test for panel W_1 using DNI transient from North towards South during summer solstice at noon

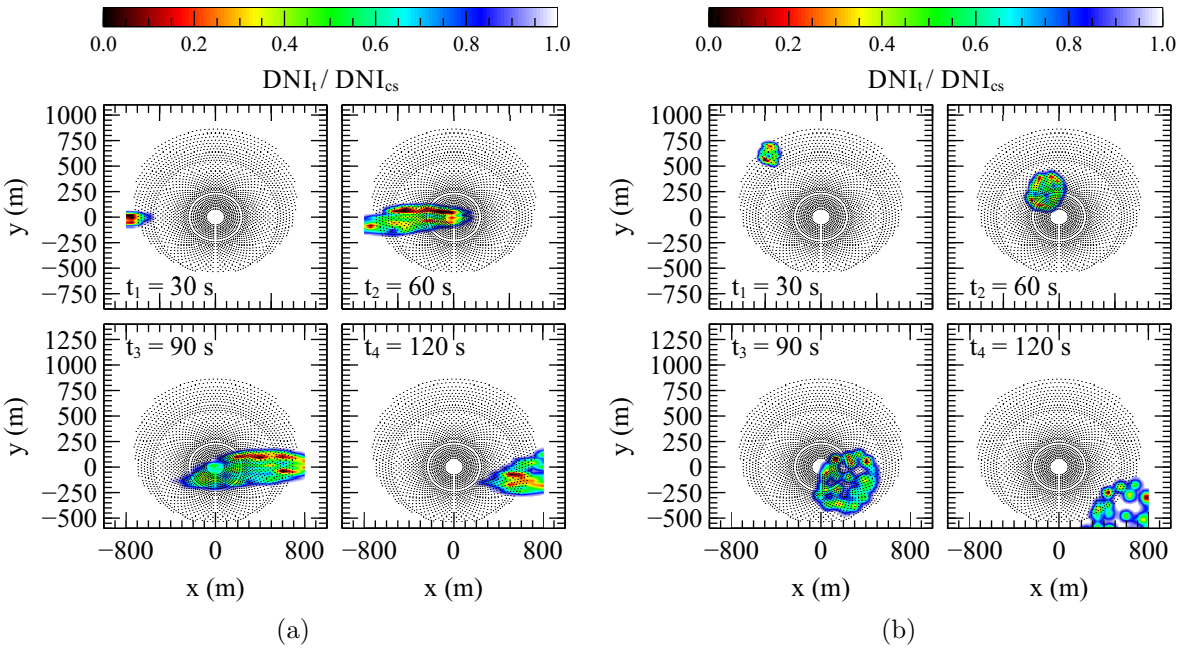

Figure 6.12: DNI transient variation due to a moving cloud from: (a) West towards East, (b) North-West towards South-East

most critical panels are on the most southern two (E9 and W9), with a slightly high heating rate in recovery after the cloud disappears. This behavior is caused by the lower manipulability of the aiming points as these are almost well spread to accomplish the smaller AFD requirement.

In regards with the West to East cloud, panels E_4, and E_5 are the ones where the highest decreased in heat flux. Similar performance is not seen in panels W_4 and W_5 due to the moving direction of the cloud. That is, the cloud starts covering those heliostats on the West side that are far from the tower, hence its effect is weak. However, when the cloud reaches the Eastern side, it starts covering those heliostats that are close to the receiver, which causes a higher impact on the heat flux.

Considering the North-West to South-East disturbance, its impact on the central receiver is in overall lower than the other clouds, and with a similar behavior over the last three panels. Despite the differences, the pattern in each case is well defined. Firstly, the cloud promotes a fast decrement on the heat flux. Secondly, the control strategy handles the transient and maintains the controlled variables as steady as possible. Thirdly, it slowly takes the process back to the steady state.

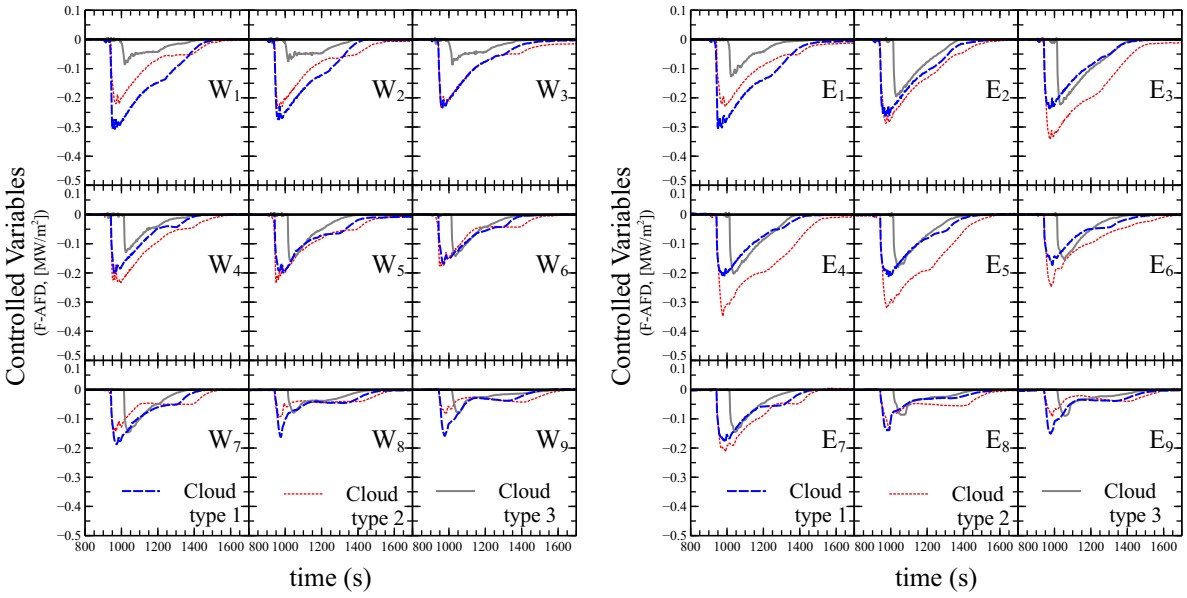

(a) West Side Panels

(b) East Side Panels

Figure 6.13: Controlled variables responses at solar noon for each disturbance, North to South (type 1), West to East (type 2), and North-West to South-East (type 3).

Chapter 7

Aiming strategy using receiver's temperature measurements

7.1 Controlled variables

This section shows the implementation of the aiming strategy using temperature measurements, due to this is a variable commonly known during the operation of many processes. Additionally, because the main thermal stresses in receiver's pipes take place at its inner wall towards the side where solar radiation is incoming [61], the controlled variable is, therefore, the maximum temperature measured in that section. It assumes these values are available through the data acquisition system found in the central receiver. The maximum allowable temperature calculated in section 3.4 indicates the set point that the aiming strategy must achieve to operate safely and efficiently.

7.2 DNI transient disturbances

As mentioned before, one of the goals to achieve is to handle unexpected disturbances properly. The designed disturbance for the performance analysis of the aiming strategy consists of a cloud moving from North towards South. The study bases its attention in two aspects of the cloud, its velocity, and the DNI dropping. Thus, it considers four cloud cases, (*i*) fast and thin, (*ii*) fast and thick, (*iii*) slow and thin, and (*iv*) slow and thick. The fast cloud moves at 12 m/s approximately, the slow cloud moves at 6 m/s, and the DNI dropping promoted by the thick cloud is four times the value given by the thin cloud. Figure (7.1) shows the clouds for cases *i* and *iv*.

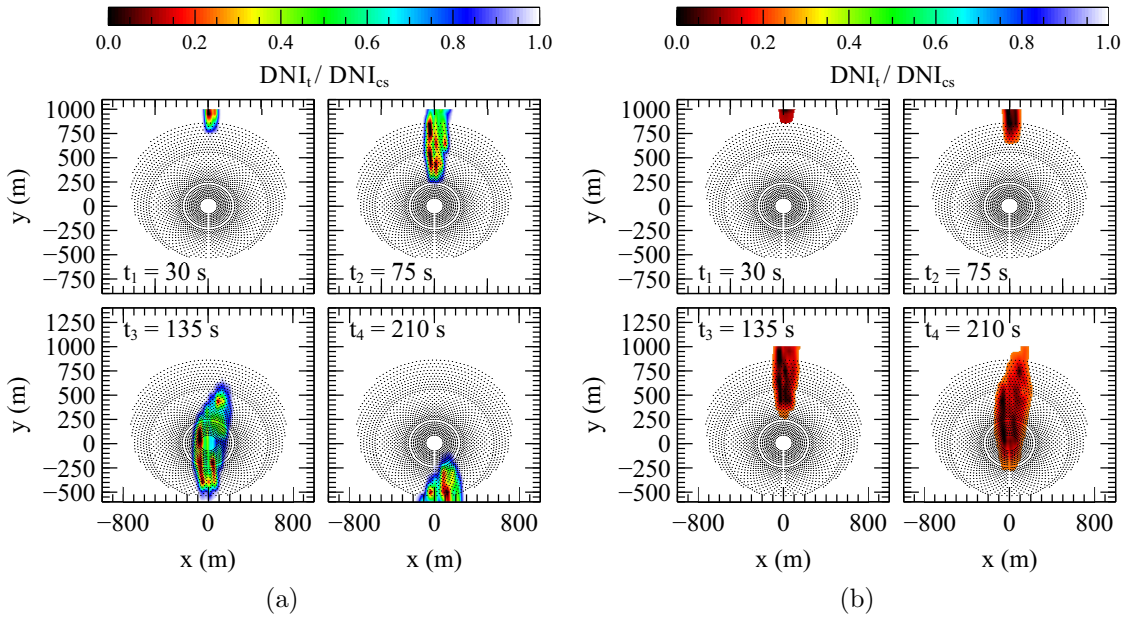

Figure 7.1: DNI transient variation due to a moving cloud from North towards South, (a) Fast and thin cloud, (b) Slow and thick cloud. $\text{DNI}_{cs} = 930$ W/m^2 at solar noon during summer solstice [27].

7.3 System responses to DNI transients

7.3.1 Base aiming strategy performance

After setting the aiming strategy and the DNI disturbances, the analysis of the closed control loop for the whole system takes place. Figure (7.2) shows the results at 12 pm solar hour; it indicates that the controlled variables for the six first panels, on the west and east sides of the receiver, behave as expected. That is, after the temperature decreases due to the presence of a cloud, the control strategy takes the process back to the initial steady state at a safe heating rate. Nevertheless, the controlled variables in the last three panels of each side show a high heating rate of around 1.5 min. approximately. This issue is due to the amount of DNI drop caused by the cloud, and the sudden availability of the energy once the cloud disappears from that section of the solar field. As explained earlier, the implemented control strategy disperses the aiming points as the cloud goes over the field to avoid sudden temperature increases after the cloud disappears. However, that approach is not enough in the last panels because these sections have already a high spread degree in the aiming points required to maintain the temperature at the desired setpoint. These results indicate that there is a temporary energy excess while taking the process back to the steady state.

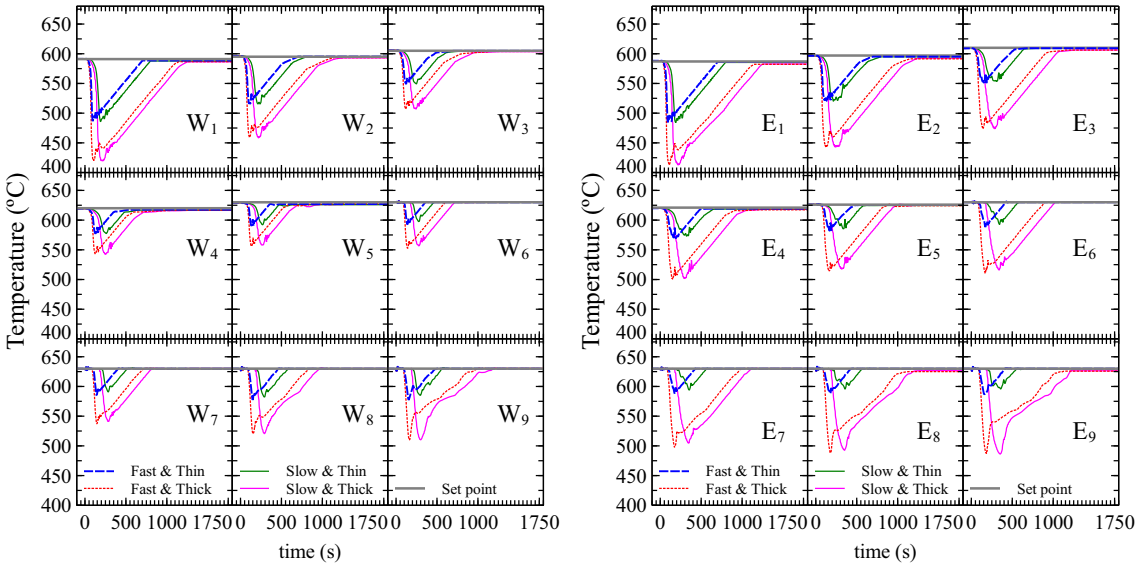

(a) West Panels

(b) East Panels

Figure 7.2: Aiming strategy performance using different DNI disturbances at 12 pm solar hour during summer solstice.

In regards to the outlet fluid's temperature, the results in Fig. (7.3) show that the system is not reaching the initial value in some of the tests. Since the mass flow remains constant for every test, then outlet fluid's temperature should go back to the initial point. It is a problem caused by the aiming point dispersion to handle the cloud disturbance and the inability of the control strategy to re-obtained the original dispersion degree for each group. Thus, it is plausible that the control strategy finds a different dispersion degree for all the groups that can maintain the controlled temperature in pipe's wall. For example, the final dispersion degree for groups 1 and 2 could be lower than initially, but group 3 dispersion needs to be larger. That behavior implies it is possible to obtain slightly lower energy than initially to heat the fluid.

7.3.2 Modified aiming strategy performance

Given there are small issues with the performance in some of the panels, the approach requires some modifications. Firstly, since the high heating rate in the last three panels is due to a temporary excess of energy, then it is necessary to defocus some of the heliostats momentarily. The deactivation takes place if the spreading value, for each group, is over a preset value. The number of deactivated heliostats is determined

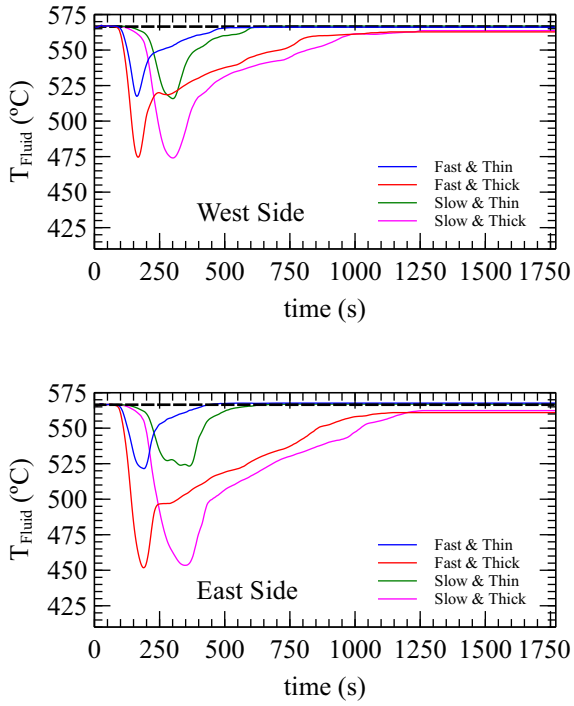

Figure 7.3: Outlet fluid temperature variation after the studied DNI disturbances go over the solar field at 12 pm solar time.

as follows:

$$n_{deact} = \left\lfloor \int k_{deact} \cdot min\left(\mathrm{SD}_{max} - \mathrm{SD}\left(t\right),\ 0\right) \right\rfloor \tag{7.1}$$

Once the strategy starts taking the system to the initial steady state value, it will concentrate the aiming points. Thus, if the spreading degree of a group is below a preset value, the strategy starts activating the heliostats again, as follows:

$$n_{act} = \left\lfloor \int k_{act} \cdot max\left(\mathrm{SD}_{min} - \mathrm{SD}\left(t\right),\ 0\right) \right\rfloor \tag{7.2}$$

Secondly, the spreading degree of group 2 constrains the maximum spreading degree for group 3. Analogously, the spreading degree of group 1 limits maximum spreading degree for group 2. In this way, the aiming strategy ensures a final pattern similar to the initial steady state. Thirdly, in case the outlet temperature is not reaching the initial set point, and if there are deactivated heliostats, the aiming strategy starts activating them until achieving the desired value.

Figure (7.4) shows the results using the modified aiming strategy. These indicate all the controlled variables behave as required regardless the DNI disturbance. The

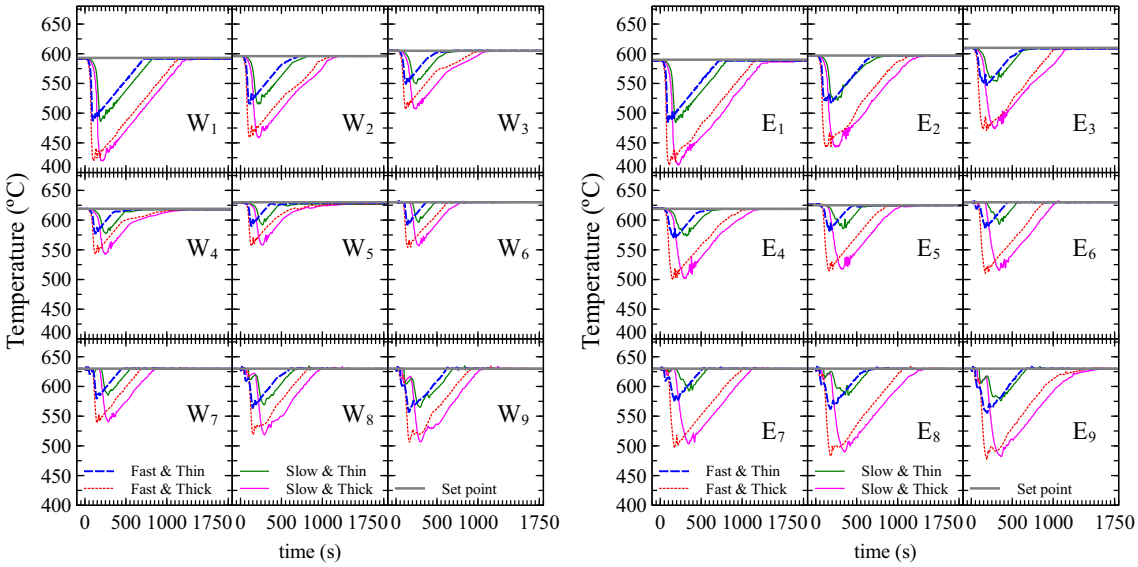

(a) West Panels (b) East Panels

Figure 7.4: Modified aiming strategy performance using different DNI disturbances at 12 pm solar hour during summer solstice.

primary goal of the aiming strategy consists of safely taking the process to the steady state. That is after the cloud disturbance disturbs the system, it is mandatory to heat the receiver slowly avoiding any significant temperature increase. In this case, the strategy follows the assigned set point maximum increment of 10 °C/min approximately. The results also illustrate that thick cloud has a larger impact on the controlled variables than a thin cloud with the same characteristics. Additionally, this effect is slightly higher if the cloud is slowly moving over the solar field. Looking at the fluid's outlet temperature in Fig. (7.5), all the studied cases go back to the initial steady state value as required, with an average heating rate of 6 °C/min approximately.

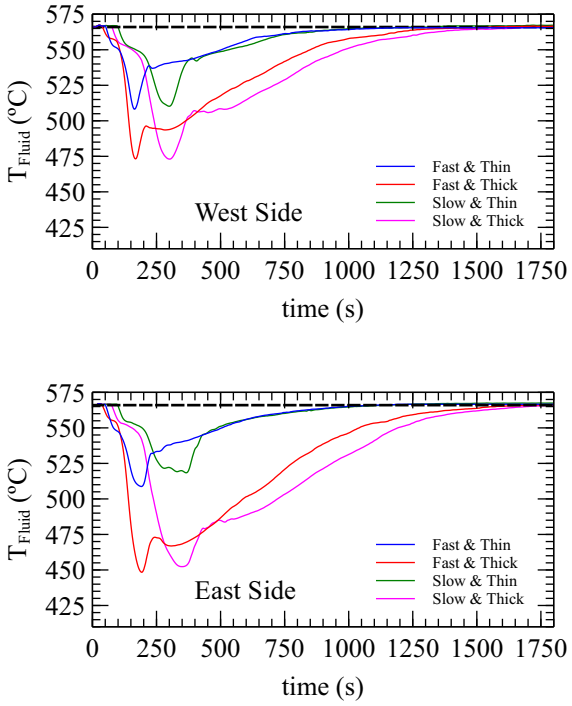

Figure 7.5: Outlet fluid temperature variation after the studied DNI disturbances go over the solar field at 12 pm solar time, and using the modified aiming strategy.

Chapter 8

Conclusions

In solar central receiver systems, the enormous number of heliostats makes the aiming methodology a complex task. This research project proposed a novel method that allows using closed loop control strategies to aim heliostats over the central receiver. The first contribution of this thesis is the proposal of a methodology that bases its performance on inducing an agent group behavior over clusters of heliostats. Therefore, through this approach, a multivariate Dynamic Matrix Control strategy allowed distributing heat flux over the central receiver according to a predefined profile. The analysis also indicated that the control strategy effectively works while the system operates under off-design conditions.

The second contribution of this research allowed the development of a biomimetic model to represent the dynamic behavior of cloud shadows based on a bacterial colony growth. The analysis of variance indicated that there are no statistical differences between the proposed model and the real phenomenon. It means that using a proper set of tuning parameters makes that the proposed model reaches the desired performance to obtain solar radiation transient responses as shown in actual data. The advantage of the tuning procedure consists of using one-dimensional measurements to develop a two-dimensional model. This biomimetic model is a useful tool for analyzing the dynamic effects of solar radiation transients on solar processes.

The third contribution of this dissertation consists of the analysis and improvement of the aiming methodology while the system is under cloud disturbances. The performance analysis showed the basic closed control loop works correctly under clear sky conditions but produces undesired overshoots and high heating rate on the controlled variables when the system is under the influence of DNI transients. These problems were overcome by a set point modification temporally supported by a PI controller. Additionally, even though its performance is strongly associated with the type of DNI transient, the aiming strategy is always promoting the safest path towards

operating the central receiver. The analysis of the aiming strategy performance under disturbances made clear that the rate of change in the controlled variables is crucial to develop the control strategy.

Finally, this methodology unlocks a path to show that available MIMO closed loop control strategies can be employed in the aiming strategy of solar central receiver systems.

Appendix A

Publications derived of this dissertation

Renewable Energy 96 (2016) 157–166

Contents lists available at ScienceDirect

Renewable Energy

journal homepage: www.elsevier.com/locate/renene

A biomimetic approach for modeling cloud shading with dynamic behavior

Jesús M. García [a], Ricardo Vasquez Padilla [b], Marco E. Sanjuan [a, *]

[a] Department of Mechanical Engineering, Universidad del Norte, Barranquilla, Colombia
[b] School of Environment, Science and Engineering, Southern Cross University, Lismore, NSW, 2480, Australia

ARTICLE INFO

Article history:
Received 1 February 2016
Received in revised form
6 April 2016
Accepted 24 April 2016
Available online 3 May 2016

Keywords:
Bacteria colony
Agent based modeling
Dynamic shading
Fuzzy

ABSTRACT

Clouds are a complex phenomenon which is the result of a strong interaction between multiple variables. Modeling its behavior through physical principles is a task that requires time and is computationally demanding. One of the main effects caused by clouds are the shadows produced over the earth's surface, a phenomenon inherently complex due its origin. This paper proposes a computationally low-demanding model for imitating (not predicting) the behavior of cloud shading by applying a biomimetic approach. This analogy relays on using a bacterial colony growth behavior. The aim of this paper is to establish a methodology to develop a cloud-shading model useful for transient analysis in solar fields. The proposed model is evaluated qualitative and quantitative by comparing it with a model based on fractal surfaces and with real sky images. The qualitative evaluation indicates that shadows created by the proposed model change its shapes and move as seen in the real phenomenon. On the other hand, the quantitative assessment is accomplished through the Fast Fourier Transform analysis. This analysis indicates that the proposed model is able to achieve the performance shown by real cloud images.

1. Introduction

Clouds are a complex phenomenon which is the result of the interaction of several parameters. These are defined as a type of hydrometeor, that is, an ensemble of liquid or solid water particles suspended in or falling through air. According to the World Meteorological Organization (WMO) [1], clouds classification has *ten* different groups depending on the height of the cloud. Names of these groups come from Latin roots such as stratus (*layer*), cumulus (*heap or puffy*), cirrus (*curl of hair*) [2]. Modeling this phenomenon using physical principles has been proposed by several research based on momentum, continuity, and energy balances. This kind of approach is useful for studying the impact of variables such as temperature, pressure, and velocity on cloud formation In [2–5]. In this way, after implementing the model, it is possible to determine the shading patterns over the surface. However, this complex model calculates several physical variables, and therefore solving these partial differential equations is computationally demanding. For this reason, there are several approaches using graphic tools for modeling clouds and that consequently are useful for developing cloud shading. Among these approaches, there are some graphic tools which use the same principles developed in computer games. Examples of these methods are polygon, procedural noise, textures sprite, metaball, particle system, or voxel volumes. These methods can be combined to obtain better results In [6].

There are several impacts of clouds on the earth. One of these is the attenuation of solar radiation, mainly the direct normal irradiance [7,8]. Several approaches for taking into account clouds in solar radiation analysis have been proposed. Some of them are built in order to match data from specific places and then develop solar radiation maps [9,10]. In Ref. [11], the changes in solar radiation were analyzed through the representation of clouds as a group of circles. These circles are spread in a two dimensional space following the homogeneous spatial Poisson process. Another approach is shown by Ref. [12]; in which clouds are represented by fractal surfaces truncated at different heights. There are also models whose core consists of statistical analysis of time data series or all-sky images in order to predict solar radiation changes [13,14].

In general, most of the above mentioned models follow the variable-based approach for representing the phenomenon. However, there are several ways for developing such representation in some complex cases. One approach that has received special

* Corresponding author.
E-mail addresses: jesusmg@uninorte.edu.co (J.M. García), ricardo.vasquez.padilla@scu.edu.au (R.V. Padilla), msanjuan@uninorte.edu.co (M.E. Sanjuan).

http://dx.doi.org/10.1016/j.renene.2016.04.070
0960-1481/

Paper 1: Published in Journal of Renewable Energy.

Dynamic modeling of solar radiation disturbances based on a biomimetic cloud shading model

Jesús García[a,1], Iván Portnoy[a,2], Ricardo Vasquez Padilla[b,3], Marco E. Sanjuan[a,*]

[a] *Department of Mechanical Engineering. Universidad del Norte, Barranquilla, Colombia*
[b] *School of Environment, Science and Engineering. Southern Cross University, Lismore, NSW, 2480, Australia*

Abstract

Variation in direct solar radiation is one of the main disturbances that any solar system must handle to maintain efficiency at acceptable levels. As known, solar radiation profiles change due to earth's movements. Even though this change is not manipulable, its behavior is predictable. However, at ground level, direct solar radiation mainly varies due to the effect of clouds, which is a complex phenomenon not easily predictable. In this paper, dynamic solar radiation time series in a $2D$ spatial domain are obtained using a biomimetic cloud-shading model. The model is tuned and compared against available measurement time series. The procedure uses an objective function based on statistical indexes that allow extracting the most important characteristics of an actual set of curves. Then, a multi-objective optimization algorithm finds the tuning parameters of the model that better fit data. The results showed that it is possible to obtain responses similar to real direct solar radiation transients using the biomimetic model, which is useful for other studies such as testing control strategies in solar thermal plants.

Keywords: Agent-Based model; direct solar radiation; cloud shading; multi-objective optimization.

Paper 2: Accepted for publication on December 2017 in Journal of Solar Energy Engineering: Including Wind Energy and Building Energy Conservation.

Multivariable closed control loop methodology for heliostat aiming manipulation in solar central receiver systems

Jesús García [a,1] Yen Chean Soo Too [b,2] Ricardo Vasquez Padilla [c,3]
Andrew Beath [b,4] Jin-Soo Kim [b,5] Marco E. Sanjuan [a,6]

[a] Department of Mechanical Engineering. Universidad del Norte, Barranquilla, Colombia
[b] CSIRO Energy Centre, Mayfield West, NSW 2304, Australia
[c] School of Environment, Science and Engineering. Southern Cross University, Lismore, NSW, 2480, Australia

Abstract

Maintaining receiver's thermal stresses and corrosion below the material limits are issues that need careful attention in solar thermal towers. Both depend on heliostats' aiming points over the central receiver and available direct solar radiation at any instant. Since this technology relies on an unavoidable time-changing resource, aiming points need to be properly manipulated to avoid excessive hot spots. This paper proposes a new aiming point strategy based on a multivariable model predictive control (MPC) approach. It shows an alternative approach by introducing an agent-based group behaviour over heliostats' subsets, which makes possible either concentrating or dispersing solar radiation as required by the MPC algorithm. Simulated results indicate that it is feasible to develop a closed-loop control procedure that distributes solar irradiance over the central receiver according to the predefined heat flux limits. The performance of the proposed

[1] jesusmg@uninorte.edu.co
[2] yenchean@csiro.au
[3] ricardo.vasquez.padilla@scu.edu.au
[4] andrew.beath@csiro.au
[5] jin-soo.kim@csiro.au
[6] msanjuan@uninorte.edu.co

Paper 3: Accepted for publication on December 2017 in Journal of Solar Energy Engineering: Including Wind Energy and Building Energy Conservation

Renewable Energy xxx (2018) xxx-xxx

Contents lists available at ScienceDirect

Renewable Energy

journal homepage: www.elsevier.com

Dynamic performance of an aiming control methodology for solar central receivers due to cloud disturbances

Jesús García[a], Yen Chean Soo Too[b, *], Ricardo Vasquez Padilla[c], Andrew Beath[b], Jin-Soo Kim[b], Marco E. Sanjuan[a]

[a] Department of Mechanical Engineering, Universidad del Norte, Barranquilla, Colombia
[b] CSIRO Energy Centre, Mayfield West, NSW 2304, Australia
[c] School of Environment, Science and Engineering. Southern Cross University, Lismore, NSW, 2480, Australia

ARTICLE INFO

Article history:
Available online xxx

Keywords:
Solar central receiver
Heliostat aiming
Multivariable closed control loop
Concentrating solar thermal
Cloud disturbances

ABSTRACT

An appropriate control of the heat flux distribution over the solar central receiver is essential to achieve an efficient and safe operation of solar tower systems. High solar radiation variation due to moving clouds may cause failures to the solar receiver. This paper shows a dynamic performance analysis of a solar central receiver operating when short-time cloud passages partially shade the solar field. The solar receiver incorporates an aiming methodology based on a closed loop model predictive control approach. The DNI changes are simulated using an agent-based model that closely emulates the transients in solar radiation caused by clouds. These models are coupled with a solar system model that resembles the Gemasolar solar plant. The simulations showed that the base feedback loop aiming strategy could successfully restore the solar receiver back to its steady state after transient operations caused by clouds. However, undesired overshoots in incident flux density and high heating rates in the controlled variables were found. These issues are overcome through a setpoint readjustment approach, which is temporally supported by a PI controller. The results show that the proposed aiming control strategy can provide a continuous safe operation of the solar central receiver when subject to transient flux distribution due to clouds.

Nomenclature

A	Identification matrix for the DMC strategy
A_H	Mirror area of the heliostat, [m^2]
$C(t)$	Controlled variable at time instant t, [MW/m^2]
D	Distance between the heliostat and the receiver, [m]
$E(t)$	Difference between the setpoint and the controlled variables
f_{at}	Attenuation factor due atmospheric conditions
$Flux_{HF}$	Heat flux perpendicular to the receiver-heliostat vector, [MW/m^2]
$F_{Receiver}$	Heat flux over the receiver, [MW/m^2]
HTF	Heat transfer fluid
I_D	Direct Normal Irradiance, [W/m^2]
P_H	Solar power concentrated by the heliostat, [MW/m^2]
PI	Proportional-Integral Controller
r	Assigned a radius around the aiming points
w	Incidence angle, [rad]
x, y	Coordinates of the receiver's surface, [m]
u	Control output of the DMC strategy

Acronyms

AFD	Allowable flux distribution, [MW/m^2]
DMC	Dynamic Matrix Control
DNI_t	DNI at time instant t, [W/m^2]
DNI_{CS}	DNI at clear sky conditions, [W/m^2]
$HFLCAL$	Heliostat field layout calculator
MPC	Model Predictive Control
SP	Setpoint
u	Control output of the DMC strategy

Greek symbols

κ	Value that indicates the degree of dispersion of a heliostat group.
λ	Tuning parameters for the DMC strategy
ω_p	Angle between the normal vector of the receiver surface and the receiver-heliostat vector, [rad]
ρ	Reflectivity of the heliostat mirror
σ_{HF}	Total effective deviation, [mrad]
σ_{slp}	Beam quality due to mirror curvature and imperfections, [mrad]
σ_{sun}	Solar radiation density distribution, [mrad]
σ_t	Tracking errors distribution, [mrad]
κ	Manipulated variable that determines the size of the radius around the aiming point
α	Relative position of a heliostat in the group
β	Scaling factor to obtain r, [−]

* Corresponding author.
Email addresses: jesusmg@uninorte.edu.co (J. García); ricardo.vasquez.padilla@scu.edu.au (R.V. Padilla); andrew.beath@csiro.au (A. Beath); jin-soo.kim@csiro.au (J-S Kim); msanjuan@uninorte.edu.co (M.E. Sanjuan)

https://doi.org/10.1016/j.renene.2018.01.019
0960-1481/

Paper 4: Accepted for publication on December 2017 in Journal of Renewable Energy

Bibliography

[1] V Ruiz Hernandez. "Evaluación del potencial de energía solar termoeléctrica". In: *Estudio Técnico PER* 2020 (2011), pp. 7–50.

[2] Ibrahim Dincer and Calin Zamfirescu. *Sustainable energy systems and applications*. Springer Science & Business Media, 2011.

[3] CJ Winter, RL Sizmann, and LL Vant-Hull. "Solar Power Plants: Fundamentals, Technology, Systems". In: *Economics* (1991), pp. 3–540.

[4] D. Mills. "Advances in solar thermal electricity technology". In: *Solar Energy* 76.13 (2004). Solar World Congress 2001, pp. 19 –31. ISSN: 0038-092X. DOI: http://doi.org/10.1016/S0038-092X(03)00102-6.

[5] Matthew Wittenstein and Geoffrey Rothwell. "Projected costs of generating electricity". In: *International Energy Agency, Nuclear Energy Agency, Organization for Economic Co-operation and Development* (2015).

[6] E F Camacho et al. *Control of Solar Energy Systems*. Advances in Industrial Control. Springer, 2012. ISBN: 9780857299154.

[7] Steven Chu and Arun Majumdar. "Opportunities and challenges for a sustainable energy future". In: *nature* 488.7411 (2012), pp. 294–303.

[8] V. Siva Reddy et al. "State-of-the-art of solar thermal power plantsA review". In: *Renewable and Sustainable Energy Reviews* 27 (Nov. 2013), pp. 258–273. ISSN: 13640321. DOI: 10.1016/j.rser.2013.06.037. URL: http://www.sciencedirect.com/science/article/pii/S1364032113004140.

[9] M.R. Rodríguez-Sánchez et al. "Thermal design guidelines of solar power towers". In: *Applied Thermal Engineering* 63.1 (Feb. 2014), pp. 428–438. ISSN: 13594311. DOI: 10.1016/j.applthermaleng.2013.11.014. URL: http://www.sciencedirect.com/science/article/pii/S1359431113008028.

[10] Gregory J Kolb et al. "Power tower technology roadmap and cost reduction plan". In: *SAND2011-2419, Sandia National Laboratories, Albuquerque, NM* 7 (2011).

[11] Patricia Kuntz Falcone. *A handbook for solar central receiver design*. Tech. rep. Sandia National Labs., Livermore, CA (USA), 1986.

[12] Roberta Mancini. "Volumetric Solar Receiver for a Parabolic Dish and Micro-Gas Turbine system: Design, modelling and validation using Multi-Objective Optimization". PhD thesis. KTH School of Industrial Engineering and Management, 2015.

[13] Antonio L. vila Marn. "Volumetric receivers in Solar Thermal Power Plants with Central Receiver System technology: A review". In: *Solar Energy* 85.5 (2011), pp. 891 –910. ISSN: 0038-092X. DOI: http://doi.org/10.1016/j.solener.2011.02.002. URL: http://www.sciencedirect.com/science/article/pii/S0038092X11000302.

[14] UPME-IDEAM. "Atlas de Radiación solar de Colombia". In: *Santafé de Bogotá DC: Unidad de Planeación Minero Energética, Ministerio de Minas y Energía* (2005).

[15] A Valverde and G Weinrebe. "Implementation of an Automatic Aim-Point Strategy for a Volumetric Receiver in the PSA CESA-1 Heliostat Field". In: *8 Int. Symp. Solar Thermal Concentrating Technologies*. Vol. 2. K{ö}ln, CF M{ü}ller. 1996, pp. 1047–1065.

[16] C. Tyner, G. Kolb, and M. Prairie. "Solar power tower development: Recent experiences". English. In: (Dec. 1996). URL: http://www.osti.gov/scitech/biblio/505159.

[17] M. Berenguel et al. "An artificial vision-based control system for automatic heliostat positioning offset correction in a central receiver solar power plant". In: *Solar Energy* 76.5 (2004), pp. 563–575. ISSN: 0038092X. DOI: 10.1016/j.solener.2003.12.006. URL: http://www.sciencedirect.com/science/article/pii/S0038092X0300464X.

[18] Abraham Kribus et al. "Closed loop control of heliostats". In: *Energy* 29.5-6 (Apr. 2004), pp. 905–913. ISSN: 03605442. DOI: 10.1016/S0360-5442(03)00195-6. URL: http://www.sciencedirect.com/science/article/pii/S0360544203001956.

[19] Y T Chen, B H Lim, and C S Lim. "General sun tracking formula for heliostats with arbitrarily oriented axes". In: *Journal of solar energy engineering* 128.2 (2006), pp. 245–250.

[20] Kosuke Aiuchi et al. "Sensor-controlled heliostat with an equatorial mount". In: *Solar Energy* 80.9 (Sept. 2006), pp. 1089–1097. ISSN: 0038092X. DOI: 10.1016/j.solener.2005.10.007. URL: http://www.sciencedirect.com/science/article/pii/S0038092X05003634.

[21] Karel Johan Malan. "A heliostat field control system". PhD thesis. Stellenbosch: Stellenbosch University, 2014.

[22] Jos M. Quero et al. "Tracking Control System Using an Incident Radiation Angle Microsensor". English. In: *IEEE Transactions on Industrial Electronics* 54.2 (Apr. 2007), pp. 1207–1216. ISSN: 0278-0046. DOI: 10.1109/TIE.2007.893075. URL: http://ieeexplore.ieee.org/articleDetails.jsp?arnumber=4140635.

[23] O Flores et al. “Thermal stresses analysis of a circular tube in a central receiver”. In: *Energy Procedia* 49 (2014), pp. 354–362.

[24] NC Cruz et al. “On Achieving a Desired Flux Distribution on the Receiver of a Solar Power Tower Plant”. In: *XIII GLOBAL OPTIMIZATION WORKSHOP GOW16 4-8 September 2016*. Vol. 16. 2016, pp. 61–64.

[25] Saeb M Besarati, D Yogi Goswami, and Elias K Stefanakos. “Optimal heliostat aiming strategy for uniform distribution of heat flux on the receiver of a solar power tower plant”. In: *Energy Conversion and Management* 84 (2014), pp. 234–243.

[26] Adrien Salomé et al. “Control of the flux distribution on a solar tower receiver using an optimized aiming point strategy: Application to THEMIS solar tower”. In: *Solar Energy* 94 (Aug. 2013), pp. 352–366. ISSN: 0038092X. DOI: 10.1016/j.solener.2013.02.025. URL: http://www.sciencedirect.com/science/article/pii/S0038092X1300090X.

[27] Alberto Snchez-Gonzlez, Mara Reyes Rodrguez-Snchez, and Domingo Santana. “Aiming strategy model based on allowable flux densities for molten salt central receivers”. In: *Solar Energy* (2016), pp. –. ISSN: 0038-092X. DOI: http://dx.doi.org/10.1016/j.solener.2015.12.055. URL: http://www.sciencedirect.com/science/article/pii/S0038092X16001468.

[28] Alexis B Zavoico. “Design basis document”. In: *Sandia National Laboratories* (2001).

[29] Lorin L Vant-Hull. “The role of Allowable flux density in the design and operation of molten-salt solar central receivers”. In: *Journal of solar energy engineering* 124.2 (2002), pp. 165–169.

[30] James E Pacheco et al. “Final test and evaluation results from the Solar Two project”. In: *Report No. SAND2002-0120, Sandia National Laboratories, Albuquerque, NM* (2002).

[31] FJ García-Martín et al. “Heuristic knowledge-based heliostat field control for the optimization of the temperature distribution in a volumetric receiver”. In: *Solar Energy* 66.5 (1999), pp. 355–369.

[32] C Aurora et al. “Predictive control of thermal power plants”. In: *International Journal of Robust and Nonlinear Control* 14.4 (2004), pp. 415–433.

[33] Peter Schwarzbözl et al. “Solar gas turbine systems: Design, cost and perspectives”. In: *Solar Energy* 80.10 (Oct. 2006), pp. 1231–1240. ISSN: 0038092X. DOI: 10.1016/j.solener.2005.09.007. URL: http://www.sciencedirect.com/science/article/pii/S0038092X05003348.

[34] A. Kribus et al. “A solar-driven combined cycle power plant”. In: *Solar Energy* 62.2 (Feb. 1998), pp. 121–129. ISSN: 0038092X. DOI: 10.1016/S0038-092X(97)00107-2. URL: http://www.sciencedirect.com/science/article/pii/S0038092X97001072.

[35] Omar Behar, Abdallah Khellaf, and Kamal Mohammedi. "A review of studies on central receiver solar thermal power plants". In: *Renewable and Sustainable Energy Reviews* 23 (July 2013), pp. 12–39. ISSN: 13640321. DOI: 10.1016/j.rser.2013.02.017. URL: http://www.sciencedirect.com/science/article/pii/S1364032113001184.

[36] A Bemporad. *Hybrid Toolbox - User's Guide*. 2004.

[37] Pierre Garcia, Alain Ferriere, and Jean-Jacques Bezian. "Codes for solar flux calculation dedicated to central receiver system applications: a comparative review". In: *Solar Energy* 82.3 (2008), pp. 189–197.

[38] Solar Energy Research Institute. Technical Information Branch and United States. Dept. of Energy. *Solar Energy Computer Models Directory*. Solar Energy Research Institute, 1985.

[39] Michael Wagner. *Integrated Layout and Optimization Tool for Solar Power Towers*. National Renewable Energy Laboratory, NREL, 2016. URL: https://www.nrel.gov/csp/solarpilot.html.

[40] Nate Blair et al. "System Advisor Model, SAM 2014.1.14: General Description". In: (2013). URL: http://www.nrel.gov/docs/fy14osti/61019.pdf.

[41] Manuel J Blanco, Juana M Amieva, and Azael Mancillas. "The Tonatiuh Software Development Project: An open source approach to the simulation of solar concentrating systems". In: *ASME 2005 International Mechanical Engineering Congress and Exposition*. American Society of Mechanical Engineers. 2005, pp. 157–164.

[42] Pierre Garcia, Alain Ferriere, and Jean-Jacques Bezian. "Codes for solar flux calculation dedicated to central receiver system applications: A comparative review". In: *Solar Energy* 82.3 (Mar. 2008), pp. 189–197. ISSN: 0038092X. DOI: 10.1016/j.solener.2007.08.004. URL: http://linkinghub.elsevier.com/retrieve/pii/S0038092X07001727.

[43] M Kiera. "Heliostat field: computer codes, requirements, comparison of methods". In: *In: Becker, M., Böhmer, M. (Eds.), GAST-proceedings of the Final Presentation. Springer, Berlin* (1989), pp. 95–113.

[44] Peter Schwarzbözl, Robert Pitz-Paal, and Mark Schmitz. *Visual HFLCAL - A Software Tool for Layout and Optimisation of Heliostat Fields*. de. Sept. 2009. URL: http://elib.dlr.de/60308/1/11354-Schwarzbozl.pdf.

[45] Francisco J. Collado. "One-point fitting of the flux density produced by a heliostat". In: *Solar Energy* 84.4 (Apr. 2010), pp. 673–684. ISSN: 0038092X. DOI: 10.1016/j.solener.2010.01.019. URL: http://www.sciencedirect.com/science/article/pii/S0038092X10000320.

[46] Francisco J. Collado and Jesús Guallar. "A review of optimized design layouts for solar power tower plants with campo code". In: *Renewable and Sustainable Energy Reviews* 20 (Apr. 2013), pp. 142–154. ISSN: 13640321. DOI: 10.1016/j.rser.2012.11.076. URL: http://www.sciencedirect.com/science/article/pii/S1364032112006909.

[47] Alberto Sánchez-González and Domingo Santana. "Solar flux distribution on central receivers: A projection method from analytic function". In: *Renewable Energy* 74 (Feb. 2015), pp. 576–587. ISSN: 09601481. DOI: 10.1016/j.renene.2014.08.016. URL: http://www.sciencedirect.com/science/article/pii/S0960148114004753.

[48] Ibrahim Reda and Afshin Andreas. *Sun Position Matlab Algoritm*. 2003. URL: http://www.mathworks.com/matlabcentral/fileexchange/4605-sun-position-m (visited on 01/01/2015).

[49] Ibrahim Reda and Afshin Andreas. "Solar position algorithm for solar radiation applications". In: *Solar Energy* 76.5 (Jan. 2004), pp. 577–589. ISSN: 0038092X. DOI: 10.1016/j.solener.2003.12.003. URL: http://www.sciencedirect.com/science/article/pii/S0038092X0300450X.

[50] J Meeus. *Astronomical Algorithms*. Willmann-Bell, 1998. ISBN: 9780943396613.

[51] G Sassi. "Some notes on shadow and blockage effects". In: *Solar energy* 31.3 (1983), pp. 331–333.

[52] Francisco J Collado and Jesús Guallar. "Campo: Generation of regular heliostat fields". In: *Renewable energy* 46 (2012), pp. 49–59.

[53] M.R. Rodrguez-Snchez et al. "Thermal design guidelines of solar power towers". In: *Applied Thermal Engineering* 63.1 (2014), pp. 428 –438. ISSN: 1359-4311. DOI: http://dx.doi.org/10.1016/j.applthermaleng.2013.11.014. URL: http://www.sciencedirect.com/science/article/pii/S1359431113008028.

[54] Mara Reyes Rodrguez-Snchez et al. "Comparison of simplified heat transfer models and {CFD} simulations for molten salt external receiver". In: *Applied Thermal Engineering* 73.1 (2014), pp. 993 –1005. ISSN: 1359-4311. DOI: http://dx.doi.org/10.1016/j.applthermaleng.2014.08.072. URL: http://www.sciencedirect.com/science/article/pii/S1359431114007686.

[55] R.B. Bird, W.E. Stewart, and E.N. Lightfoot. *Transport Phenomena*. Wiley International edition. Wiley, 2007. ISBN: 9780470115398. URL: https://books.google.com.au/books?id=L5FnNlIaGfcC.

[56] F.P. Incropera and D.P. DeWitt. *Fundamentals of heat and mass transfer*. John Wiley & Sons Australia, Limited, 2002. ISBN: 9780471386506. URL: https://books.google.com.au/books?id=l7V_vgAACAAJ.

[57] Roberta Ferri, Antonio Cammi, and Domenico Mazzei. "Molten salt mixture properties in RELAP5 code for thermodynamic solar applications". In: *International Journal of Thermal Sciences* 47.12 (2008), pp. 1676 –1687. ISSN: 1290-0729. DOI: http://dx.doi.org/10.1016/j.ijthermalsci.2008.01.007. URL: http://www.sciencedirect.com/science/article/pii/S1290072908000197.

[58] Z.S. Chang et al. "The Design and Numerical Study of a 2MWh Molten Salt Thermocline Tank". In: *Energy Procedia* 69 (2015), pp. 779 –789. ISSN: 1876-6102. DOI: http://dx.doi.org/10.1016/j.egypro.2015.03.094. URL: http://www.sciencedirect.com/science/article/pii/S1876610215004002.

[59] D L Siebers and J S Kraabel. *Estimating convective energy losses from solar central receivers*. 1984. DOI: 10.2172/6906848. URL: http://www.osti.gov/scitech/servlets/purl/6906848.

[60] SW Churchill and M Bernstein. "A correlating equation for forced convection from gases and liquids to a circular cylinder in crossflow". In: *Journal of Heat Transfer* 99.2 (1977), pp. 300–306.

[61] Jin-Soo Kim et al. "Ideal Heat Transfer Conditions for Tubular Solar Receivers with Different Design Constraints". In: *Solar Paces 2016 Symposium. Abu Dhabi, United Arab Emirates*. 2016.

[62] B.E. Gatewood. "XXIII. Thermal stresses in long cylindrical bodies". In: *The London, Edinburgh, and Dublin Philosophical Magazine and Journal of Science* 32.213 (1941), pp. 282–301. DOI: 10.1080/14786444108521303. eprint: http://dx.doi.org/10.1080/14786444108521303. URL: http://dx.doi.org/10.1080/14786444108521303.

[63] R.B. Hetnarski and M.R. Eslami. *Thermal Stresses – Advanced Theory and Applications*. Solid Mechanics and Its Applications. Springer Netherlands, 2009. ISBN: 9781402092466.

[64] ASME. *BPVC Section II-Materials-Part D-Properties-(Metric)*. ASME, 2015.

[65] RW Bradshaw. "Thermal Convection Loop Study of the Corrosion of Incoloy 800 in Molten NaNO3-KNO3". In: *Corrosion* 43.3 (1987), pp. 173–178.

[66] World Meteorological Organization. Secretariat-WMO. *International Cloud Atlas - Volume 1: Manual on the Observation of Clouds and Other Meteors (annex 1 to WMO Technical Regulations)*. WMO (Series). 1975.

[67] Mark Z Jacobson. *Fundamentals of atmospheric modeling*. Cambridge university press, 2005.

[68] David O'C Starr and Stephen K Cox. "Cirrus Clouds. Part I: A Cirrus Cloud Model." In: *Journal of Atmospheric Sciences* 42 (1985), pp. 2663–2681.

[69] David O'C Starr and Stephen K Cox. "Cirrus clouds. Part II: Numerical experiments on the formation and maintenance of cirrus". In: *Journal of the atmospheric sciences* 42.23 (1985), pp. 2682–2694.

[70] Ryo Miyazaki et al. “A method for modeling clouds based on atmospheric fluid dynamics”. In: *Computer Graphics and Applications, 2001. Proceedings. Ninth Pacific Conference on*. IEEE. 2001, pp. 363–372.

[71] Bei Wang. *Techniques for efficient cloud modeling, simulation and rendering*. ProQuest, 2007.

[72] R. Tapakis and A.G. Charalambides. “Enhanced values of global irradiance due to the presence of clouds in Eastern Mediterranean”. In: *Renewable Energy* 62 (2014), pp. 459 –467. ISSN: 0960-1481.

[73] Ricardo Cesar de Andrade and Chigueru Tiba. “Extreme global solar irradiance due to cloud enhancement in northeastern Brazil”. In: *Renewable Energy* 86 (2016), pp. 1433 –1441. ISSN: 0960-1481.

[74] Ana Pérez-Burgos et al. “Reconstruction of long-term direct solar irradiance data series using a model based on the Cloud Modification Factor”. In: *Renewable Energy* 77 (2015), pp. 115 –124. ISSN: 0960-1481.

[75] Viorel Badescu and Alexandru Dumitrescu. “Simple models to compute solar global irradiance from the CMSAF product Cloud Fractional Coverage”. In: *Renewable Energy* 66 (2014), pp. 118 –131. ISSN: 0960-1481.

[76] Ery Arias-Castro, Jan Kleissl, and Matthew Lave. “A Poisson model for anisotropic solar ramp rate correlations”. In: *Solar Energy* 101 (Mar. 2014), pp. 192–202. ISSN: 0038092X.

[77] Chengrui Cai and Dionysios C Aliprantis. “Cumulus cloud shadow model for analysis of power systems with photovoltaics”. In: *Power Systems, IEEE Transactions on* 28.4 (2013), pp. 4496–4506.

[78] Marek Brabec, Viorel Badescu, and Marius Paulescu. “Cloud shade by dynamic logistic modeling”. In: *Journal of Applied Statistics* 41.6 (2014), pp. 1174–1188.

[79] Hsu-Yung Cheng and Chih-Chang Yu. “Multi-model solar irradiance prediction based on automatic cloud classification”. In: *Energy* 91 (2015), pp. 579 –587.

[80] Germain Augsburger and Daniel Favrat. “Modelling of the receiver transient flux distribution due to cloud passages on a solar tower thermal power plant”. In: *Solar Energy* 87 (2013), pp. 42 –52.

[81] G Nigel Gilbert. *Agent-based models*. 153. Sage, 2008.

[82] J U Kreft, G Booth, and J W Wimpenny. “BacSim, a simulator for individual-based modelling of bacterial colony growth.” In: *Microbiology (Reading, England)* 144 (Pt 1 (Dec. 1998), pp. 3275–87.

[83] Arthur L Koch. “Microbial physiology and ecology of slow growth.” In: *Microbiology and Molecular Biology Reviews* 61.3 (1997), pp. 305–318.

[84] Timothy David Paustian. *Microbiology Textbook: The World of Microbes*. Department of Bacteriology, University of Wisconsin-Madison, 2001.

[85] S. J. Pirt. “The Maintenance Energy of Bacteria in Growing Cultures”. English. In: *Proceedings of the Royal Society of London. Series B, Biological Sciences* 163.991 (1965), pp. 224–231.

[86] C. Vlachos et al. “A rule-based approach to the modelling of bacterial ecosystems”. In: *Biosystems* 84.1 (2006), pp. 49 –72.

[87] Mengying Li et al. “Quantitative evaluation of the impact of cloud transmittance and cloud velocity on the accuracy of short-term {DNI} forecasts”. In: *Renewable Energy* 86 (2016), pp. 1362 –1371. ISSN: 0960-1481.

[88] Ben Niu et al. “Biomimicry of quorum sensing using bacterial lifecycle model.” In: *BMC bioinformatics* 14 Suppl 8.Suppl 8 (Jan. 2013), S8.

[89] A Andreas and T Stoffel. “NREL Solar Radiation Research Laboratory (SRRL): Baseline Measurement System (BMS); Golden, Colorado (Data);” in: *NREL Report No. DA-5500-56488.* (1981). URL: http://dx.doi.org/10.5439/1052221.

[90] Zhanwei Yuan et al. “Description of shape characteristics through Fourier and wavelet analysis”. In: *Chinese Journal of Aeronautics* 27.1 (2014), pp. 160–168.

[91] Dengsheng Zhang and Guojun Lu. “Shape-based image retrieval using generic Fourier descriptor”. In: *Signal Processing: Image Communication* 17.10 (2002), pp. 825–848.

[92] Frederik Kratzert. *Implementation of the Generic Fourier Descriptors*. 2015. URL: http://www.mathworks.com/matlabcentral/fileexchange/52643-fd-=-gfd-bw-m-n--implementation-of-the-generic-fourier-descriptors/all_files.

[93] Teolan Tomson. “Transient processes of solar radiation”. In: *Theoretical and applied climatology* 112.3-4 (2013), pp. 403–408.

[94] M. Sengupta and A. Andreas. “Oahu Solar Measurement Grid (1-Year Archive): 1-Second Solar Irradiance; Oahu, Hawaii (Data)”. English. In: (Mar. 2010). DOI: 10.7799/1052451. URL: http://www.osti.gov/scitech/biblio/1052451.

[95] S. Jackson. *Statistics Plain and Simple*. Cengage Learning, 2009.

[96] Wenfu Ku, Robert H Storer, and Christos Georgakis. “Disturbance detection and isolation by dynamic principal component analysis”. In: *Chemometrics and intelligent laboratory systems* 30.1 (1995), pp. 179–196.

[97] Douglas C. Montgomery. *Design and Analysis of Experiments and Educational Version of Design Expert*. Vol. 1997. John Wiley & Sons Canada, Limited, 1997, p. 720.

[98] Venkat Venkatasubramanian et al. “A review of process fault detection and diagnosis: Part I: Quantitative model-based methods”. In: *Computers & Chemical Engineering* 27.3 (2003), pp. 293 –311. ISSN: 0098-1354. DOI: http://dx.doi.org/10.1016/S0098-1354(02)00160-6. URL: http://www.sciencedirect.com/science/article/pii/S0098135402001606.

[99] Venkat Venkatasubramanian, Raghunathan Rengaswamy, and Surya N Kavuri. "A review of process fault detection and diagnosis: Part II: Qualitative models and search strategies". In: *Computers & Chemical Engineering* 27.3 (2003), pp. 313 –326. ISSN: 0098-1354. DOI: http://dx.doi.org/10.1016/S0098-1354(02)00161-8. URL: http://www.sciencedirect.com/science/article/pii/S0098135402001618.

[100] Venkat Venkatasubramanian et al. "A review of process fault detection and diagnosis: Part III: Process history based methods". In: *Computers & Chemical Engineering* 27.3 (2003), pp. 327 –346. ISSN: 0098-1354. DOI: http://dx.doi.org/10.1016/S0098-1354(02)00162-X. URL: http://www.sciencedirect.com/science/article/pii/S009813540200162X.

[101] Evan L. Russell, Leo H. Chiang, and Richard D. Braatz. *Data-driven Methods for Fault Detection and Diagnosis in Chemical Processes*. Advances in Industrial Control. London: Springer London, 2000.

[102] Rubén Daniel Ledesma and Pedro Valero-Mora. "Determining the number of factors to retain in EFA: An easy-to-use computer program for carrying out parallel analysis". In: *Practical Assessment, Research & Evaluation* 12.2 (), pp. 1–11.

[103] Scott B Franklin et al. "Parallel analysis: a method for determining significant principal components". In: *Journal of Vegetation Science* 6.1 (1995), pp. 99–106.

[104] William R Zwick and Wayne F Velicer. "Comparison of five rules for determining the number of components to retain." In: *Psychological bulletin* 99.3 (1986), p. 432.

[105] Alexandre Gagné et al. "High resolution characterisation of solar variability for two sites in Eastern Canada". In: *Solar Energy* 137 (2016), pp. 46–54.

[106] Joshua S Stein, Clifford W Hansen, and Matthew J Reno. "The variability index: A new and novel metric for quantifying irradiance and PV output variability". In: *World Renewable Energy Forum*. Citeseer. 2012, pp. 13–17.

[107] SENER. *CPV & CSP TWO AXES SOLAR TRACKER*. 2016. URL: http://www.sener-power-process.com/EPORTAL_DOCS/GENERAL/SENERV2/DOC-cw499d8e0908599/CPVCSPtwoaxessolartracker.pdf.

[108] J.A. Rossiter. *Model-Based Predictive Control: A Practical Approach*. Control Series. CRC Press, 2003. ISBN: 9780203503966. URL: https://books.google.com.au/books?id=owznQTI-NqUC.

[109] Åke Björck. "Linear Least Squares Problems". In: *Numerical Methods in Matrix Computations*. Cham: Springer International Publishing, 2015, pp. 211–430. ISBN: 978-3-319-05089-8. DOI: 10.1007/978-3-319-05089-8_2. URL: http://dx.doi.org/10.1007/978-3-319-05089-8_2.